National Library of Canada

Acquisitions and Bibliographic Services Branch

395 Wellington Street
Ottawa, Ontario
K1A 0N4

Bibliothèque nationale du Canada

Direction des acquisitions et des services bibliographiques

395, rue Wellington
Ottawa (Ontario)
K1A 0N4

Your file Votre référence

Our file Notre référence

NOTICE

The quality of this microform is heavily dependent upon the quality of the original thesis submitted for microfilming. Every effort has been made to ensure the highest quality of reproduction possible.

If pages are missing, contact the university which granted the degree.

Some pages may have indistinct print especially if the original pages were typed with a poor typewriter ribbon or if the university sent us an inferior photocopy.

AVIS

La qualité de cette microforme dépend grandement de la qualité de la thèse soumise au microfilmage. Nous avons tout fait pour assurer une qualité supérieure de reproduction.

S'il manque des pages, veuillez communiquer avec l'université qui a conféré le grade.

La qualité d'impression de certaines pages peut laisser à désirer, surtout si les pages originales ont été dactylographiées à l'aide d'un ruban usé ou si l'université nous a fait parvenir une photocopie de qualité inférieure.

Canada

The Structure of the Central Recirculation Zone in Enclosed Swirling Flow

by

Chong-Yu Ding

A thesis submitted to the
School of Graduate Studies and Research
in partial fulfillment of the requirement for the degree of
Master of Applied Science

Ottawa-Carleton Institute for Mechanical and Aerospace Engineering
Department of Mechanical Engineering
Faculty of Engineering
University of Ottawa

ISBN 0-315-93573-1

UNIVERSITÉ D'OTTAWA
UNIVERSITY OF OTTAWA

To my Parents

Contents

List of Figures

Glossary of Notation

Roman Symbols

a_1	Inlet solid body core radius
a_2	Solid body core at maximum diameter of the recirculation zone
A_1	$(\frac{a_1}{r_1})^2$
A_2	$(\frac{a_2}{r_2})^2$
B	Refer to equation (3.1)
$COEFV$	Dynamic pressure coefficient
$COFTP$	Static pressure coefficient
F_1	Refer to equation (4.33)
F_2	Refer to equation (4.44)
F_3	Refer to equation (4.47)
F_4	Refer to equation (4.48)
g_r	Gravitational acceleration in radial direction
g_θ	Gravitational acceleration in tangential direction
g_x	Gravitational acceleration in axial direction
G	Dimensionless axial momentum flux
G_x	Axial momentum flux
G_{x1}	Refer to equation (4.56)
G_{x2}	Refer to equation (4.59)
$\Im_M$	Refer to equation (4.100)
$G_{\phi 1}$	Refer to equation (4.43)
$G_{\phi 2}$	Refer to equation (4.46)
$G_{\phi BL}$	Refer to equation (4.86)
$G_{\phi BL,M}$	Refer to equation (4.87)
k	Loss coefficient
L	Sliding sleeve position in the swirl generator
$L1$	Refer to equation (4.74)
$\dot{m}$	Mass flow rate
$\dot{m}_1$	Mass flow rate at station 1
$\dot{m}_2$	Mass flow rate at station 2
$\dot{m}_a$	Manometer measured axial mass flow rate
$\dot{m}_{BL}$	Refer to equation (4.82)
$\dot{m}_{BL,M}$	Refert o equation (4.84)
$\dot{m}_r$	Recirculating mass flow rate
$\dot{m}_t$	Manometer measured tangential mass flow rate

p	Pressure
P_1	Refer to equation (4.57)
P_2	Refer to equation (4.60)
p_{01}	Static pressure on axis at station 1
p_{02}	Static pressure on axis at station 2
$(p_1 - p_2)$	Pressure difference at probe holes 1 and 2
$(p_1 - p_{atm})$	Pressure difference at probe hole 1 and atmosphere
$(p_1 - p_w)$	Pressure difference at probe hole 1 and wall
$(p_2 - p_3)$	Pressure difference at probe holes 2 and 3
$(p_4 - p_5)$	Pressure difference at probe holes 4 and 5
p_{atm}	Atmospheric pressure
p_{ax}	Manometer static pressure at the axial inlet
p_s	Pressure at stagnation point
$(p_t - p_s)$	Pressure difference between total and static pressure
p_{tan}	Manometer static pressure at the tangential inlet
p_w	Wall pressure
Q	Volumetric flow rate at the throat
r	Radial direction in cylindrical coordinate
r_1	Throat radius
r_2	Expansion radius
R_2	$(r_2/r_1)^2$
r_b	Radius at $\Psi = 0$
r_B	Refer to equation (4.84)
r_c	Radius at $u = 0$
r_N	Radius at last measured point
r_s	Radius chosen from experimental results in the solid body region
S	Swirl number
u	Axial velocity component
u_1	Inlet axial velocity near the throat wall
u_{02}	Backflow velocity at station 2
u_2	Axial velocity near the expansion wall
u_{b2}	Axial velocity at r_b
$\bar{u}_{ref}$	Reference axial velocity
Δu	Refer to equation (4.24)
$\bar{u}_M$	Refer to equation (4.85)
u_N	Axial velocity at last measured point
v	Radial velocity component
w	Tangential velocity component
w_2	Tangential velocity at the solid body core boundary

w_N	Tangential velocity at last measured point
w_M	Average tangential velocity from the model
w_s	Tangential velocity chosen from experimental results in the solid body region
x	Axial direction in cylindrical coordinates
Γ	Circulation

Greek Symbols

Γ_1	Refer to equation (4.99)
θ	Angular direction in cylindrical coordinates
κ	Shear coefficient for the axial velocity behind the wake
λ	Refer to equation (4.103)
μ	Viscosity of air
π	3.14159
τ_{xr}	Shear stress refer equation (4.68)
ρ	Local density of air
χ	Yaw angle
ω	Angular velocity
υ	λu_1
ε	Effective turbulent viscosity
Ω	Dimensionless angular momentum flux
Ω_M	Refer to equation (4.94)
Ψ	Stream function
Ψ_ϕ	Angular Momentum stream function
$\Psi_{\phi,B}$	Angular momentum stream function at r_B

ACKNOWLEDGEMENTS

I would like to thank all my colleagues for their support. Thanks must go also to Mr.George Spak, who was always eager to help me to fix all kinds of mechanical problems in my experiment.

I am particularly grateful to Dr.Hallett, my supervisor, for his consistent support and for his very responsible and strong knowledgeable guidance during the course of this work.

Finally, this thesis is dedicated to my parents. Their encouragement has motivated me throughout the course of my study.

ABSTRACT

Swirling flows are widely used in fuel burners and combustors to provide a central recirculation zone which intensifies mixing and stabilizes the flame. In general, in a flow with sufficiently high swirl entering through a sudden expansion, the change of the tangential velocity produces an axial pressure gradient and forms a back flow near the axis which results in a central recirculation zone.

In this study, the recirculation zone was measured in an experimental apparatus consisting of a sudden expansion fed by a swirl generator of the axial-tangential type, whose swirl intensity could be varied over a wide range. Three expansion ratios of 2.813, 2.0 and 1.625 were chosen in this experimental work. Velocity components at the inlet and at a number of stations downstream of the sudden expansion were measured. From the experiments, the recirculation zone was found to increase with swirl intensities and expansion ratios. Although the recirculating mass flow increases with swirl intensities, the diameter of the recirculation does not change greatly.

In order to predict the structure of the central recirculation zone in enclosed swirling flow, a simple mathematical model of the momentum integral type is developed based on assumed velocity profile shapes both at the inlet and at the location of maximum diameter of the recirculation zone. The momentum integral method is used to solve for the recirculating mass flow. To test the model parameters against the measured values, a fitting routine for model velocity profiles is also presented. The results of comparisons between the model and the experiment show that the model is satisfactory.

Chapter 1

Introduction

1.1 Background

Swirling flow is a flow with a rotating or tangential component of velocity added to the axial forward motion. It results in a spiraling motion, with tangential velocity component being imparted to the flow via the use of swirl vanes or a tangential entry. Swirling flow is encountered very often in industrial practice. In particular, it is used as an efficient approach to achieve high combustion efficiency in furnace, burners, gas turbine engines and combustors. In general, the tangential velocity component of the swirling flow decays rapidly if the flow is allowed to expand. The change of the tangential velocity, which is determined by the degree of swirl, will produce an axial-pressure gradient. When the swirl intensity is below a critical value, the adverse pressure gradient is not large enough to cause backflow. As the swirl intensity increases, the adverse pressure gradient becomes larger and at a certain value the flow undergoes a transition to a complete flow reversal near the axis. The minimum value required to produce the central recirculation is called the critical swirl intensity. If the swirl intensity is further increased, a stagnation point on the axis will be developed and followed by a region of reversed axial flow. This phenomena is referred to as vortex breakdown. The area formed by backflow at the axis of the swirl jet is called the *central recirculation zone*, distinguished from

the *corner recirculation zone* formed by a sudden expansion. They are illustrated in figure (1.1). The central recirculation zone can be used to intensify mixing and stabilize the flame. However, no explicit guides are available to design an efficient combustor. This brings the need to investigate the structure of the central recirculation zone in enclosed swirling flow.

1.2 Research Motivation and Approaches

Although swirling flow has been in use for long time, details on the structure of the recirculation zone in enclosed swirling flow remain poorly understood. The fact that swirling flow exists both in laminar and turbulent forms makes it very difficult to analyze mathematically. During the past years most studies relied on experimental approaches, for example in [27], [30]. Although several have shown the effect of swirl intensity on the recirculation zone, only Beltagui and Maccallum [3] and Rao et al. [30] have investigated the effect of expansion ratio. In recent years, numerical solutions (finite difference) were obtained for swirling flows, for example in [31]. However, very little work has been done to establish a simple mathematical model to predict the central recirculation zone in swirling flows.

This thesis is concerned with experimental work and a simple theory for the structure of the central recirculation zone in enclosed swirling flow. More specifically, we develop a simple mathematical model to predict the structure of the maximum recirculation zone in a sudden expansion and evaluate this model by experimental work. In present research, the following two approaches are taken for the study:

1. An experimental study of the structure of the central recirculation zone in a sudden expansion under conditions of non-reacting flow and axi-symmetric geometries. The effect of both the swirl intensity and the expansion ratio on the recirculation zone was investigated. The sudden expansion consisted of a 50.8 mm diameter circular throat, exiting abruptly into a test section with a

ratios of 2.813, 2.0 and 1.625. A five-hole probe was used to measure the time mean velocity components. Based on the measured velocity components, the size of the recirculation zone and the recirculating mass flow rate were obtained

2. A momentum integral type model to predict the maximum recirculating flow. By assuming simple velocity profiles at the inlet and at the maximum diameter of the recirculation zone, integral conservation equations are used to solve for the characteristics of the recirculation.

1.3 Thesis Organization

Due to the nature of this work, this thesis mainly contains two parts: experimental work and mathematical modelling. They are organized as follows:

Chapter 2, Literature Survey, summarizes the results of previous work. They are reviewed separately under experimental work and mathematical modelling.

Chapter 3, Experimental Work, describes the experimental work. It starts by introducing the experimental system. Measurement steps and data processing procedures are presented. The cause of possible errors in the experiments is also discussed.

Chapter 4, Mathematical Model, derives the momentum integral model. From the Navier-Stokes equations, three governing integral equations are derived first. To solve for the recirculation zone, assumptions for the velocity profiles at both inlet and at the maximum diameter of the recirculation zone are made. Also developed is a method for fitting inlet velocity parameters based on the corrected boundary layer.

Chapter 5, Results and Discussions, presents all the experimental and numerical results. Maps of axial and tangential velocity components obtained by the pitot probe give an clear view of the velocity profiles along downstream stations. The overall flow-field characteristics are also highlighted by the recirculation region ge-

ometries. Comparisons between the experiments and the models are given and the predictive capability of the model is also discussed.

Chapter 6, Conclusions, summaries the conclusions of the present investigation and gives recommendations for future work.

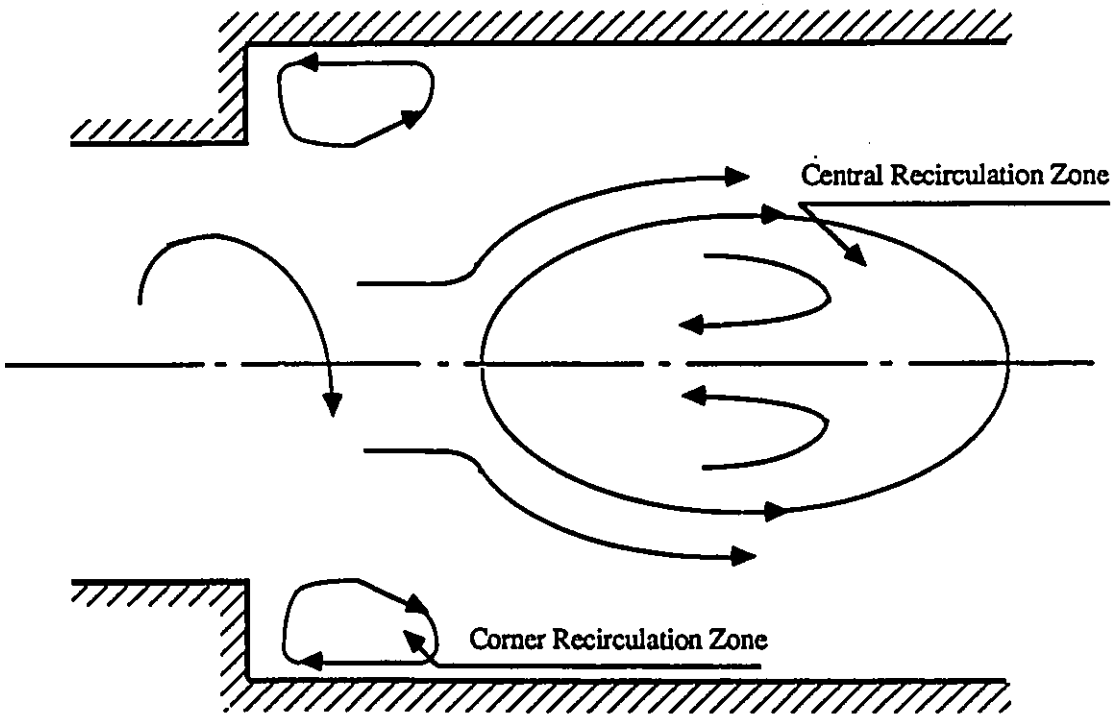

Figure 1.1: The structure of the recirculation zone

Chapter 2

Literature Survey

There exists a lot of work in the study of swirling flow in the literature. All these works served us as excellent resources of previous results, and guided us closely in the research work. In this chapter we shall review only those related to our study, namely, the central recirculation zone in a sudden expansion. Due to the nature of our work, the previous results are separately reviewed for experimental work and mathematical modelling.

2.1 Experimental Work

Swirling flows issuing from hubless and annular vane swirl generators in a sudden expansion were experimentally studied by Mathur and Maccallum [27] for various swirl intensities. In their experiments, velocity components were measured by using a three-hole probe. From the experimental results, they found that the maximum recirculating mass flow depends on the swirl number, and the maximum reverse flow velocities are similar for both types of swirl generators. They also pointed out that swirl intensity may play an important part in controlling the growth of the recirculation zone. Further studies were carried out by Beltagui and Maccallum [3]. They concluded that when the recirculation zone is set up, the maximum diameter of the recirculation zone is primarily a function of the expansion diameter and the

central recirculation zone length is also proportional to the furnace diameter for a given inlet swirl intensity.

Afrosimova [1] studied the aerodynamics of a furnace space consisting of a sudden expansion. He found that the length of the central recirculation zone and the total flow rate of the recirculation zone increase proportionally with the increase of swirl intensity.

The swirling flow in an axi-symmetric furnace with and without combustion was studied by Baker et al. in [2]. A laser anemometer was used to measure the three velocity components in isothermal flow and in a combusting mixture of air and natural gas. They concluded that the regions of recirculation are substantially different for the combusting measurements and that the turbulence is far from isotropic over most of the flow field.

The effect of combustion air swirl on the flow pattern in a cylindrical fired furnace was studied by Khalil et al. in [21]. The experiment was carried out in a cylindrical water-cooled test section with different swirl intensities imparted to the combustion air through the use of guide vane cascade swirlers. By using a pitot probe, the axial and tangential velocity components were measured to investigate the central recirculation zone. An analytical study based on the hypothesis of minimum kinetic energy was also made to relate the intensity of swirl and the radius of the central recirculation zone. The experimental results were compared to the analytical results. The size and strength of the central recirculation zone were found to increase with the swirl intensity. The analytical results were reported to agree with the experimental results quite well for normal range of swirl number and for a nearly free vortex distribution of a tangential velocity outside the central recirculation zone.

The behavior of swirling jet flames in a narrow cylindrical furnace was studied experimentally by Wu and Fricker in [38]. They observed that small swirl quantities apt to give rise to instabilities in the flow pattern and severe oscillations and

vibrations in the cylindrical furnace. The use of a double concentric air supply with the inner portion swirled gave good ignition stability together with more uniform heat fluxes.

Experimental results for swirling flow were also reported by Rhode et al. [32], who studied the swirl flow entering sudden and angled wall expansions. A collection of flow visualization photographs of the recirculation "bubbles" with different sizes and shapes was obtained and illustrated. Velocities were measured with a five-hole probe. From the results, they concluded that an increase of swirl intensity will decrease the size of the corner recirculation zone.

Dixon et al. [9] studied strongly swirled coaxial jets issuing from a divergent nozzle with a hub. They found that the recirculated mass flow rate increases with an increase of swirl intensity. They also suggested that the range of momentum flux ratios over which the central recirculation zone remains stable and symmetric without primary swirl is relatively narrow and decreases with decreasing swirl number.

The effect of various swirler vane angles on the size of recirculation zone was investigated by Rao et al. [30] for axi-symmetric enclosed swirling flows generated by vane swirlers with a hub. They found that an increase in vane angle will result in an increase in the adverse pressure gradient and the width of the recirculation zone, and a decrease of the length of the recirculation zone. They also pointed out that the axial velocity in the backflow zone increases with the swirler vane angle due to the increase in adverse pressure gradient caused by the increased swirling motion of the incoming air.

The effect of combustion in a swirl combustor was studied by Farag et al. in [13]. A flow direction detector probe was used to measure the reverse flow zone. Laser Doppler velocimetry was applied to measure the mean axial velocities. Photographs were taken to map a velocity distribution by using the spark-tracer technique. It was concluded that when the swirl number was higher than 0.5, the reverse flow

zone and axial velocity were increased by the thermal expansion due to combustion occurring in this zone. In the presence of the flame, the mean axial velocity increased inside the reverse flow zone, but owing to the effect of atomizing air, it decreased in the region near the combustor center line.

Scharrer and Lilley [34] investigated recirculation zones in test sections with blockage which can create a reverse flow, and without blockage for different expansion ratios. They found that the presence of swirl would result in the formation of a central recirculation zone and would decrease significantly the effect of the corner recirculation zone. The blockage decreases the central recirculation zone length, except for strong swirl flows with no expansion, and the degree of the effect increases as the degree of blockage increases. A reduction of the expansion ratio results in a reduction of the size of the central recirculation zone. They also found that changing the inlet from a sudden to a gradual a expansion has a minimal effect on the flow.

Swirling air flow in a stepped sudden expansion was studied by Hallett and Günther [16]. Turbulent velocity fluctuations, shear stress and mean velocities were measured for two flow regimes, namely a vortex breakdown flow at high swirl and an unsteady processing flow at low swirl. Hot-wire probes were used to determine the turbulent velocity fluctuations and shear stresses. The results showed that at the highest swirl, vortex breakdown occurs immediately after the flow leaves the throat. The turbulence in a swirling flow immediately downstream of a sudden expansion was found to be highly anisotropic, with the axial velocity fluctuations initially much larger than the other components.

The swirling flow in a non-reacting and a reacting combustor flow was studied by Brum and Samuelsen in [5] using a two-component laser anemometer. Reynolds stress, rms axial and azimuthal velocities were directly measured. From the experiments, they studied the effect of reaction on the flow structure and examined the small-scale dynamics associated with strong swirl-stabilized reacting and non-reacting flows.

The effects of inlet conditions and expansion ratios on the onset of flow reversal in swirling flow in a sudden expansion were investigated by Hallett and Toews [18]. Experimental results showed that the critical swirl number required to produce a central recirculation zone in a sudden expansion is determined by both the expansion ratio and inlet velocity profile shape. An inlet tangential velocity distribution with a large solid body vortex core or an axial velocity profile with a maximum on the axis was found to lead to a higher critical swirl.

Similarly, the effect of a central hub on the onset of flow reversal in a swirling sudden expansion was investigated by Tavasoli [37]. A five-hole probe was used to measure velocity components. He found that the addition of a hub produces a considerable reduction in critical swirl, as the momentum deficit in the hub wake lowers the pressure gradient necessary for stagnation. He also found that the inlet velocity profiles were substantially independent of expansion ratio. As the hub radius increases, the potential vortex is reduced to a thin layer near the outer wall; the tangential velocities near the hub are reduced below those of pure solid body rotation, and the axial velocities develop a pronounced maximum at the hub wall.

Lastly, a report by Syred and Beer [36] is a review of the work on swirling flows before 1974. Many references not mentioned here can be found in that report.

Although several authors have showed the effect of swirl strength on the recirculation zone, eg., Mathur and Maccallum [27], Wu and Fricker [38], Rao et al. [30], Rhode et al. [32], only Beltagui and Maccallum [3] and Rao et al. [30] have looked at the effect of expansion ratio as well. therefore, there is the need for further study.

2.2 Mathematical Model

Mathematical modelling of swirling flows has mainly used three approaches namely analytical solutions, simple closed form models based on the momentum integral method and finite difference computations.

Chow [8] reported analytical solutions to several classes of breakdown phenomena in a fluid swirling through an axi-symmetrically deformed tube. With simplifying assumptions, he first reduced the governing equations to a single one, with a solution in terms of Bessel functions. He concluded that as the swirl intensity increases, the number of recirculation zones increases as well.

Bossel [4] studied the behavior of swirling flow at high swirls in streamtubes of variable cross section by employing the method of weighed residuals. To solve for the swirling flow issuing into an expansion, Bessel functions were used. A relationship was obtained to predict the critical expansion ratio at which stagnation on the axis occurs for a given swirl.

Momentum integral techniques have also been used to predict swirling flows. By assuming simple functional forms for the radial variations of the velocities, integrated forms of the governing equations in the radial direction can be solved for parameters defining the velocity profiles. Among these works, Morton [29] presented a mathematical analysis to study the effect of swirl strength and angle of diffuser on the size of the recirculation zone inside a diffuser. In his analysis, the axial velocity distribution was represented by a single family of curves, and the tangential velocity was assumed to be a solid body rotation. A momentum integral method was used to simplify the differential equations. It was found that an increase in both swirl and angle of divergence enhances the recirculation zone, while mass addition along the combustor decreases both the strength and size of recirculation, especially at higher swirl strengths. A similar study was also reported by Domkundwar et al. [10], who concluded that an increase in swirl strength and diffuser angle accentuated recirculation. On the other hand, combustion and mass addition inhibited recirculation.

The viscous core of an incompressible swirling flow through a nozzle was studied by Mager [24]. In his study, the momentum integral equations were used together with a statement of conservation of mass in the whole nozzle and conservation of momentum along the nozzle axis to get a set of four ordinary nonlinear differential

equations. These equations were solved for circumferential and axial velocities both inside and outside the core. Two possible solutions in which the core is swirl and massflow dominated were found. He concluded that the massflow dominated core occurred at low swirl and was characterized by a high discharge coefficient. The swirl dominated flows have the capability to sustain very large total pressure losses, and usually have regions of reversal axial velocity. An increase of Reynolds number tends to decrease the discharge coefficient. The study was applied further in [25] to solve quasi-cylindrical momentum integral equations for the dissipation and breakdown of wing-tip vortex.

The momentum integral method to predict the swirl in a sudden expansion has also been used in recent years. Hallett [19] developed the first simple momentum integral model to estimate the critical swirl in a sudden expansion. The momentum integral model was established from the conservation of mass and momentum as well as the condition for stagnation of the flow on axis. In his derivation, a Rankine vortex was used to approximate the tangential and the axial velocities at inlet; a parabolic assumption for axial velocity profile and a solid body vortex followed by a constant value near the wall for the tangential velocity profile at the greatest extension of the backflow were also used. Based on those assumptions, an explicit expression for the inlet critical swirl needed to initiate downstream flow reversal was obtained. The critical swirl was found to be a function of the expansion ratio and inlet velocity profiles. Further studies on the effect of a central hub on the critical swirl in a swirling sudden-extension flow were carried out by Hallett and Tavasoli [20], in which the momentum integral model was extended to approximate the critical swirl in a flow with a hub. A modified Rankine vortex was employed to model velocity profiles at inlet. An explicit expression was obtained for the critical swirl as a function of geometry and inlet conditions, in particular the hub size and the shape of the axial velocity profiles.

With the development of computers, the finite difference method was used to study the swirling flow in combustion chambers. Complete solutions to swirling flow

fields have been obtained with finite difference methods for a variety of geometries and inlet conditions in recent years. Rhode et al. [31] predicted the effect of swirl intensity and turbulence intensity of the inlet flow on swirling jets issuing into an expansion as well as the effect of expansion side wall angle by using finite difference methods to solve the turbulent Reynolds equations for conservation of mass and momentum. Although the predictions did not match the experimental data close to the inlet region, the agreement was very good after two throat diameters. Chattree et al. [7] did calculations for isothermal turbulent swirling flow inside an asymmetric combustor using a finite volume approach along with the SIMPLE algorithm to solve the governing equations. Application of the procedure to model combustor reveals the importance of various parameters such as the swirl number and inlet swirl velocity profiles.

Kubo and Gouldin [23] solved the governing equations by using a numerical procedure for determining the effect of swirl strength on the size and location of the recirculation zone in isothermal flows. They found that increasing the swirl strength increased the recirculation zone size and moved the stagnation point towards the swirler.

Dixon et al. [9] used a numerical solution to predict the flow of strongly swirled coaxial jets issuing from a divergent nozzle with hub. A two-equation effective viscosity turbulence model was incorporated. By comparing with experimental results, he found that the numerical solutions can adequately represent the measured quantities.

Theoretical investigations of vane-generated swirling flows in a circular chamber were presented by Rao et al. in [30]. A finite difference method was used to predict the three velocity components. They found that the predicted results were in reasonable agreement with the measurements except close to the nozzle.

Alothough the finite difference method was used resently, the momentum integral model can give us a clear physical meaning to describe the recirculating flow.

Chapter 3

Experimental Work

In order to study the structure of the central recirculation zone, a series of experiments were performed in a sudden expansion flow section as shown in figure (3.1). The experimental system consists of three major parts: the swirl generator, the test section, and the probe measurement system. Since each of these subsystems is important for the experiment, we will describe them individually in the following sections.

3.1 Swirl Generator

The heart of the experimental rig is the swirl generator. In this experiment, a tangential plus axial swirl generator, shown in Figure (3.1), is used, a modification of the design of Hallett [17]. Swirl is produced by admitting air through four tangential inlets of length L. The angular momentum imparted to the flow can be controlled by means of a sliding sleeve which changes the value of L. Each tangential port is equipped with a moveable partition attached to the sleeve and a bell-mouthed entry in order to produce a uniformly distributed inlet velocity. By admitting a secondary non-swirling stream of air to the system (hereafter referred to as "axial air"), the swirl intensity of the resulting flow can be reduced. By regulating the proportions of air introduced tangentially and axially as well as the length L, both

the swirl intensity and the shape of the axial velocity profile at the swirler exit can be varied [17]. Flow nozzles of ASME pattern are used to measure the axial and tangential mass flows.

The mass flow rate of air delivered through each nozzle can be controlled independently by using a pair of sliding gates. Each of the flow rates is monitored by a water manometer placed at an 8.73 degree slope. A blower draws air through the test rig, and the total mass flow rate can also be controlled by a sliding gate at the entrance to the blower. The air is exhausted to the outside by a long circular duct.

Before entering the swirl generator, the tangential part of the air has to pass through a cloth filter where both dust and larger eddies of turbulent flow are trapped, resulting in cleaner and more uniform air delivery to the swirl generator [37].

3.2 Test Section

To study the behavior of swirling flow issuing into sudden expansions, three different cylindrical test sections are used. Each section is connected with its own flanges at each end. One end is joined to the swirl generator throat, and the other is joined to a circular duct followed by a flexible hose leading to the exhauster fan. The throat radius of 50.8 mm is kept constant throughout the investigation.

Three expansion sections with diameters of 0.165, 0.203, and 0.286 m, corresponding to expansion ratios r_2/r_1 of 1.625, 2.0, and 2.813, are used to study the effect of the expansion ratio on swirling flow. These expansion sections are made of *Plexiglas* tube, so that flow visualization can be performed. A number of ports are provided along the test section wall to allow probe to be inserted to measure velocity profiles at various downstream locations.

3.3 Probe Measurement System

A five-hole Pitot probe was chosen to measure the velocity vector components and the static pressure. The probe measurement system consists of a five-hole probe and a valve board. The operational mechanism of the valve board is shown in figure (3.2).

3.3.1 Five-Hole Probe and Measurement Configuration

The five-hole probe has five holes arranged as shown in figure (3.3). The probe tip diameter is approximately 3 mm. A protractor is attached on the probe to measure the pitch angle of the probe. Capacitive pressure transducers of 10 and 100 Torr range are used to measure the pressure differences between the holes. Generally, the dynamic responses of the pressure probe and transducer system are too slow to allow for instantaneous pressure measurements. Therefore, the three components of mean velocity and the static pressure are measured.

The probe is fastened to a holder by means of two clamping screws. The holder is fixed onto a traversing slider by supports of adjustable height. The slider is used to measure the radial location of the probe. The setup of the probe, slide and probe insertion in the throat area is similar to those in [37].

The probe is operated in the null mode: it is rotated about its shaft until the pressure difference $(p_3 - p_2) = 0$, at which point the probe lies in the plane of the velocity vector, and the pitch angle is read off the protractor on the probe shaft. The remaining three pressure differences, namely (p_1 - p_2), (p_4 - p_5) and (p_1 - p_w), are then measured, p_w being the pressure measured at a tap mounted on the wall opposite the probe. The yaw angle, χ, is related to the pressure coefficient B, by means of a calibration curve. B is defined as:

$$B = \frac{p_4 - p_5}{p_1 - p_2} \tag{3.1}$$

The static and total pressure are then calculated by using two further coefficients

$$COEFV = \frac{p_t - p_s}{p_1 - p_2}, \tag{3.2}$$

$$COFTP = \frac{p_1 - p_t}{p_t - p_s}. \tag{3.3}$$

3.3.2 Probe Calibration

The probe is calibrated in a non-swirling jet of known characteristics, issuing from an ASME nozzle. The calibration procedures were developed by McGrath [28] and are described in more detail in [37]. The probe tip is placed at the center of the potential core of the jet and the yaw angle, χ, is defined as the angle between the normal to the nozzle centerline (i.e., the flow direction) and a normal to the probe shaft. The required pressure differences $(p_4 - p_5)$, $(p_1 - p_2)$, $(p_1 - p_t)$ and $(p_t - p_{atm})$ are measured, where p_1, p_2, p_3, p_4 and p_5 refer to the pressures at the probe holes 1, 2, 3, 4 and 5. The total pressure of the jet p_t, is the nozzle back pressure in the calibration unit, and p_{atm} represents the barometric pressure which is also the static pressure in the jet. The probe was calibrated at both high and low nozzle velocities (13 and 41 m/s) to check for a Reynolds number dependence of the calibration, but none was found.

The results are plotted in the form of calibration curves in Figs. (3.4) to (3.5).

- $(p_4 - p_5)/(p_1 - p_2)$ vs. yaw angle, so that the yaw angle can be determined.
- $(p_t - p_{atm})/(p_1 - p_2)$ vs. yaw angle, so that the velocity pressure coefficient, $COEFV$, can be calculated from the yaw angle.
- $(p_1 - p_t)/(p_t - p_s)$ vs. yaw angle, so that the total pressure coefficient, $COFTP$, can be predicted from the yaw angle.

Each of these curves is then fitted by a ninth degree polynomial [37].

$$\chi = \begin{cases} (B + 0.166)/(0.0326) & \text{if } B \leq 0.1779 \\ (B + 0.300)/(0.0453) & \text{if } B > 0.1799 \end{cases} \tag{3.4}$$

$$COEFV = 0.957 + (2.406 \times 10^{-3}\chi) - (1.69 \times 10^{-4}\chi^2) - (4.108 \times 10^{-7}\chi^3) + (3.069 \times 10^{-7}\chi^4) + (0.898 \times 10^{-9}\chi^5) - (0.172 \times 10^{-9}\chi^6) - (0.127 \times 10^{-11}\chi^7) + (0.394 \times 10^{-13}\chi^8) + (0.45 \times 10^{-15}\chi^9) \quad (3.5)$$

$$COFTP = -0.414 \times 10^{-2} - (2.027 \times 10^{-4}\chi) - (1.657 \times 10^{-4}\chi^2) - (4.862 \times 10^{-6}\chi^3) - (6.963 \times 10^{-7}\chi^4) + (0.121 \times 10^{-7}\chi^5) + (0.51 \times 10^{-9}\chi^6) - (0.996 \times 10^{-11}\chi^7) - (0.123 \times 10^{-12}\chi^8) + (0.288 \times 10^{-14}\chi^9) \quad (3.6)$$

3.4 Probe Measurement Errors

In turbulent flow a probe is subject to varying velocity magnitude, static pressure and pitch and yaw angles. All these forms are well-known sources of errors in five-hole probe measurements.

In regions with a high velocity gradient, the effect of shear on the five-hole probe is significant and can be expected to result in an error in the direction of the velocity vector proportional to the shear parameter. Mahmud et al. [26] found this to yield higher axial velocities and lower tangential velocities [26]. A pressure gradient will also yield errors in the measurement of velocities; in the direction of the pressure gradient, the velocity component will be overestimated [6].

The alignment of the probe is a necessary step in the measurement of flow direction. The probe can be aligned with the flow within a small angle difference ($\pm$ 0.5 degree) and the pitch angle is usually considered to be the most accurate quantity measured by the probe. However, the effects of velocity shear mentioned earlier can lead to errors in pitch angle. In turbulent flow, a probe is subject to varying yaw and pitch angles; however, the maximum yaw and pitch angles to which the five-hole probe operates are limited to within about $\pm$ 40 degrees. Consequently, experimental problems arise when the flow directions are highly variable [15], such as in highly turbulent flow.

The influence of turbulence is another source of errors in the measurements. Its effect is known to be significant at high turbulence intensities and will result in higher measured dynamic pressures and velocities, with an error proportional to the square of turbulence intensities [26]. However, five-hole probes are still frequently employed for turbulent flow measurements and the effect of turbulence on the probe is often ignored [15], since no reliable correction procedures have been developed.

The use of the probe in the measurements will also cause errors due to probe disturbance such as perturbations of the flow field. A well-known example of such perturbation is probe blockage, which can be especially severe in flows that are characterized by complex flow patterns [15]. When the probe traverses the flow field, the probe blockage increases and may result in flow asymmetries. The presence of the probe may also cause interference such as the generation of secondary flows, tripping of flow instability and local flow changes. However, the occurrence of disturbance is dependent on the probe geometry and its location in the flow field and flow conditions. Evidence in the literature indicates that perturbations may or may not occur depending on flow conditions and probe design. For example, a comparison between velocity measurements made with probes and laser velocimetry showed that the differences do not suggest probe perturbations [15]. The amount of disturbance increases with probe size. In the present experiments, the probe diameter was 3 mm, and the ratio of probe area to flow area with the probe fully inserted was about 2.3×10^{-2} to 1.3×10^{-2}. Therefore, the disturbance of the probe should be small.

Leakage in the apparatus is also a possible error source. Since the whole system is under suction, any leakage into the main box would result in a higher mass entry into the system than measured by the manometers. In the expansion section, any leakage would result in a higher radial velocity and complex effects on the axial and tangential velocity profiles. Depending on the location of the leakage, it would also lead to a possible flow measurement error. To minimize the leakage, flange connections and every joint that could cause leakage are heavily sealed.

Although there are many of sources of errors in the probe measurements, by using properly designed procedures and working carefully we can still control the error within certain ranges. The overall error in our experiment was estimated by comparing the mass flows integrated from axial velocity profiles with the metered mass flows. The differences are considered as representative to the errors of the velocity measurements. In order to minimize the error, dimensionless quantities based on the integrated mass flow are used. Under the assumption that all the errors (i.e., in velocities) are in the same proportion as the total mass flow, the use of dimensionless quantities can partially cancel the errors caused by turbulence and probe effects.

3.5 Data Reduction Program

To obtain the three dimensional velocities and the static pressure from the five hole probe measurements, a FORTRAN program based on one originally developed by McGrath [28] was used in Appendix A. More details of the definitions of parameters are given in [37].

The following data is recorded, in order to initiate the program.

- Room Temperature in ^{o}C.
- Barometric pressure in $mmHg$.
- The local density of air, ρ, is calculated from the ideal gas law.
- The tangential and axial mass flow rates are calculated from the two manometer readings by using the following equations [37].

$$\dot{m}_t = 7.836 \times 10^{-3} \sqrt{(p_{atm} - \frac{p_{tan}}{133.32}) \frac{p_{tan}}{T}}, \tag{3.7}$$

$$\dot{m}_a = 1.9056 \times 10^{-3} \sqrt{(p_{atm} - \frac{p_{ax}}{133.32}) \frac{p_{ax}}{T}}. \tag{3.8}$$

where $\dot{m}_t$ and $\dot{m}_a$ correspond to the mass flow rate through the tangential and axial gates.

- The total mass flow rate entering the system is $(\dot{m}_t + \dot{m}_a)$.
- The probe error is estimated by comparing the total mass flow rate with that obtained from the integration of the probe measurements.

3.5.1 Integral Quantities

In addition to the mentioned quantities, a number of integral quantities were calculated by numerical integration of the measured velocity profiles using the trapezoid rule, so that a better understanding of the flow could be achieved. These are:

- Mass flow rate at the throat

$$\dot{m} = 2\pi \int_0^{r_1} \rho u r \, dr. \tag{3.9}$$

- The recirculated mass flow rate

$$\dot{m}_r = 2\pi \int_0^{r} \rho(\mid u \mid -u) r \, dr \tag{3.10}$$

When there is a backflow velocity, $(\mid u \mid -u)$ equals $2u_{back}$, otherwise it equals zero.

- Stream function

$$\Psi = \frac{\int_0^r \rho u r dr}{\int_0^{r_1} \rho u r dr} \tag{3.11}$$

- The axial flux of axial momentum

$$G_x = 2\pi \int_0^r \rho u^2 r \, dr; \tag{3.12}$$

and in dimensionless form

$$G = \frac{G_x}{\dot{m}\bar{u}_{ref}}. \tag{3.13}$$

Here the mass flow $\dot{m}$ integrated from the axial velocity profile is used to calculate dimensionless quantities rather than the mass flow determined from

the flow meters in order to roughly cancel probe error in measured quantities such as G_x. $\bar{u}_{ref}$ is the reference axial velocity, given by

$$\bar{u}_{ref} = \frac{Q}{\pi r^2}. \tag{3.14}$$

where Q is the volumetric flow rate at the throat.

- The angular momentum flux

$$G_\phi = 2\pi \int_0^r \rho u w r^2 \, dr; \tag{3.15}$$

and the dimensionless form

$$\Omega = \frac{G_\phi}{\dot{m}\, r_1 \bar{u}_{ref}}. \tag{3.16}$$

- The angular momentum flux stream function

$$\Psi_\phi = \frac{2\pi \int_0^r \rho u w r^2 \, dr}{G_\phi}. \tag{3.17}$$

- The swirl number

$$S = \frac{G_\phi}{r_1 G_x}. \tag{3.18}$$

S and Ω are two alternative parameters for characterizing the swirl intensity. The swirl number is used more often in the literature, but Ω has the advantage that it depends only on the form of the tangential velocity profiles.

- The Reynolds Number

$$Re = \frac{2 r_1 \bar{u}_{ref}}{\nu}. \tag{3.19}$$

3.6 Experimental Procedures

After initializing the system, the experiment was conducted according to the following procedures.

1. Axial and tangential flows were set to the desired swirl level. At each setting, flow visualization using $TiCl_4$ fume [37] was performed to check that a steady recirculation zone existed in the flow.

2. The five-hole probe was inserted into the flow to measure the three velocity components and the local static pressures at the inlet station and a number of stations downstream after the flow conditions were set.

3. The atmospheric temperature, pressure and the readings LA and LT of the axial and tangential manometer readings connected to the flow metering nozzles were recorded.

4. The opening plugs were sealed completely after the probe was inserted into the flow and the whole apparatus system checked thoroughly again for any possible leakage.

5. The probe was aligned with the flow by rotating the probe until the pressure difference $(p_2 - p_3)$ was zero. Once the probe was aligned, the pitch angle could be read from the attached protractor.

6. The pressure differences $(p_4 - p_5)$, $(p_1 - p_2)$ and $(p_1 - p_w)$ were measured by changing the valve positions on the valve board at this pitch angle.

7. Measurements were taken radially, starting from a point near the test section wall surface and proceeding toward the axis by operating the traversing slider. The measurement points were taken at intervals of 5 mm. The "swan neck" of the probe head does not allow the probe to approach the rear wall closely, so measurements are taken between the axis and the wall farthest from the probe port.

8. Only one measurement of $(p_1 - p_{atm})$ is taken at each measurement station. The value of $(p_1 - p_{atm})$ is used to obtain the wall pressure $(p_w - p_{atm})$ from the measured $(p_1 - p_w)$.

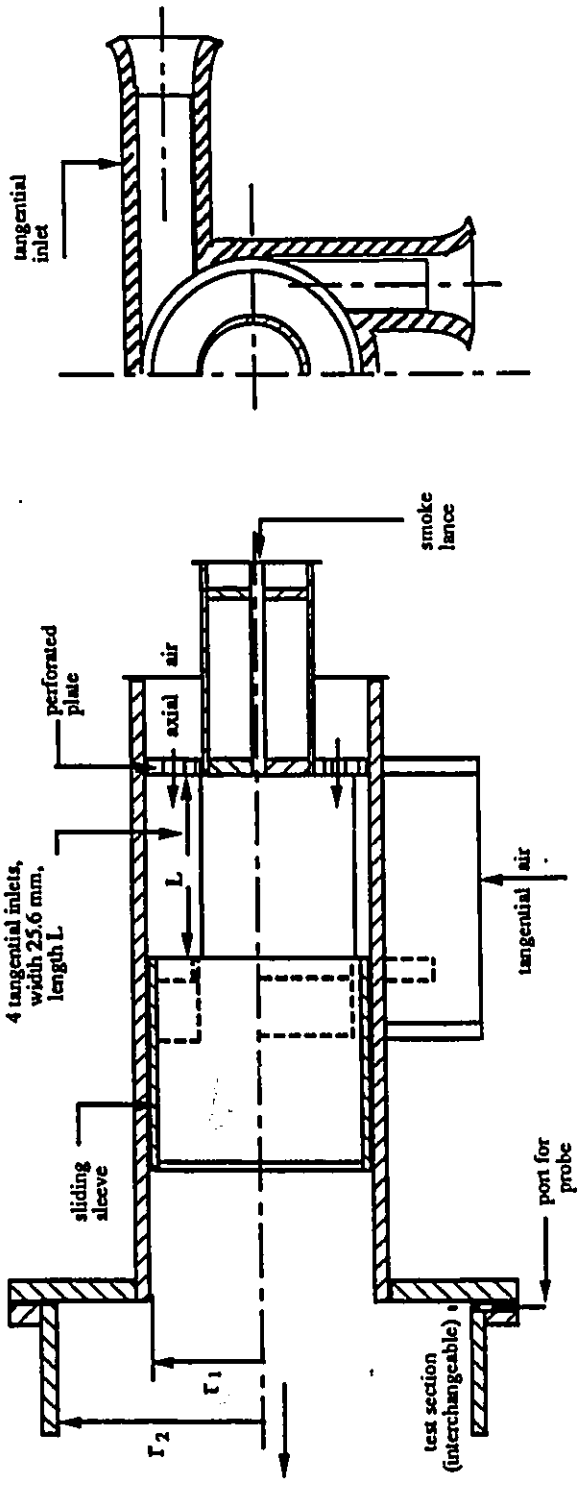

Figure 3.1: Experimental System

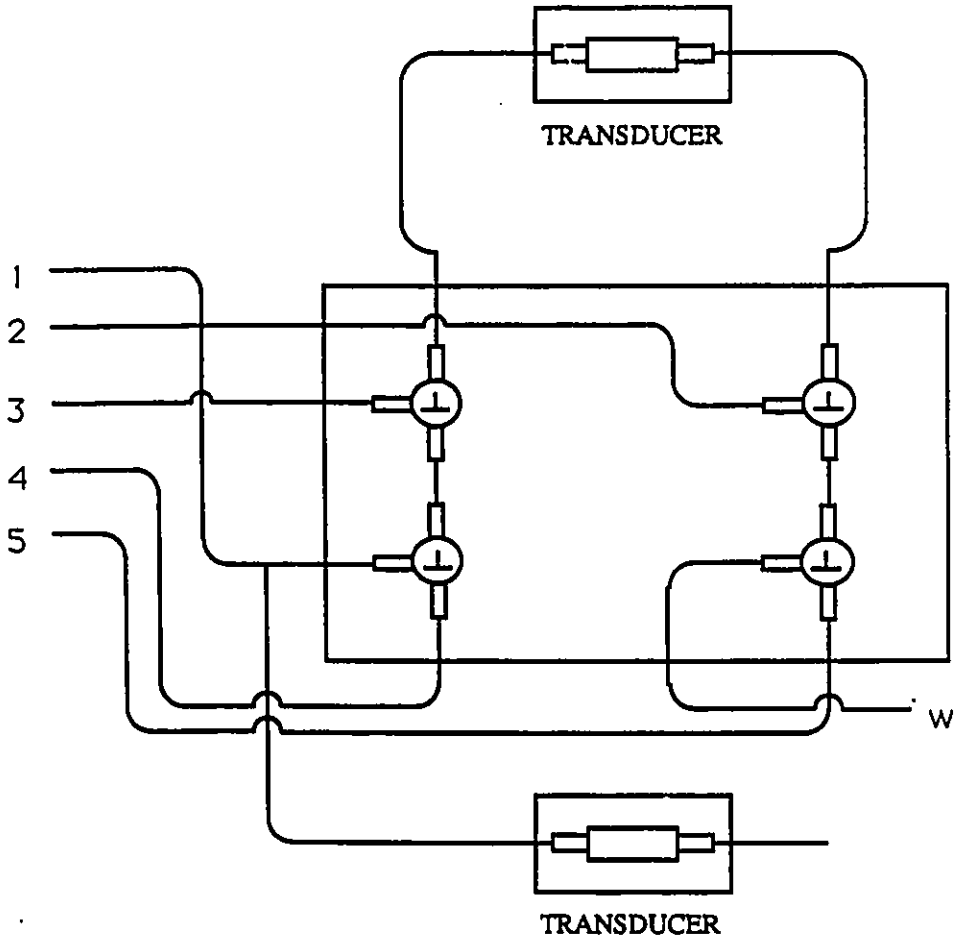

Figure 3.2: Valve Board

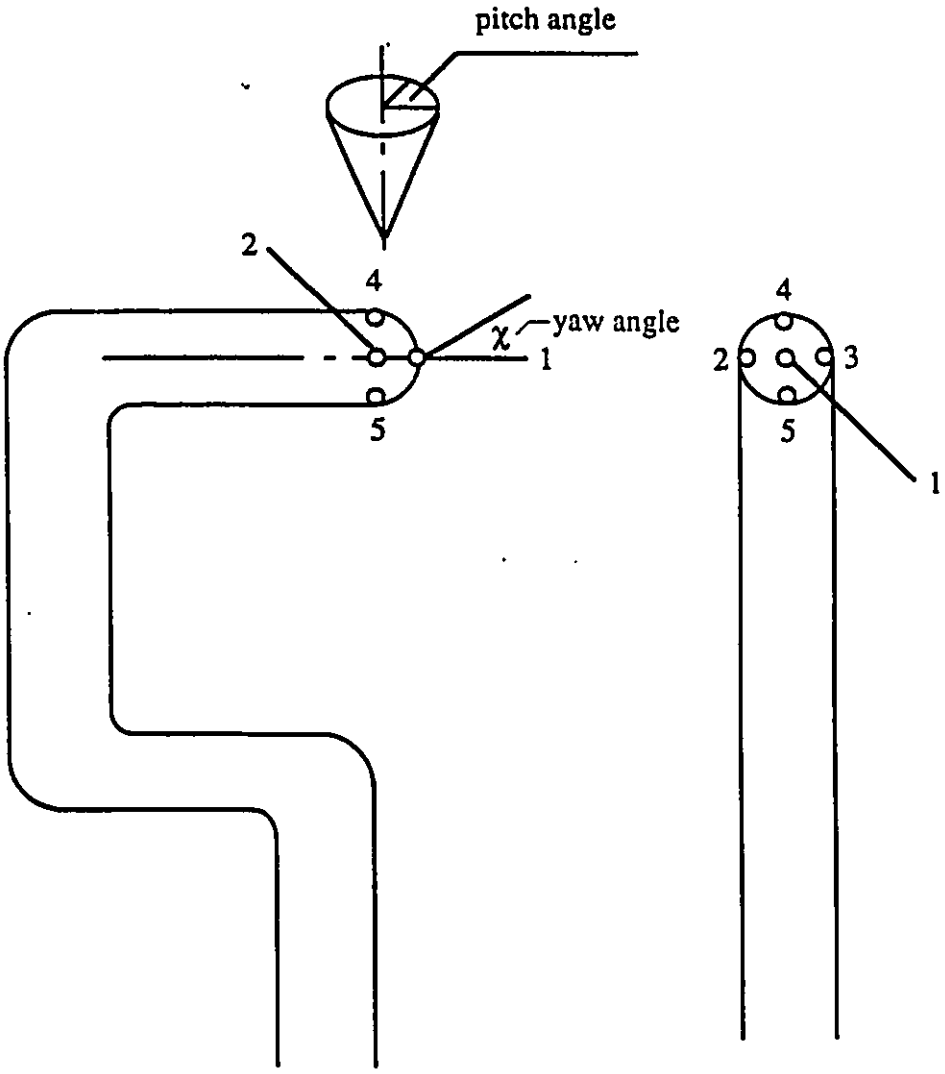

Figure 3.3: Five-Hole Probe

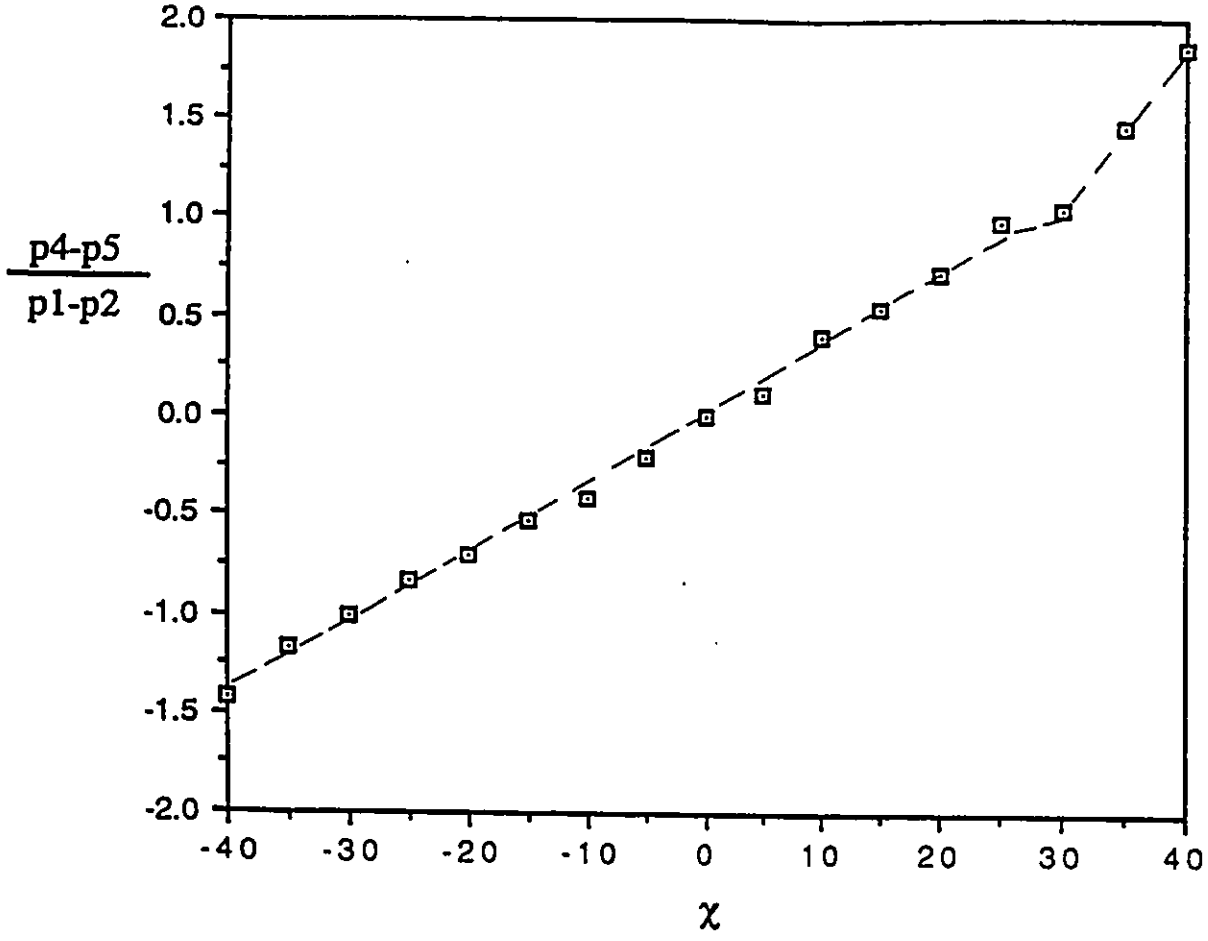

Figure 3.4: B vs. χ

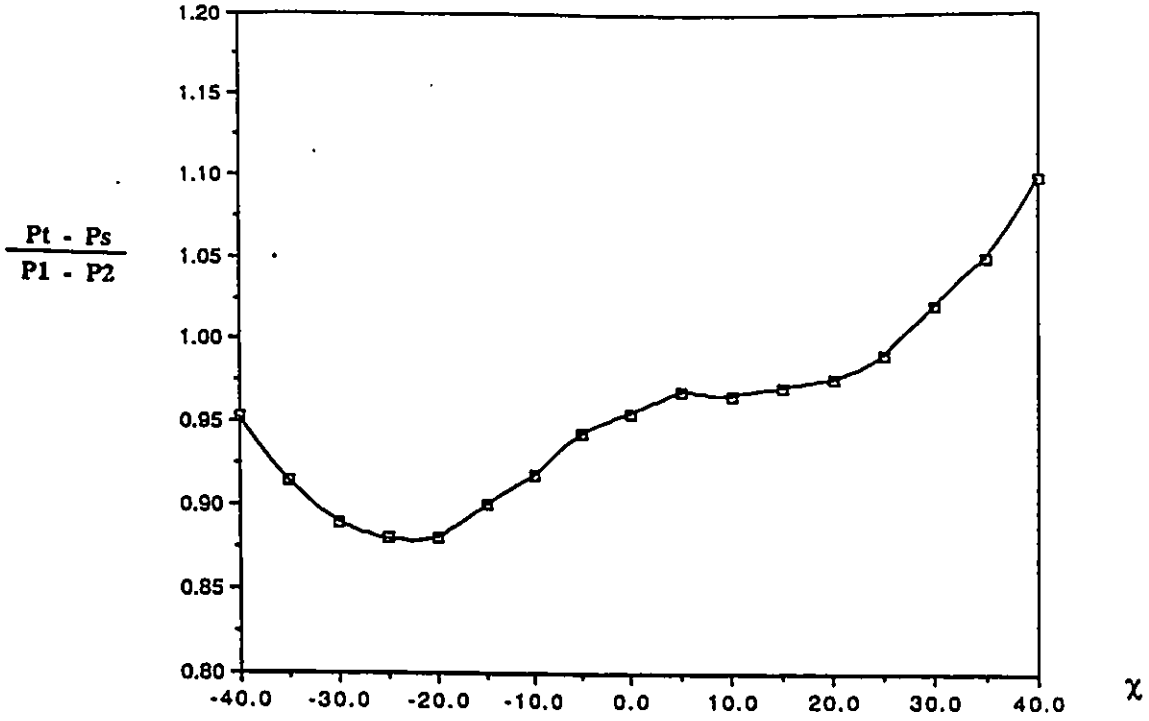

Figure 3.5: COEFV vs. χ

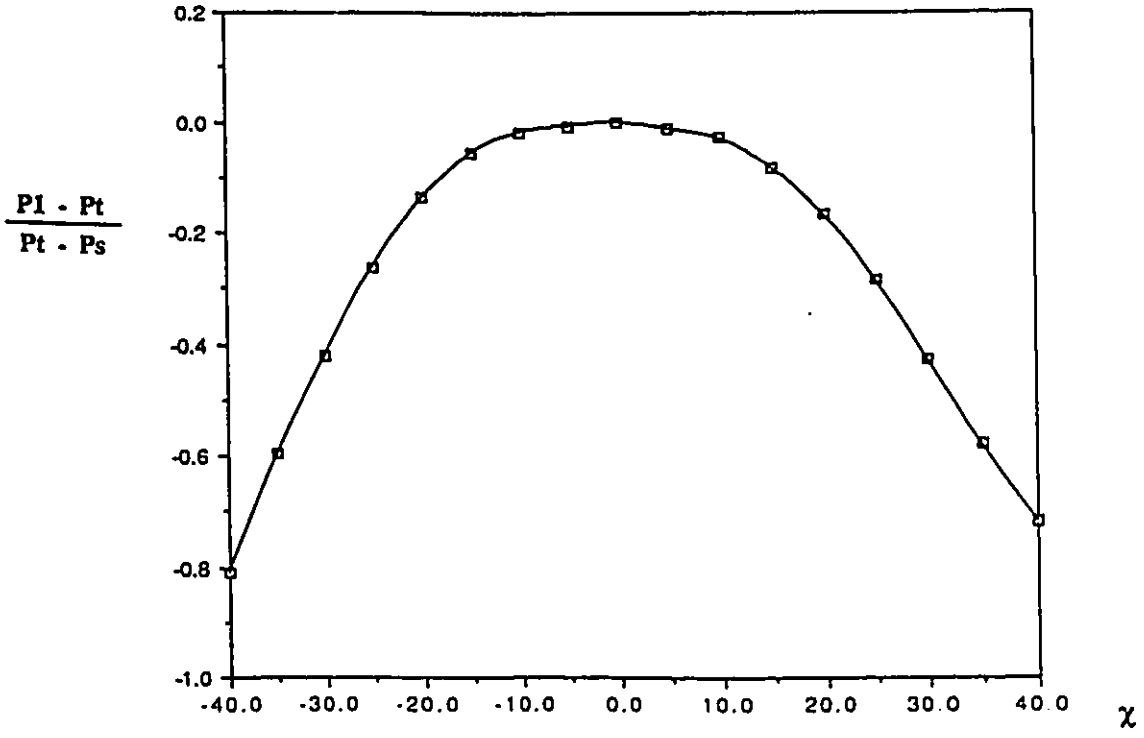

Figure 3.6: COFTP vs. χ

Chapter 4

The Mathematical Model of the Recirculation Zone

In this chapter, we develop a mathematical model of the recirculation zone. A back flow condition that the swirl number is larger than the critical is considered. Based on a previous study of the critical swirl by Hallett [19], we derive a mathematical model of the recirculation zone by using the Rankine vortex model for the velocities at the inlet and a parabolic assumption for the axial velocity at the location of the largest diameter of the recirculation zone. In order to solve for the back flow velocities, two sets of Bernoulli equations are established by the condition for stagnation of the flow on the axis. The momentum integral method is employed to solve for the recirculating mass flow. To test the model parameters against the measured values, a fitting routine for model velocity profiles is also set up.

4.1 Mathematical Model Description

The mathematical model used to predict the size of the recirculation zone is a momentum integral description of the flow, in which velocity profiles approximating those in the real flow are required to satisfy integral conservation of mass, momentum and angular momentum. The assumed profile shapes are shown in figure (4.1). Station 1, representing the inlet conditions, is located just downstream of

the step, so that pressure forces on the end wall need not be taken into account. (Pressure forces at station 1 and station 2 are accounted for.) The profiles here are defined by the parameters a_1, u_1, λ and Γ_1. Station 2 is located at the plane of the largest diameter of the recirculation zone, or the largest recirculating mass flow. Parameters used to describe the flow conditions at this station are u_{02} (the backflow velocity), Δu, w_2 and a_2. By employing the momentum integral method, in which the equations of motion are integrated over the control volume between station 1 and station 2, we solve for these parameters and hence describe the behavior of the recirculation zone.

4.2 Derivation of the Governing Equations

There are three governing equations, namely the integral equations of conservation of mass, tangential and axial momentum, which are used to describe the swirling flow in our model. They are derived directly from the Navier-Stokes equations and the continuity equation in cylindrical coordinates, which are:

r-component

$$\rho\left(\frac{\partial v}{\partial t}+v\frac{\partial v}{\partial r}+\frac{w}{r}\frac{\partial v}{\partial \theta}-\frac{w^2}{r}+u\frac{\partial v}{\partial x}\right)= -\frac{\partial p}{\partial r}+\mu\left[\frac{\partial}{\partial r}\left(\frac{1}{r}\frac{\partial (rv)}{r\,\partial r}\right)+\frac{1}{r^2}\frac{\partial^2 v}{\partial \theta^2}-\frac{2}{r^2}\frac{\partial w}{\partial \theta}+\frac{\partial v^2}{\partial x^2}\right]+\rho g_r; \tag{4.1}$$

θ-component

$$\rho\left(\frac{\partial w}{\partial t}+v\frac{\partial w}{\partial r}+\frac{w}{r}\frac{\partial w}{\partial \theta}+\frac{vw}{r}+u\frac{\partial w}{\partial x}\right)= -\frac{1}{r}\frac{\partial p}{\partial \theta}+\mu\left[\frac{\partial}{\partial r}\left(\frac{1}{r}\frac{\partial (rw)}{\partial r}\right)+\frac{1}{r^2}\frac{\partial^2 w}{\partial \theta^2}+\frac{2}{r^2}\frac{\partial v}{\partial \theta}+\frac{\partial^2 w}{\partial x^2}\right]+\rho g_\theta; \tag{4.2}$$

x-component

$$\rho\left(\frac{\partial u}{\partial t}+v\frac{\partial u}{\partial r}+\frac{w}{r}\frac{\partial u}{\partial \theta}+u\frac{\partial u}{\partial x}\right)= -\frac{\partial p}{\partial x}+\mu\left[\frac{1}{r}\frac{\partial}{\partial r}\left(r\frac{\partial u}{\partial r}\right)+\frac{1}{r^2}\frac{\partial^2 u}{\partial \theta^2}+\frac{\partial^2 u}{\partial x^2}\right]+\rho g_x; \tag{4.3}$$

and the continuity equation

$$\frac{\partial \rho}{\partial t} + \frac{1}{r}\frac{\partial(\rho r v)}{\partial r} + \frac{1}{r}\frac{\partial(\rho w)}{\partial \theta} + \frac{\partial(\rho u)}{\partial x} = 0 \tag{4.4}$$

where g_x, g_θ, g_r are gravitational terms in the three directions. The following assumptions are made for the model:

- Flow is assumed to be incompressible and inviscid.
- Flow is assumed to be axi-symmetric.
- Flow is assumed to be steady and isothermal.
- Gravitational effects are neglected.

Applying these assumptions to the above equations and simplifying them, we get

$$\frac{\partial(ur)}{\partial x} + \frac{\partial(vr)}{\partial r} = 0. \tag{4.5}$$

$$\frac{\partial(uv)}{\partial x} + \frac{\partial(v^2)}{\partial r} + \frac{v^2}{r} - \frac{w^2}{r} = -\frac{1}{\rho}\frac{\partial p}{\partial r} \tag{4.6}$$

$$\frac{\partial(u^2 r)}{\partial x} + \frac{\partial(ruv)}{\partial r} = -\frac{r}{\rho}\frac{\partial p}{\partial x}. \tag{4.7}$$

$$\frac{\partial}{\partial x}(r^2 uw) + \frac{\partial}{\partial r}(r^2 vw) = 0. \tag{4.8}$$

Equations (4.5), (4.6), (4.7) and (4.8) are now integrated over the cross section of a cylindrical tube of radius r_2. The boundary conditions are given by

$$u = v = w = \frac{\partial u}{\partial x} = \frac{\partial v}{\partial x} = \frac{\partial w}{\partial x} = 0. \qquad at\ r = r_2 \tag{4.9}$$

while at the axis symmetry requires that

$$v = w = \frac{\partial u}{\partial r} = \frac{\partial v}{\partial r} = \frac{\partial}{\partial r}(\frac{w}{r}) = 0 \qquad at\ r = 0 \tag{4.10}$$

Integrating equation (4.5) and applying Leibniz' rule leads to

$$\frac{d}{dx}\int_0^r ur\,dr = 0. \tag{4.11}$$

This shows that the volume flow rate is constant.

At the inlet, and again at the station where the recirculation reaches its largest extent, the radial velocity v will be negligible. Such an assumption is supported by the radial velocity profiles measured in the present experiments (chapter 3) and those reported by Mathur and Maccallum [27] and Rao et al. [30]. Then, from equation (4.6) we have

$$\frac{\rho w^2}{r} = \frac{\partial p}{\partial r} \tag{4.12}$$

The condition for preservation of the "thrust" (axial momentum flux plus the pressure force) in the absence of friction is given by the integration of equation (4.7)

$$\frac{d}{dx}(\int_0^r \rho u^2 r\, dr + \int_0^r pr\, dr) = 0. \tag{4.13}$$

Similarly, equation (4.8) integrates to conservation of angular momentum flux:

$$\frac{d}{dx}(\int_0^r \rho uwr^2\, dr) = 0. \tag{4.14}$$

As a summary, the integral equations of the motion of the swirling flow used in our model are shown as follows

$$\int_0^r ur\, dr = const., \tag{4.15}$$

$$\int_0^r \rho u^2 r\, dr + \int_0^r pr\, dr = const., \tag{4.16}$$

$$\int_0^r \rho uwr^2\, dr = const.. \tag{4.17}$$

4.3 Derivation of the Mathematical Model

In this section, we solve for the components of velocities and other properties, such as mass flow rates etc. by assuming simple expressions for velocity profiles which approximate those in the real flow, and use these to carry out the integrations. The

upstream tangential velocity is modelled as a Rankine vortex [19] with solid body core radius a_1 as shown in Fig.(4.1).

$$w = \frac{\Gamma_1 r}{a_1^2} \qquad 0 \leq r \leq a_1 \tag{4.18}$$

$$w = \frac{\Gamma_1}{r} \qquad a_1 < r \leq r_2 \tag{4.19}$$

while the axial velocity is given by

$$u = u_1 \left[\lambda - (\lambda - 1)\frac{r}{a_1}\right] \qquad 0 \leq r \leq a_1 \tag{4.20}$$

$$u = u_1 \qquad a_1 < r \leq r_1 \tag{4.21}$$

$$u = 0 \qquad r_1 < r \leq r_2 \tag{4.22}$$

It should be noted that the axial velocity profile ends at r_1, while the tangential velocity profile continues to r_2. Experimental results [3], [16] show that rotation occurs for $r > r_1$. This is caused by upstream transport of angular momentum due to the corner recirculation as shown in figure 1.1. The chosen profiles give a good approximation to the measured results and those obtained by Hallett and Toews [18], and are identical to those used by Hallett [19] to predict critical swirl. The values of λ and a_1 are inlet conditions and represent factors which are known to affect the swirling recirculation [18], [11] and [22].

The downstream profiles represent the state of the recirculating flow at the point of the maximum diameter and the recirculating mass flow rate. At this location radial velocities are negligible. Experimental data [37,15,26] suggest that axial velocities can be approximated by a parabola (this assumption also matches our experimental results.)

$$u = \Delta u \, (\frac{r}{r_2})^2 - u_{02}, \tag{4.23}$$

where

$$\Delta u = u_2 + u_{02}, \tag{4.24}$$

and u_{02} is the backflow velocity, such that

$$u_{02} > 0. \tag{4.25}$$

Experimental results in chapter 5 show that the tangential velocity near the wall becomes flatter than a potential vortex. The tangential velocity can therefore be approximated by

$$w = w_2 \frac{r}{a_2} \qquad 0 \leq r < a_2, \tag{4.26}$$

$$w = w_2 \qquad a_2 \leq r \leq r_2. \tag{4.27}$$

These profiles reduce to those of Hallett [19] for $u_{02} \rightarrow 0$ (critical swirl). For given inlet conditions and geometries, one needs to solve for the recirculating mass flow at station 2. In practice, this requires solving for the four velocity profile parameters w_2, a_2, u_2 and u_{02}. To do this, we may use integral equations for continuity of mass, momentum, and angular momentum, plus other conditions.

4.3.1 Continuity

At station 1, using the assumed inlet velocity profiles and integrating over r to r_1, we have [19] .

$$\dot{m}_1 = \pi \rho u_1 r_1^2 \, [1 - \frac{A_1}{3}(1 - \lambda) \,]. \tag{4.28}$$

where $A_1 = (a_1/r_1)^2$.

At station 2, the mass flow between the axis (0) and (r) is given by

$$\dot{m}(r) = 2\pi \int_0^r \rho u r \, dr = \pi \rho \, [\, \frac{1}{2} \Delta u (\frac{r^4}{r_2^2}) - u_{02} r^2 \,]. \tag{4.29}$$

The total mass flow rate can be obtained by integrating equation (4.29) from the axis (0) to (r_2)

$$\dot{m}_2 = \pi \rho r_2^2 \, [\frac{1}{2} \Delta u - u_{02}]. \tag{4.30}$$

Using conservation of the mass flow rate

$$\dot{m}_1 = \dot{m}_2, \tag{4.31}$$

we get

$$\Delta u = \frac{2u_1}{R_2} F_1 + 2u_{02}, \tag{4.32}$$

where $R_2 = (r_2/r_1)^2$ and

$$F_1 = 1 - \frac{1}{3}A_1\ (1 - \lambda). \tag{4.33}$$

Rewriting equation (4.32), we have

$$\frac{u_{02}}{\Delta u} = \frac{1}{2(u_1 F_1/(u_{02}R_2) + 1)}. \tag{4.34}$$

4.3.2 Recirculating Mass Flow

The recirculation zone geometry can be characterized either by the recirculation boundary r_b, defined as the radius at which the stream function Ψ equals zero, or the backflow boundary r_c, defined as the radius at which the axial velocity u equals zero. The recirculating mass flow rate is given by

$$\dot{m}(r_c) = -\pi\rho[\frac{1}{2}\Delta u(\frac{r_c^4}{r_2^2}) - u_{02}r_c^2]. \tag{4.35}$$

Using the definition of r_c, from equation (4.23) we have

$$(\frac{r_c}{r_2})^2 = \frac{u_{02}}{\Delta u} \qquad at \quad u = 0. \tag{4.36}$$

Therefore, equation (4.35) can be simplified to

$$\dot{m}_r = \pi\rho r_2^2\ (\frac{1}{2}\frac{u_{02}^2}{\Delta u}). \tag{4.37}$$

The fraction of mass flow rate recirculated is given by the ratio of m_r and m_2,

$$\frac{\dot{m}_r}{\dot{m}_2} = \frac{u_{02}^2}{\Delta u^2 - 2\Delta u u_{02}} = \frac{u_{02}^2}{u_2^2 - u_{02}^2}. \tag{4.38}$$

From the definition, we have the boundary streamline mass flow rate $\dot{m}(r_b)$=0, thus we can get

$$(\frac{r_b}{r_2})^2 = \frac{2u_{02}}{\Delta u} = 2(\frac{r_c}{r_2})^2. \tag{4.39}$$

Substituting equation (4.39) into the equation (4.23) at r_b, we have

$$u_{b2} = u_{02}. \tag{4.40}$$

4.3.3 Conservation of Angular Momentum

At station 1, the angular momentum is represented by

$$G_{\phi 1} = 2\pi \int_0^{r_2} \rho u w r^2 \, dr, \tag{4.41}$$

or

$$G_{\phi 1} = 2\pi\rho \, (\int_0^{a_1} u w r^2 \, dr + \int_{a_1}^{r_2} u w r^2 dr). \tag{4.42}$$

Substituting the distribution of the inlet velocities, we have

$$G_{\phi 1} = \pi \rho u_1 \Gamma_1 r_1^2 F_2, \tag{4.43}$$

where

$$F_2 = 1 + A_1(\frac{\lambda}{10} - \frac{3}{5}). \tag{4.44}$$

At station 2, using the distribution of the velocities, we get

$$\begin{aligned} G_{\phi 2} &= 2\pi\rho \, [\int_0^{a_2} (\Delta u \frac{r^4}{r_2^2} - u_{02} r^2)(w_2 \frac{r}{a_2}) dr + \int_{a_2}^{r_2} [\Delta u \frac{r_4}{r_2^2} - u_{02} r^2)(w_2) \, dr] \\ &= \pi \rho w_2 r_2^3 \, [\Delta u (\frac{2}{5} - \frac{1}{15} A_2^{5/2}) - u_{02} \, (\frac{2}{3} - \frac{1}{6} A_2^{3/2}) \,]. \end{aligned} \tag{4.45}$$

where $A_2 = (a_2/r_2)^2$.

Substituting Δu from Equation (4.34), we obtain

$$G_{\phi 2} = \pi \rho w_2 r_2^3 \, [u_1 \frac{2F_1 F_3}{R_2} + u_{02}(2F_3 - F_4) \,], \tag{4.46}$$

where

$$F_3 = (\frac{2}{5} - \frac{1}{15} A_2^{2/5}), \tag{4.47}$$

$$F_4 = (\frac{2}{3} - \frac{1}{6} A_2^{3/2}). \tag{4.48}$$

Rearranging equation (4.46), we have

$$G_{\phi 2} = \pi \rho u_1 r_1^2 (w_2 r_2) \, [2F_1 F_3 + \frac{u_{02}}{u_1} R_2 (2F_3 - F_4) \,]. \tag{4.49}$$

If the wall friction is negligible, $G_{\phi 1} = G_{\phi 2}$, thus we have

$$w_2 r_2 = \frac{\Gamma_1 F_2}{2F_1F_3 + (u_{02}/u_1)R_2(2F_3 - F_4)}. \tag{4.50}$$

Inverting equation (4.50), we get

$$\frac{u_{02}}{u_1} = \frac{1}{R_2(2F_3 - F_4)}[\frac{\Gamma_1 F_2}{w_2 r_2} - 2F_1F_3]. \tag{4.51}$$

4.3.4 Conservation of Axial Momentum

From the conservation of axial momentum, we have the relationship

$$G_{x1} + P_1 = G_{x2} + P_2. \tag{4.52}$$

where P is the pressure force. The definition of the pressure force is

$$P_1 = 2\pi \int_0^{r_2} pr\, dr, \tag{4.53}$$

where from equation (4.12),

$$p(r) = p_{01} + \int_0^r \frac{\rho w^2}{r}\, dr. \tag{4.54}$$

The axial momentum flux at station 1 is

$$\begin{aligned} G_{x1} &= 2\pi \int_0^{r_1} \rho u^2 r\, dr \\ &= 2\pi \int_0^{a_1} \rho[u_1^2(\lambda - (\lambda - 1)\frac{r}{a_1})^2]r\, dr + 2\pi \int_{a_1}^{r_1} \rho u_1^2 r\, dr. \end{aligned} \tag{4.55}$$

Simplifying , we get

$$G_{x1} = \pi \rho u_1^2 r_1^2[1 - A_1(\frac{1}{2} - \frac{\lambda}{3} - \frac{\lambda^2}{6})\,]. \tag{4.56}$$

By employing the w-profile at station 1, P_1 is given by

$$\begin{aligned} P_1 &= 2\pi \int_0^{r_2} (p_{01} + \int_0^r \frac{\rho w^2}{r}\, dr)r\, dr \\ &= 2\pi \int_0^{a_1} [p_{01} + \int_0^r \frac{\rho}{r}(\frac{\Gamma_1 r}{a_1^2})^2\, dr]r\, dr + 2\pi \int_{a_1}^{r_2} [p_{01} + \int_{a_1}^r \frac{\rho}{r}(\frac{\Gamma_1}{r})^2\, dr\,]r\, dr. \end{aligned} \tag{4.57}$$

Simplifying, we have

$$P_1 = \pi\ [p_{01} r_1^2 R_2 + \rho \Gamma_1^2\ (\frac{R_2}{A_1} - \frac{3}{4} - \frac{1}{2} \ln \frac{R_2}{A_1})\ ]. \tag{4.58}$$

By the same approach, we can obtain the axial momentum flux at station 2

$$\begin{aligned} G_{x2} &= 2\pi \int_0^{r_2} \rho[\Delta u^2 (\frac{r}{r_2})^4 - 2u_{02}\Delta u (\frac{r}{r_2})^2 + u_{02}^2] r\, dr \qquad (4.59) \\ &= \pi \rho r_2^2\ (\frac{1}{3}\Delta u^2 - u_{02}\Delta u + u_{02}^2) \\ &= \pi \rho u_1^2 r_1^2\ [\frac{4}{3}\frac{F_1^2}{R_2} + \frac{2}{3}\frac{u_{02}}{u_1} F_1 + \frac{R_2}{3}(\frac{u_{02}}{u_1})^2\ ], \end{aligned}$$

and the pressure force

$$P_2 = \pi\ [p_{02} r_1^2 R_2 + \rho (w_2 r_2)^2 (\frac{1}{4} A_2 - \frac{1}{2} \ln A_2)\ ]. \tag{4.60}$$

4.3.5 Bernoulli Equation along Axis

In the previous analysis we have used up all three conservation equations and we ended up with four unknown parameters, namely w_2, u_{02}, Δu and a_2. In addition, we have introduced the pressure difference (p_{01} - p_{02}) through equations (4.58) and (4.60). In order to solve this problem, another relation among these parameters needs to be set up. We examine two streamlines, one going from the axis at station 1 to the stagnation point of the recirculation zone at s; the other starting at station 2 in the backflow and going back to s as shown in figure (4.2). The Bernoulli equation along 1 to s is

$$p_{01} + \frac{1}{2}\rho (\lambda u_1)^2 = p_s; \tag{4.61}$$

and a energy equation along 2 to s is

$$p_{02} + \frac{1}{2}\rho u_{02}^2 = p_s + Losses. \tag{4.62}$$

Although the streamline from 1 to s may be approximated as frictionless, the streamline from 2 to s is associated with large losses. This is caused by the backflow

and turbulence generation inside the recirculation zone. The losses can be thought of as a function of u_{02} and expressed as

$$Losses = \frac{1}{2} k \rho u_{02}^2. \tag{4.63}$$

where k is a loss coefficient.

Substituting equation (4.63) into (4.62), we then obtain

$$p_{02} = p_{01} - \frac{1}{2}\,\rho(1-k)u_{02}^2 + \frac{1}{2}\rho\,(\lambda u_1)^2. \tag{4.64}$$

The larger k is, the higher is the value of p_{02} that will be needed to drive the recirculation against the losses. Inserting equation (4.64) into equation (4.58) and (4.60), then solving equation (4.52), we eliminate p_{01} and p_{02} and get

$$\begin{aligned}(\frac{w_2 r_2}{u_1 r_1})^2 \;=\; & \frac{1}{F_6}\,\{(\frac{\Gamma_1}{u_1 r_1})^2\,[\,\frac{R_2}{A_1} - \frac{3}{4} - \frac{1}{2}\ln(\frac{R_2}{A_1})\,] \\ & + 1 - A_1(\frac{1}{2} - \frac{\lambda}{3} - \frac{\lambda^2}{6}) - \frac{1}{2}\lambda^2 R_2 - \frac{4F_1^2}{3R_2} \\ & - \frac{2u_{02}}{3u_1}F_1 + R_2(\frac{u_{02}}{u_1})^2\,[\,\frac{(1-k)}{2} - \frac{1}{3}\,]\,\},\end{aligned} \tag{4.65}$$

where

$$F_6 = \frac{1}{4}A_2 - \frac{1}{2}\ln A_2. \tag{4.66}$$

If k is known, we can solve equation (4.50) and (4.65) for the values of w_2 and u_{02}.

4.3.6 Model for the Loss Coefficient k

To find an expression for k, we write the x-direction Navier-Stokes equation along the axis from 2 to s

$$\frac{\partial}{\partial x}(\frac{1}{2}\rho u^2 + p) = \frac{1}{r}\frac{\partial}{\partial r}(r\tau_{xr}). \tag{4.67}$$

In the equation, since $v = 0$ on the axis, the term $v\partial u/\partial r$ has been dropped. Also τ_{xx} has been neglected. Then we define that

$$\tau_{xr} = \rho\varepsilon\frac{\partial u}{\partial r}, \tag{4.68}$$

where ε is the effective turbulent viscosity. Now we have

$$\frac{\partial}{\partial x}(\frac{1}{2}\rho u^2 + p) = \rho\varepsilon(\frac{\partial^2 u}{\partial r^2} + \frac{1}{r}\frac{\partial u}{\partial r}) \qquad at\ r = 0. \tag{4.69}$$

Substituting the assumed velocity profiles,

$$\frac{\partial u}{\partial r} = 2\Delta u\frac{r}{r_2^2}, \tag{4.70}$$

$$\frac{\partial^2 u}{\partial r^2} = \frac{2\Delta u}{r_2^2}, \tag{4.71}$$

the equation (4.69) becomes

$$\frac{\partial}{\partial x}(\frac{1}{2}\rho u^2 + p) = \frac{4\rho\varepsilon\Delta u}{r_2^2} \qquad at\ r = 0. \tag{4.72}$$

Integrating equation (4.72) from 2 to s, we get

$$\frac{1}{2}\rho u_{02}^2 + p_{02} - p_s = \frac{4\rho\varepsilon\Delta u L1}{r_2^2}, \tag{4.73}$$

where

$$L1 = x_2 - x_s. \tag{4.74}$$

Referring to equation (4.62), we have

$$k = \frac{8\varepsilon\Delta u L1}{r_2^2 u_{02}^2}. \tag{4.75}$$

The value of ε can be obtained by using the simple turbulent exchange assumption of Schlichting [35] for a turbulent wake or jet:

$$\varepsilon = \kappa r_b(u_{b2} + u_{02}) \tag{4.76}$$

where κ is a shear coefficient. Since for the chosen profile, we have

$$u_{b2} = u_{02},$$

$$\varepsilon = 2\kappa r_b u_{02}. \tag{4.77}$$

Substituting into equation (4.75), we then obtain

$$k = 16\kappa\,(\frac{\Delta u}{u_{02}})(\frac{r_b}{r_2})(\frac{L1}{r_2}). \tag{4.78}$$

It is more convenient to relate $L1$ to r_b in practice, so equation (4.78) is changed to

$$k = 16\kappa(\frac{\Delta u}{u_{02}})(\frac{L1}{r_b})(\frac{r_b}{r_2})^2. \tag{4.79}$$

From equation (4.39) for r_b, finally, we get k as

$$k = 32\kappa\frac{L1}{r_b}. \tag{4.80}$$

Note that in integrating equation (4.67), it has been assumed that τ_{xr} and hence ε, u_{02} and Δu do not vary with x. This is, of course, untrue. Due to this assumption the Δu and u_{02} used for calculating τ are effective average values over the distance from 2 to S. The difference between these averages and the real u_{02} and Δu must be absorbed by κ. The program made to calculate the recirculating parameters is shown in Appendix B.

In some case at high swirl in the present experiments, the inlet velocity profiles were found to have a small region of flow reversal on the axis; ie, λ took on a small negative value. In this case the stagnation point s no longer exits. It can be shown, however, that equation (4.64), (4.65) and (4.75) are equally valid for this case.

Although the exchange model of equation (4.76) is considered initially valid for free turbulence jets, wakes etc., it should work well in this model because the recirculation is not bounded by a wall. Schlichting [35] suggested that the value of κ be 0.0256 for a circular free jet and 0.094 for a plane wake. Values of κ required to fit the present results are much large of order of 1. This is to be expected, since the turbulence intensity of a swirling recirculating flow is much higher than that of a simple wake.

Some comments are also given here about the model: when we derived the three integral equations, we assume that flow is inviscid. But we do consider the viscous flow by deriving the expression for k. Both of them are consistent. Because we integrated three simplified Navier-Stokes equations across test section, only wall shear stress is involved in the integrations, and only it is neglected. Internal shear stresses can still exist, and when we derive the expression for k along the axis, the

turbulent shear stress has to be considered in this region. Because the shear stress is higher at the axis, this was proved by Hallett and Güenther in [16].

4.4 Fitting of Model Parameters to Measured Inlet Velocities

To compare the model with experimental data, the parameters of the inlet velocity profiles, i.e., u_1, a_1, λ, and Γ_1 , must first be fitted so that the centerline velocity, the mass flow and the angular momentum flux of the measured profile can be reproduced.

First a correction for the wall boundary layer is applied as in Fig.(4.3). The measured profile extends to the wall and it is assumed in the integration used to find $\dot{m}$ in data reduction program that u drops linearly from the last measured point r_N to the wall at r_1. The model profile used has no boundary layer, but continues at constant velocity to the wall. In order to conserve mass flow, therefore, the wall in the model must be located at a radius r_B, where $(r_1 - r_B)$ is the displacement thickness of the boundary layer as shown in figure (4.3). To calculate and evaluate the mass flow in the boundary layer $\dot{m}_{BL}$, we have

- from measurement, using the trapezoid rule:

$$\dot{m}_{BL} = 2\pi \int_{r_N}^{r_1} \rho u r \, dr \tag{4.81}$$

$$= \pi \rho u_N r_N (r_1 - r_N), \tag{4.82}$$

- from model:

$$\dot{m}_{BL,M} = \pi \rho u_N (r_B^2 - r_N^2). \tag{4.83}$$

Then equating both equations, we obtain

$$r_B^2 = r_N^2 + r_N(r_1 - r_N). \tag{4.84}$$

Because of the smaller cross-section produced by this correction, the average velocity $\bar{u}_M$ for the model is now greater than the measured value $\bar{u}_{ref}$. They are related by

$$\bar{u}_M = \bar{u}_{ref}(\frac{r_1}{r_B})^2. \tag{4.85}$$

For all model profiles, $\bar{u}_M$ will be the reference velocity.

The angular momentum flux must also be corrected. The measured G_ϕ between r_N and r_1, $G_{\phi BL}$, is

$$\begin{aligned} G_{\phi BL} &= 2\pi \int_{r_N}^{r_1} \rho u w r^2 \, dr \\ &= \pi \rho_N u_N w_N r_N^2 (r_1 - r_N). \end{aligned} \tag{4.86}$$

Since the model assumes $w = w_N r_N / r$, integrating G_ϕ from r_N to r_B yields the angular momentum flux in the boundary layer $G_{\phi BL,M}$,

$$G_{\phi BL,M} = \pi \rho_N u_N w_N r_N \, (r_B^2 - r_N^2). \tag{4.87}$$

From that we get the ratio of $G_{\phi BL,M}/G_{\phi BL}$

$$\frac{G_{\phi BL,M}}{G_{\phi BL}} = \frac{r_B^2 - r_N^2}{r_N(r_1 - r_N)}. \tag{4.88}$$

Now we need to derive the total angular momentum $G_{\phi M}$ for the model profile. It can be found if we know the angular momentum stream function Ψ_ϕ at r_B

$$G_{\phi M} = \Psi_{\phi,B} G_\phi, \tag{4.89}$$

where G_ϕ is the total angular momentum from measurements. Since by definition $\Psi_{\phi,wall} = 1.0$, we have the following relationship between the $G_{\phi BL,M}$ for the model and the measured $G_{\phi BL}$

$$\frac{G_{\phi BL,M}}{G_{\phi BL}} = \frac{\Psi_{\phi,B} - \Psi_{\phi N}}{1 - \Psi_{\phi N}}. \tag{4.90}$$

Rearranging equation (4.90), we have

$$\Psi_{\phi,B} = \Psi_{\phi,N} + \frac{G_{\phi BL,M}}{G_{\phi BL}}(1 - \Psi_{\phi N}), \tag{4.91}$$

or

$$\Psi_{\phi,B} = \Psi_{\phi,N} + \frac{r_B^2 - r_N^2}{r_N(r_1 - r_N)}(1 - \Psi_{\phi N}). \tag{4.92}$$

where $\Psi_{\phi,N}$ comes from measurements. The dimensionless total angular momentum flux Ω_M for fitting profiles is then

$$\Omega_M = \frac{G_{\phi M}}{r_B \dot{m} \bar{u}_M} \tag{4.93}$$

$$= \frac{\Psi_{\phi,B} G_\phi}{r_1 \dot{m} \bar{u}_{ref}} (\frac{r_B}{r_1})^2 (\frac{r_1}{r_B}). \tag{4.94}$$

This connected value of Ω must now be related to the model velocity profile shapes in order to solve for the profile parameters. Recalling the model profile in section (4.3) and considering the boundary layer defined in this section, the angular momentum flux can be obtained from the integration

$$G_{\phi M} = 2\pi \int_0^{r_B} \rho u w r^2 dr, \tag{4.95}$$

so that

$$G_{\phi M} = \pi \rho u_1 \Gamma_1 r_B^2 [1 + A_1(\frac{\lambda}{10} - \frac{3}{5})]. \tag{4.96}$$

The mass flow rate in equation (4.28) can be obtained by using r_B to replace r_1 in equation (4.94)

$$\dot{m} = \pi \rho u_1 r_B^2 [1 - \frac{A_1}{3}(1 - \lambda)]. \tag{4.97}$$

Substituting equations (4.96) and (4.97) to equation (4.94), the dimensionless angular momentum flux becomes

$$\Omega_M = \frac{\Gamma_1}{r_B \bar{u}_M} \frac{[1 + A_1(\lambda/10 - 3/5)]}{[1 - A_1/3(1 - \lambda)]}. \tag{4.98}$$

To begin fitting, the angular velocity $\omega/\bar{u}_{ref} = (w/\bar{u}_{ref})/r$ of the solid body core region is read from the measured profile to be fitted, which from above angular velocity expression allows Γ_1 to be expressed as

$$\frac{\Gamma_1}{\bar{u}_{ref}} = \frac{r_B^2 A_1 \omega}{\bar{u}_{ref}}. \tag{4.99}$$

Then equation (4.98) can be written as

$$\Im_M = \frac{\bar{u}_{ref}\Omega_M}{\omega r_B} = A_1 \frac{[\ 1 + A_1(\lambda/10 - 3/5)\ ]}{[\ 1 - A_1/3.(1-\lambda)\ ]} \tag{4.100}$$

Since $\Im_M$ is known, this gives one equation for λ and A_1. The second one is derived by reading the axial velocity at the centerline ($v/\bar{u}_{ref}$) from the measurements; this is then converted to a $\bar{u}_M$ basis:

$$\frac{v}{\bar{u}_M} = \frac{\lambda u_1}{\bar{u}_M} = \frac{v}{\bar{u}_{ref}}(\frac{r_B}{r_1})^2 \tag{4.101}$$

From the continuity equation, we have

$$\frac{\bar{u}_M}{u_1} = 1 - \frac{1}{3}A_1(1-\lambda), \tag{4.102}$$

so that we can obtain λ as

$$\lambda = \frac{1 - A_1/3}{\bar{u}_M/v - A_1/3}. \tag{4.103}$$

Substituting equation (4.103) into equation (4.100) and simplifying it, we finally obtain the following cubic equation for A_1

$$A_1^3 + A_1^2(-\frac{7}{5} - \frac{18}{5}\frac{\bar{u}_M}{v}) + A_1\frac{\bar{u}_M}{v}(6 + 2\Im_M) - 6\frac{\bar{u}_M}{v}\Im_M = 0. \tag{4.104}$$

This can be used to solve for A_1, then λ from equation (4.103), and $\Gamma_1\ /r_B\bar{u}_M$ from equation (4.98).

Summarizing, to fit model parameters to measured inlet velocity profiles, the following procedures are performed:

1. Read $v/\bar{u}_{ref}$, $w_s/\bar{u}_{ref}$, r_s from measured profile; where w_s is the value chosen from experimental results in the solid body region ($0 \leq r \leq a_1$).

2. Convert to $\bar{u}_M$ basis:

$$\frac{v}{\bar{u}_M} = \frac{v}{\bar{u}_{ref}}(\frac{r_B}{r_1})^2 \tag{4.105}$$

$$\frac{\omega r_B}{\bar{u}_M} = \frac{w_s r_B}{\bar{u}_{ref} r_s}(\frac{r_B}{r_1})^2 \tag{4.106}$$

3. Calculate $\Im_m$ and find A_1 from equation (4.104);

4. Find λ from equation (4.103), $\Gamma_1 / r_B \bar{u}_M$ from equation (4.98);

5. Find $u_1/\bar{u}_M$ from (4.102);

To plot fitted profiles, they must be returned to a $\bar{u}_{ref}$ basis by

$$\frac{u_1}{\bar{u}_{ref}} = \frac{u_1}{\bar{u}_M}(\frac{r_1}{r_B})^2, \tag{4.107}$$

$$\frac{w}{\bar{u}_{ref}} = \frac{w}{\bar{u}_M}(\frac{r_1}{r_B})^2. \tag{4.108}$$

The value of (w_s, r_s) was determined by selecting it to minimize the sum of least squares of deviations from measured points

$$\sum(\frac{u}{\bar{u}_{ref}} - \frac{u_M}{\bar{u}_{ref}})^2 + \sum(\frac{w}{\bar{u}_{ref}} - \frac{w_M}{\bar{u}_{ref}})^2 = min. \tag{4.109}$$

where u_M, w_M are measured values.

A BASIC program was developed by Hallett to solve these equations with input values from the measurements Ω_M, v and ω. The program is listed in Appendix C.

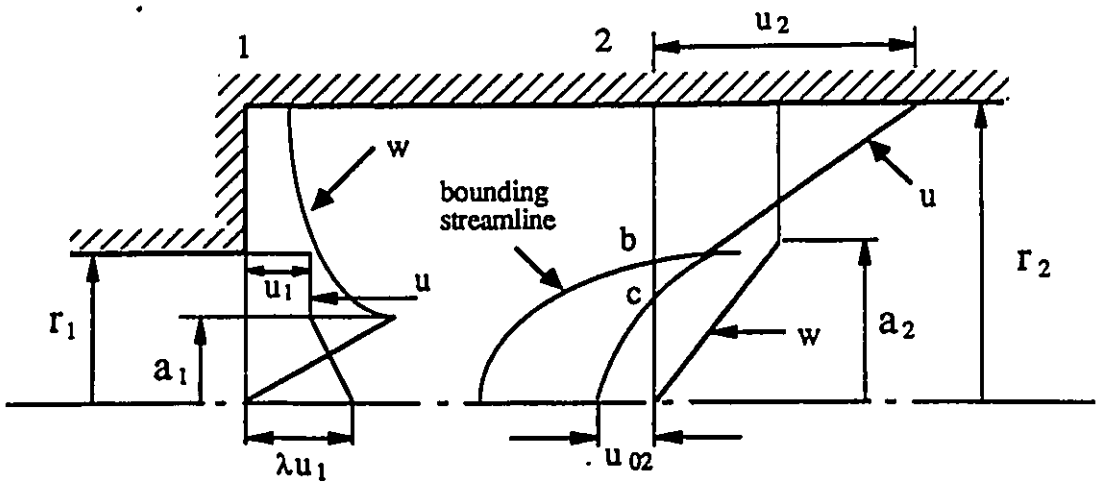

Figure 4.1: Assumed Velocity Profiles

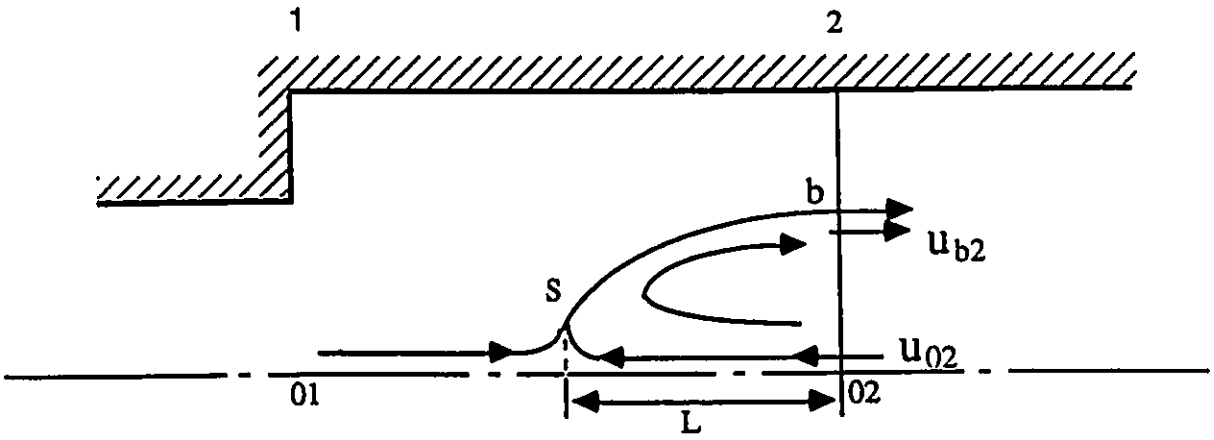

Figure 4.2: Stagnation of Flow Along Axis

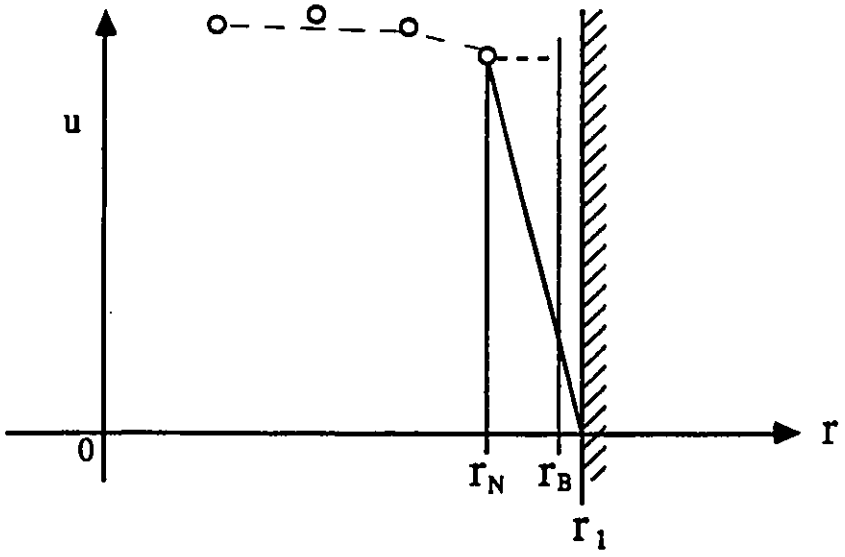

Figure 4.3: Correction for Boundary Layer

Chapter 5

Results and Discussion

In this chapter, we present our experimental results and discuss the effects of the expansion ratio and the swirl intensity on velocity components, recirculating mass flow rate and size of the recirculation zone. The numerical results obtained from the fitted parameters of the inlet velocity profiles are presented here and compared against the experimental results.

5.1 Experimental Results

To study the behavior of swirling flow issuing into a sudden expansion, the five-hole probe was used to measure the velocity components in expansion ratios of 2.813, 2.0 and 1.625. Based on those velocity components, recirculating mass flow rates, swirl intensities and the size of the recirculation zone were calculated to indicate the structure of the central recirculation zone in enclosed swirling flow. In the following sections, the experimental results of velocity components, recirculating mass flow rates and the size of the recirculation zone are presented and the effects of both the swirl intensity and expansion ratio are also discussed.

5.1.1 Velocity Components

The distributions of axial velocity profiles are shown in figures (5.1) to (5.11). There are three coordinates in each graph, namely axial and radial distance and the velocity scale. The velocities have been made dimensionless with the average axial velocity $\bar{u}_{ref}$ in the inlet. The velocity profiles start from the inlet, located just downstream of the step. The solid lines present a number of stations downstream of the expansion. Backflow velocities are those with negative values which are formed by axial pressure gradients. As this pressure gradient increased, the flows are stagnated at axis and backflow expands gradually to maximum size; then gradually reduces and the backflow zone disappears due to turbulence. The axial velocity component and the tangential velocity component are illustrated separately for clarity. Velocity profiles of different inlet swirl intensities and expansion ratios are presented in different figures. The shapes of the velocity profiles are similar to those obtained by Hallett and Toews [18], Hallett and Tavasoli [20], Gouldin [15], and Mahmud et al. [26] and Mathur and Maccallum [27], and Beltagui and Maccallum [3].

For axial velocities, there are small back flow velocities observed at the higher swirl settings at the inlet, for example in figures (5.1), (5.4), and (5.5) which correspond to $\Omega = 1.038$ at $r_2/r_1 = 2.813$, and $\Omega = 1.437$ and $\Omega = 1.129$ at $r_2/r_1 = 2.0$. By changing the swirl generator setting from pure tangential flow to axial plus tangential, or varying the sliding sleeve position, we can change the swirl intensity for a fixed expansion ratio. An increase in swirl intensity results in larger backflow velocities, as for example, in figures (5.3) to (5.1). The impact of the expansion ratio on the back flow velocities is studied in figures (5.1) to (5.11). The backflow velocities decrease slightly with increasing expansion ratio at roughly constant swirl especially for the expansion ratios of 2.813 and 2.0. Corner recirculation zones were found close to the inlet, as shown in figures (5.1) to (5.5) and (5.7). These are simply flow separations caused by the step of the expansion; they are not within the scope of this research. Note that in some velocity profiles, there are several points

missing, for example in figure (5.1); this is because some values from experiments are out of the calibrated range at yaw angles of the probe. This occurs mostly when the radial velocity is significant and the axial velocity is very small.

The tangential velocities are presented in figures (5.12) to (5.22). The same scales are used for the velocity profiles as before. For a fixed test section size and inlet condition, each downstream station is exactly matched with the axial velocity profiles. By examining the tangential velocities, a solid body core region can be identified, within which the tangential velocity increases approximately linearly with r/r_1. The radius of this core is seen in all cases to be nearly equal to that of inlet flow and insensitive to the expansion ratio as observed by Hallett and Günther [16] and Mathur and Maccallum [27]. In general, the tangential velocity increases with swirl intensity, but this does not appear to affect the core size significantly. Outside the core, the tangential velocity is nearly constant, except near the inlet; in no case can a potential vortex outer region be seen, except in the inlet flow. This and the fact that the core radius does not expand as the flow expands is due to recirculation of angular momentum by the backflow.

The radial velocities were found generally to be very small comparing to the axial and tangential velocities and are not shown here.

5.1.2 Recirculation Zone

By referring back to figures (5.1) to (5.11), the dashed line represents the boundary of the backflow zone, which was obtained by connecting the zero velocity (u=0) points. The crossed line represents the boundary of the recirculation zone, which was obtained by connecting the zero mass stream function ($\Psi = 0$) points. Within the recirculation boundary the flow can be regarded as recirculating in a closed toroidal vortex. We can see that for fixed test section geometry and inlet conditions, the diameter of the recirculation zone increases with the local distance and reaches a maximum at a certain point, then decreases and finally disappears, as for example in

figures (5.1) and (5.2). The location of the maximum diameter of the recirculation zone corresponds to the largest diameter of the backflow zone, as for example in figure (5.4). The length of the recirculation zone increases with swirl intensity for a given test section, but the diameter of the recirculation zone does not change greatly. This is similar to observations by Rao et al. [30], Mathur and Maccallum [27] and Beltagui and Maccallum [3]. The recirculation zone diameter iricreases roughly in proportion to the expansion size. The upstream sections of recirculation zone measured under different conditions appear to be geometrically similar, so that the axial distance from the start of recirculation (the inlet) to the point of maximum diameter is roughly in constant ratio to the recirculation diameter.

5.1.3 Mass Error

The average mass flow error was obtained by comparing the metered mass flow rate with the one obtained from the integration. The mass flow error fraction against local distances for different inlet conditions and different sizes of the test sections were plotted in figures (5.23) to (5.33). By investigating these figures, one can roughly divide three regions of mass error, namely the inlet, the region with a corner recirculation zone just downstream of the inlet, and the remainder of the flow. In the experiment, the average error percentage was approximately for these regions: 10% for inlet, 34% for corner recirculation region and 8.0% for the central recirculation region. Since the existence of a corner recirculation zone affects the error in the total mass flow rate, the error fraction in this region was much higher. For the expansion ratio of 1.625, at swirls of $\Omega = 0.58$ and $\Omega = 0.511$, the highest mass error fraction was found. The reasons for this are unclear, but perhaps probe blockage had some effect here. On the other hand, it is assumed that the flow is axi-symmetric, but the experiments show that the flow is not completely axi-symmetric near the axis.

5.1.4 Dimensionless Angular Momentum Flux vs. Local Distance

The dimensionless angular momentum flux distributions against local distances for different inlet conditions and different sizes of test sections were plotted in figures (5.34) to (5.44). The results of the experiments show that for most cases, the dimensionless angular momentum flux is approximately constant with small fluctuations. From the integrated equations of motion, the values of Ω should only be affected by wall friction, which should cause Ω to drop slowly with distance. Taking into account the errors in the experiment, this gives a very good agreement. This indicates that the experimental results are reliable for the most part. Only, for the expansion ratio of $r_2/r_1 = 2.813$ does the dimensionless angular momentum flux show larger variations, especially at $\Omega = 1.038$ and $\Omega = 0.639$. This is due in part to the large corner recirculation zones for these cases, which cause larger mass errors in the measurements, and to the lower velocities in the large expansion test section.

5.1.5 Recirculating Mass Flow Rate vs. Local Distance

Recirculating mass flow rates were obtained by integrating the backflow velocities over the radius of the backflow zone. They are shown in figures (5.45) to (5.55). It is to be expected that the higher the swirl is, the bigger the recirculating mass flow rate is. Most of the experimental results fit this quite well. However, in some cases, the results do not follow that: for example, in the case of the expansion ratio $r_2/r_1 = 1.625$, the local recirculating mass flow rate for $\Omega = 0.511$ was smaller than for $\Omega = 0.485$. This is caused by the low tangential velocity. Further investigating the graphs, we found that we may not always get the largest $\dot{m}_r/\dot{m}$ at the largest diameter of the recirculation zone. The possible reason for that might be again the corner recirculation zones near the inlets which bring more mass flow errors. A few points which lie away from the others are seen to be obviously incorrect: for example, at $r_2/r_1 = 2.813$ and $\Omega = 0.506$ there is a point at $X = 18$ in figure (5.47)

which corresponds to an Ω in figure (5.36) which is too large, while the point at $X = 7$ for $r_2/r_1 = 2.0$, $\Omega = 0.676$ in figure (5.50) is associated with a large mass error in figure (5.28).

5.2 Numerical Results

In order to predict the structure of the central recirculation zone in enclosed swirling flow, a simple mathematical model has been set up. To evaluate this model, in this section we compare the numerical results with the experimental results in terms of several important parameters of the recirculating flow, such as the recirculating mass flow rate and the radius of the recirculation zone. Discussions are also given based on the comparisons.

5.2.1 The Fitted Inlet Velocity Profiles

To compare the model with experimental data, the parameters of the inlet velocity profiles, i.e. u_1, a_1, λ and Γ_1, must first be fitted so that the centerline velocity, the mass flow and the angular momentum flux of the measured velocity profiles are reproduced. These parameters can be solved for as described in section 4.4. The fitted inlet velocity profiles are shown in figures (5.56) to (5.66). In the figures, the solid lines are fitted lines and the points are the measured velocity profiles. We can see that in most cases they are fitted reasonaly well. The fitted inlet velocity parameters are shown in table 1.

5.2.2 Numerical Examples and Comparisons

Recall the model derived in chapter 4. In order to obtain values for parameters a_2/r_2 and L/r_b, it is necessary to make physically reasonable assumptions. From the experimental results, we found that the tangential velocity profiles have a solid body core diameter roughly equal to that of inlet flow and that measured tangential

velocities are similar to the assumed profile shape, for example $w = w_2 r/a_2$ for $0 \leq r < a_2$ and $w = w_2$ for $a_2 \leq r \leq r_2$ (section 4.3). Also, as in early work [19], the model proved to be insensitive to the value of a_2. Therefore, a_2 is chosen to be equal to a_1 for the corresponding inlet condition. The parameter L/r_b is also chosen based on the results of experiments. From the discussion of the previous section, L/r_b can be approximately chosen to be 1.5.

Based on the mathematical model and the fitted parameters of the inlet flow, we can solve for all the values of the recirculation zone such as the recirculating mass flow rate, the backflow velocities and the radius of recirculation zone. Table 5.2 shows comparisons between the numerical and the experimental results for a constant value of $\kappa = 1.0$. This value gives us a good approximation of measured results.

By comparing the recirculating mass flow rates from the model to those from experiment, an average error of 22% was found, except in three cases, namely, $\Omega = 1.038$ and at $r_2/r_1 = 2.813$, $\Omega = 0.676$ and $\Omega = 0.452$ at $r_2/r_1 = 2.0$. The difference can be partially explained by comparing model with measured velocity profiles. The parabolic profile assumption in the model caused the axial velocity to increase with radius and reach a maximum at the outside wall. By analyzing the axial velocity profiles from experiment, the approximated parabolic shape of the axial velocity distributions was found at the maximum diameter of the recirculation zone for expansion ratios of 2.813 and 2.0, although the value of the axial velocity does not increase enough near the outside wall and because of the wall boundary layer. This agrees with those observed in [19] and [30]. However, the parabolic shape did not fit quite as well for the expansion ratio of 1.625. This is simply because there is not enough space to expand the flow at this test section. On the other hand, due to the boundary layer, the velocity will actually be reduced near the wall, which may cause a change in the recirculating mass flow rate.

Error in the experiment is a further possible cause of difference between the model and the experiment. The recirculating mass flow rate is reported as the ratio

between the back flow mass obtained by integrating axial velocity over backflow zone and the total mass obtained by integrating axial velocity over the entire section, and it is expected that the mass flow error should at least partly cancel out in the final dimensionless quantity. Due to the integration, the error caused by assumptions is reduced and this should result in a smaller error fraction for the recirculating mass flow rate. For the $\Omega = 1.038$ at $r_2/r_1 = 2.813$, and $\Omega = 0.676$,$\Omega = 0.452$ at $r_2/r_1 = 2.0$, the mass error fractions are larger than usual and it seems probable that there are corner recirculation zones and the experimental value of $\dot{m}_r/\dot{m}$ is too large for $\Omega = 0.452$. In figures (5.34), the large variation of angular momentum flux was obtained close to the inlet. Taking into account of above reasons, this is why the large differences were obtained for these three cases.

On the other hand, from the table we can see that there is a difference which is about 26% in average in back flow velocities between the results from the model and the experiments. To explain this, we examine the velocity profile assumption again. In the model, we used a Rankine vortex to describe the inlet velocity profiles. This assumption reflects the velocity distribution reasonably correctly for most cases. Another important assumption made in the model is the parabolic distribution for the axial velocity profile at the maximum diameter of the recirculation zone as discussed before. This is considered another source of error. More important, the model backflow velocity reaches a maximum value at the axis of the test section, while results of experiments show that the backflow velocity does not always reach a maximum value on the axis. However, from a definition of u_{02}/u_{ref}, u_{02} is supposed to be the largest velocity on the axis. This can cause a difference between the model and the experiment. This is also because of the complexity of the flow and the simplicity of the model. Of course, the error associated with the experiment is a another factor in any difference. The difference in the radius of backflow zone r_c/r_2 between the model and the experiment can also be accounted by above reasons. It has a 15% average error percentage.

Agreement between the model and experimental results will be better, if κ is

chosen with different values for different expansion ratios. For a better fit, κ should increase with r_2/r_1, reflecting the fact that a larger recirculation zone produces more turbulence. However, the relationship between κ and r_2/r_1 remains to be explored.

In this chapter, we discussed the results and comparisons between the model and experiment. Although the experiments have an average amount of error as shown in section (5.1.3), by considering a complex of the flow, the experiments are reliable. The major concern for this model is the recirculating mass flow rate. Although there are difference in the model and the experiment, this agreement is satisfactory.

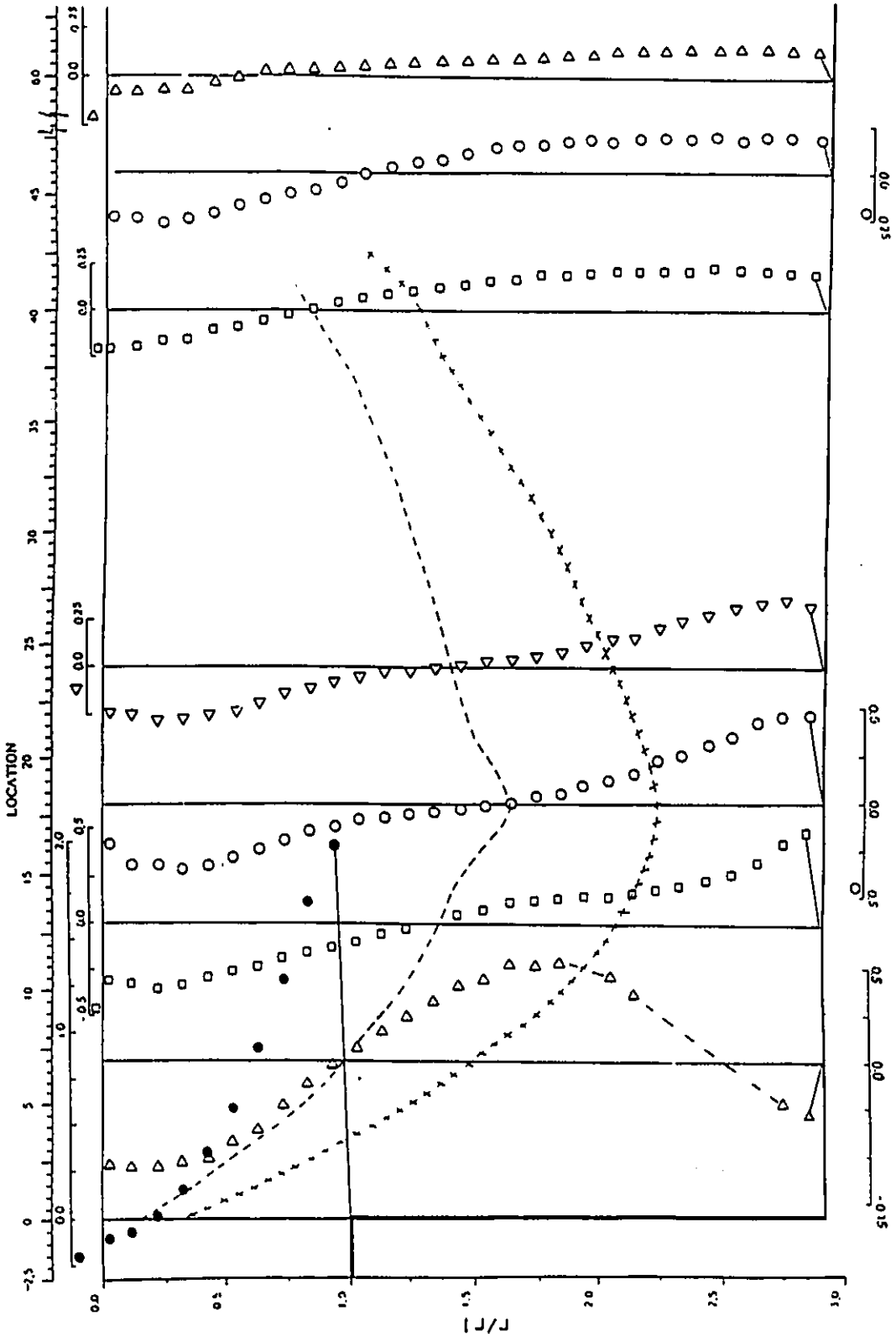

Figure 5.1: Axial Velocity Profiles for $r_2/r_1 = 2.813$, $\Omega = 1.038$

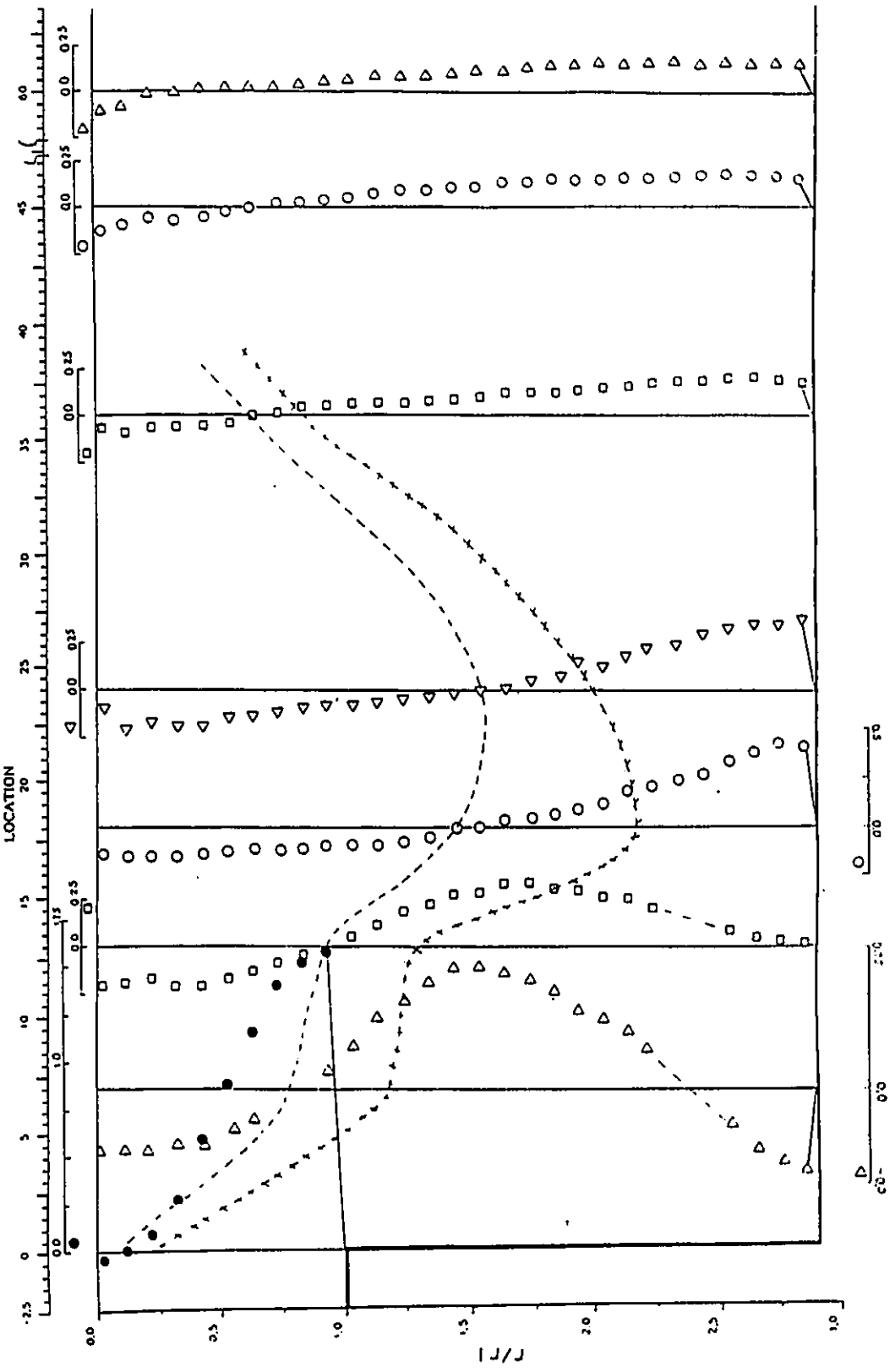

Figure 5.2: Axial Velocity Profiles for $r_2/r_1 = 2.813$, $\Omega = 0.639$

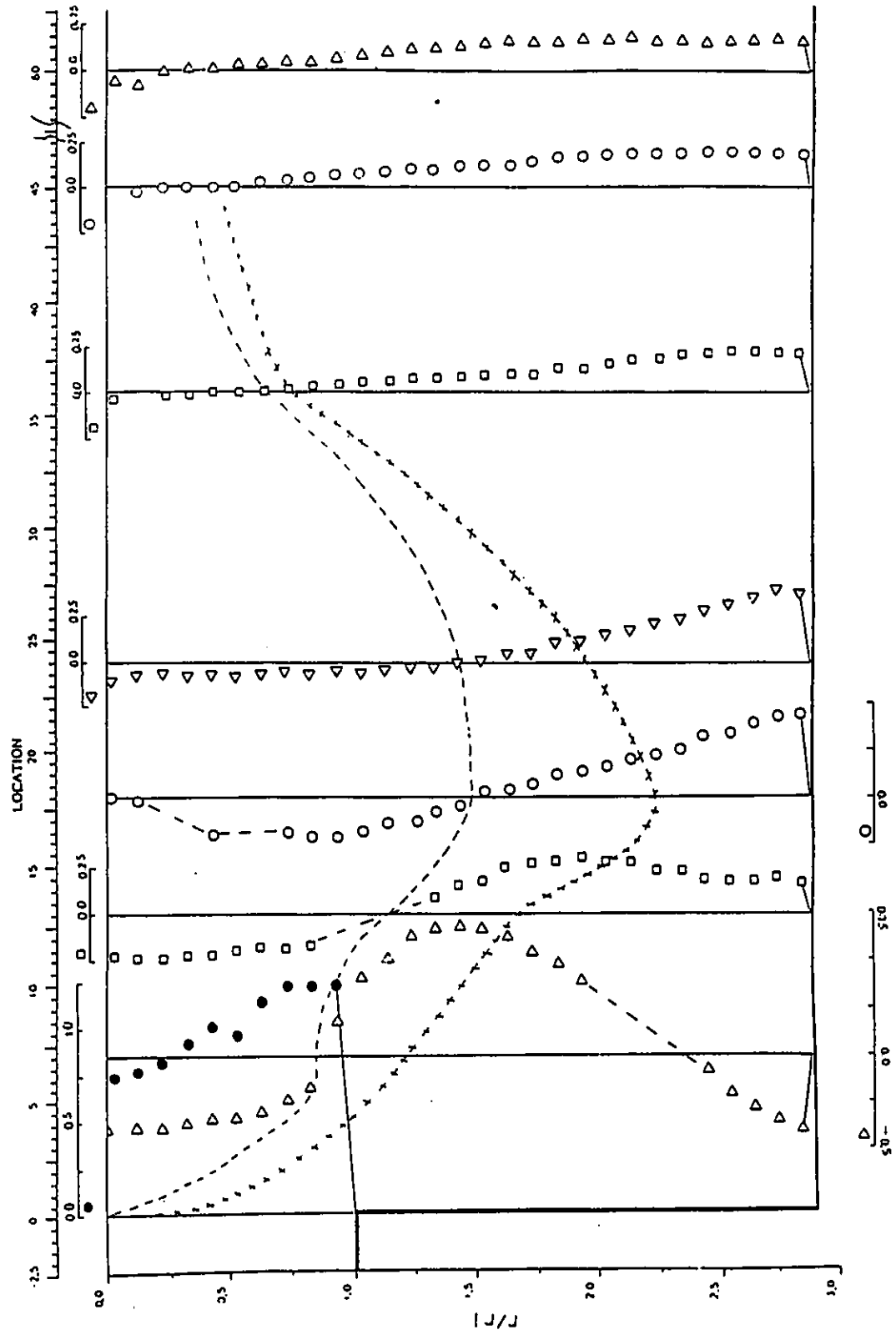

Figure 5.3: Axial Velocity Profiles for $r_2/r_1 = 2.813$, $\Omega = 0.506$

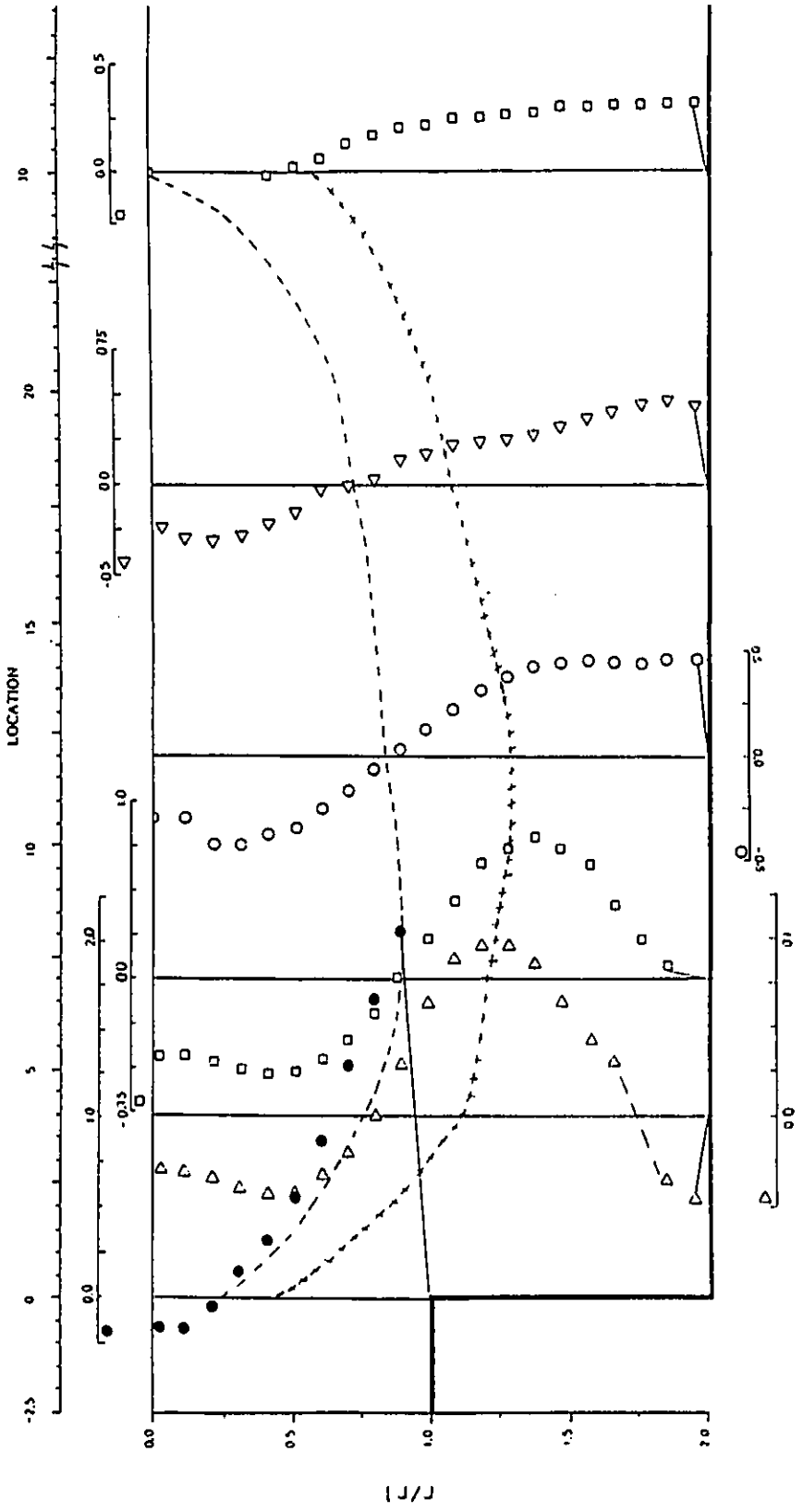

Figure 5.4: Axial Velocity Profiles for $r_2/r_1 = 2.0$, $\Omega = 1.437$

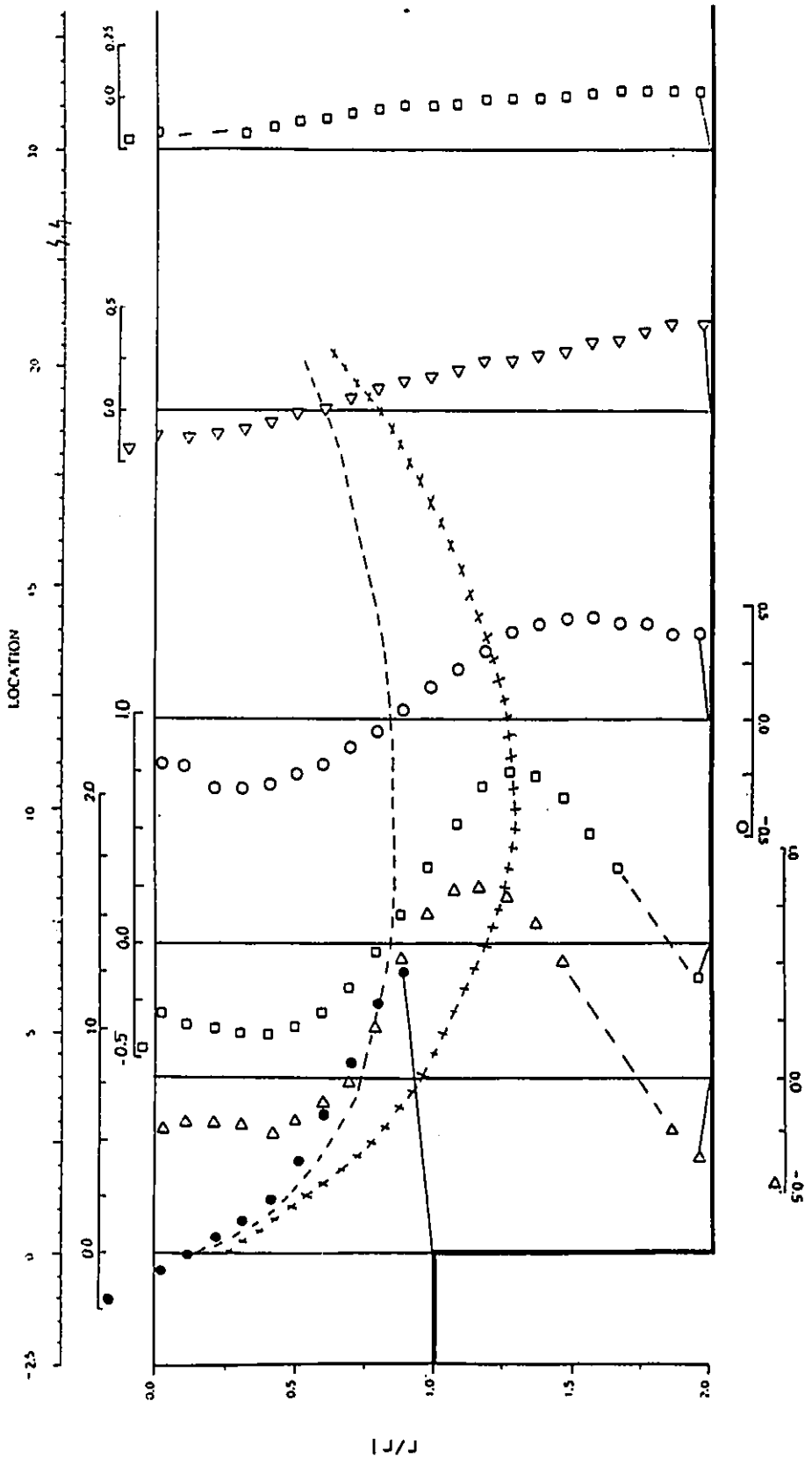

Figure 5.5: Axial Velocity Profiles for $r_2/r_1 = 2.0$, $\Omega = 1.129$

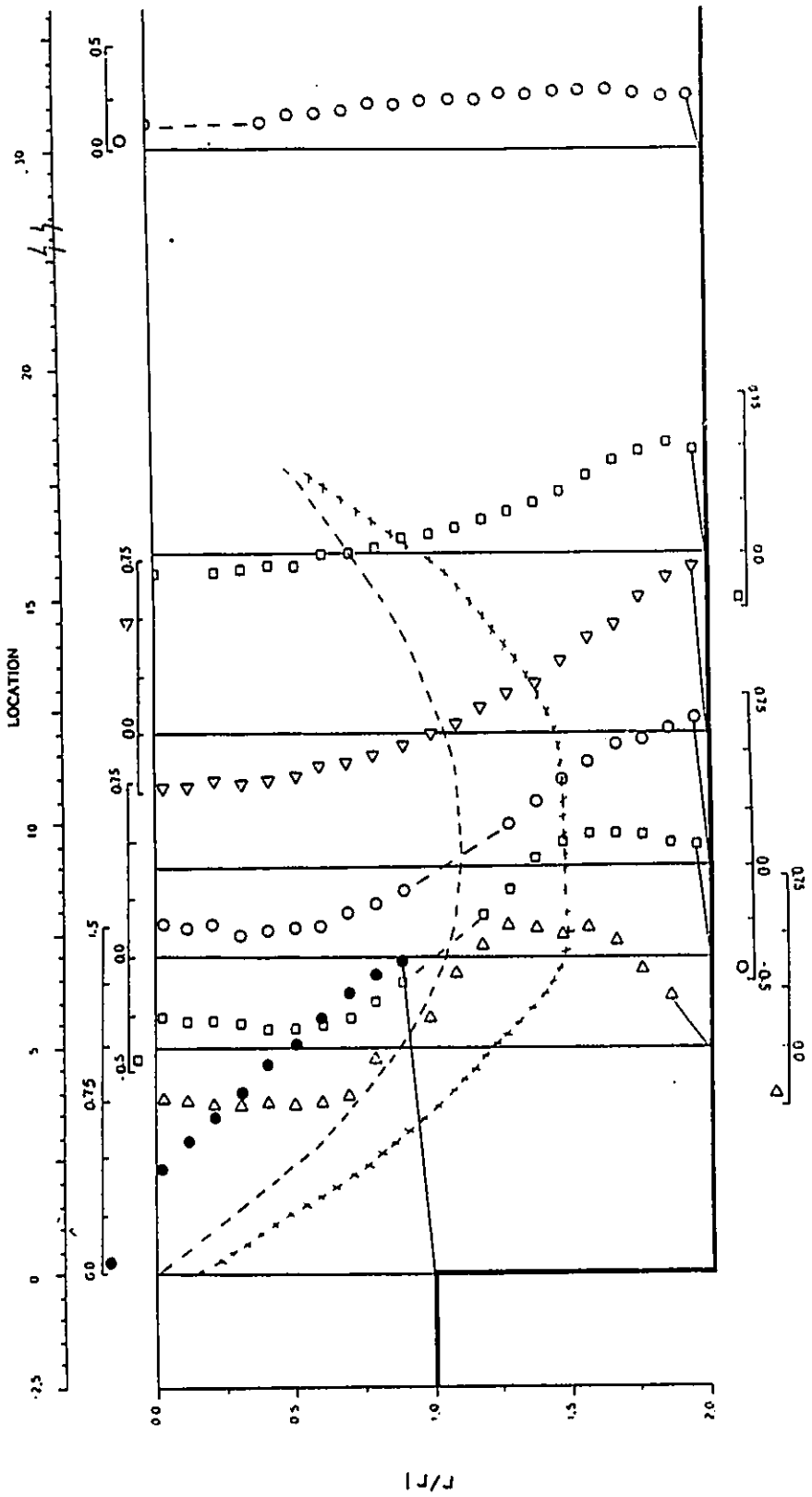

Figure 5.6: Axial Velocity Profiles for $r_2/r_1 = 2.0$, $\Omega = 0.676$

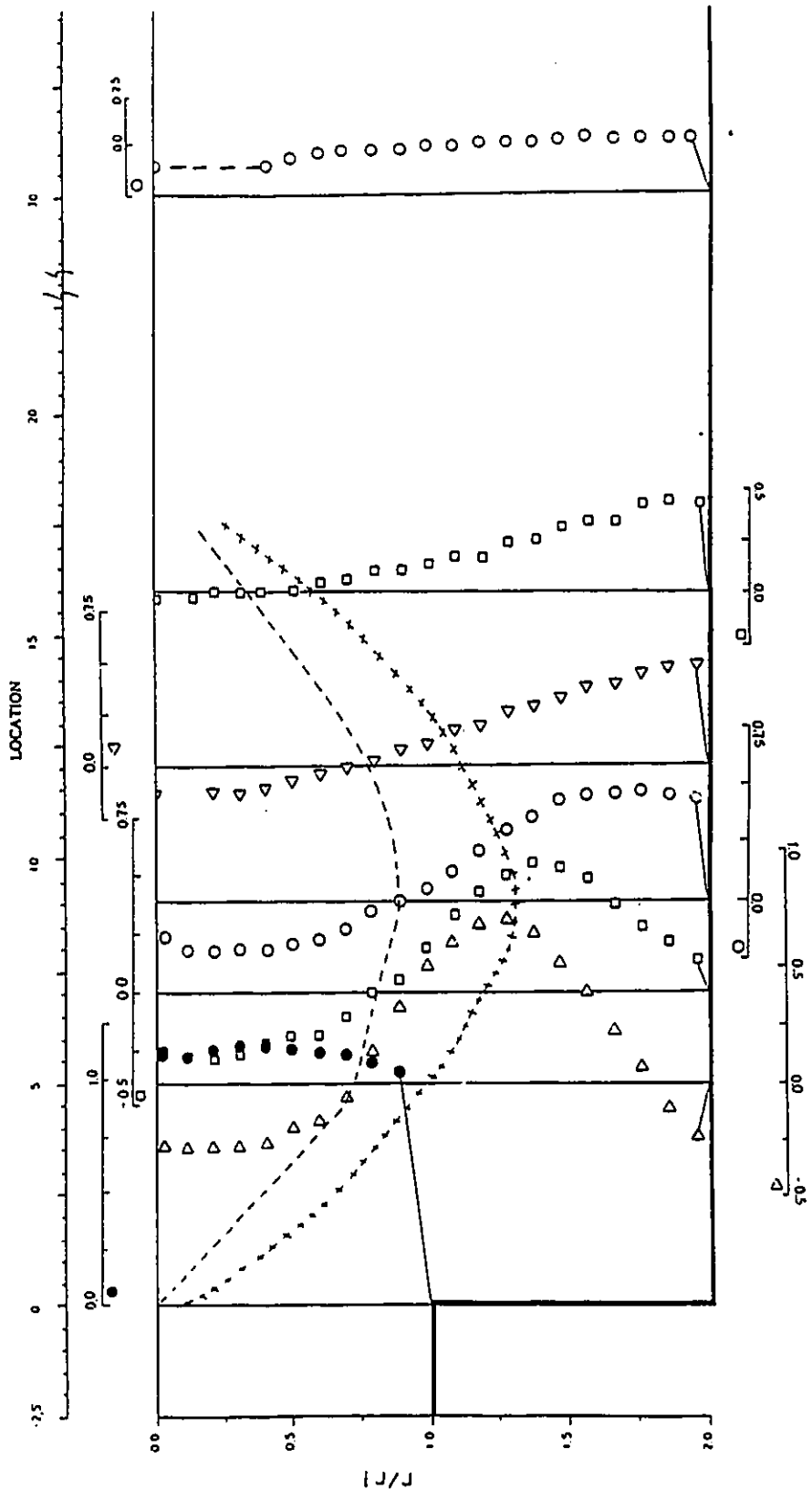

Figure 5.7: Axial Velocity Profiles for $r_2/r_1 = 2.0$, $\Omega = 0.452$

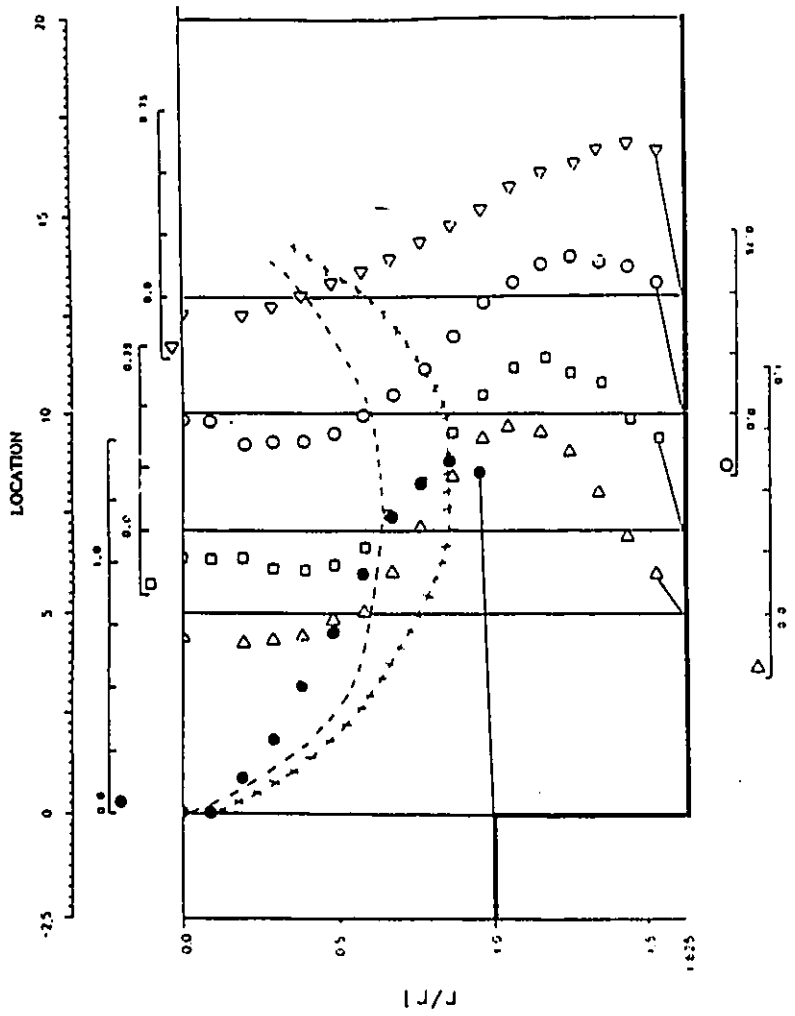

Figure 5.8: Axial Velocity Profiles for $r_2/r_1 = 1.625$, $\Omega = 0.641$

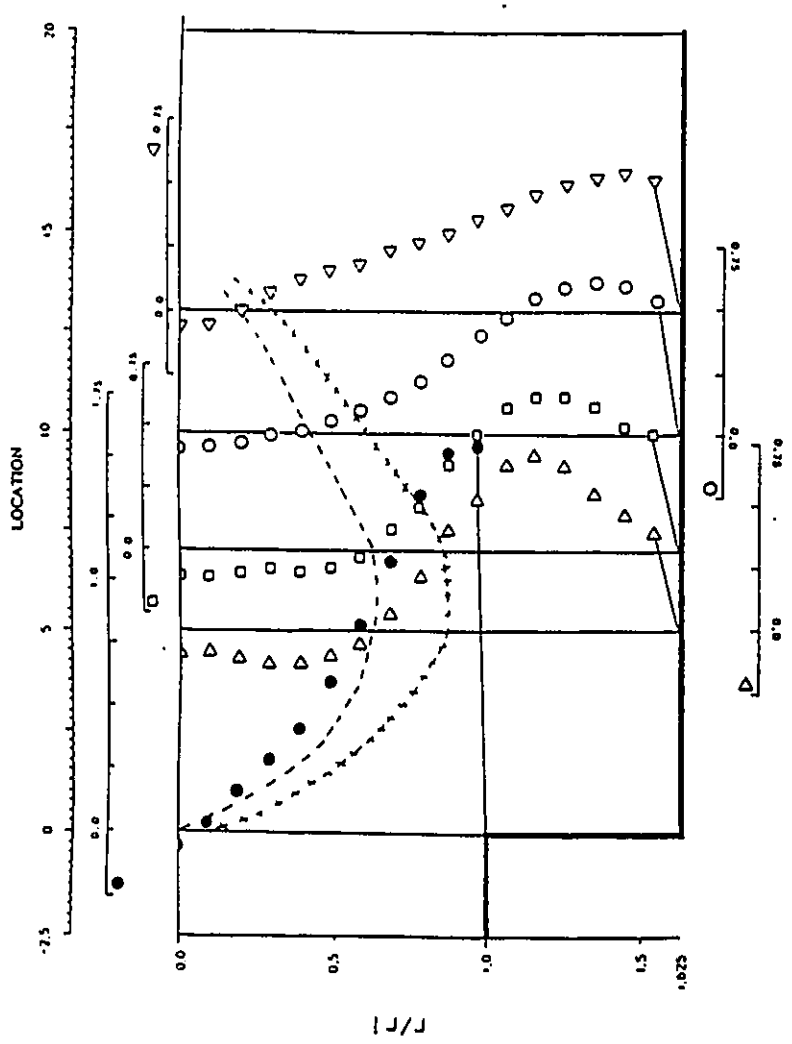

Figure 5.9: Axial Velocity Profiles for $r_2/r_1 = 1.625$, $\Omega = 0.58$

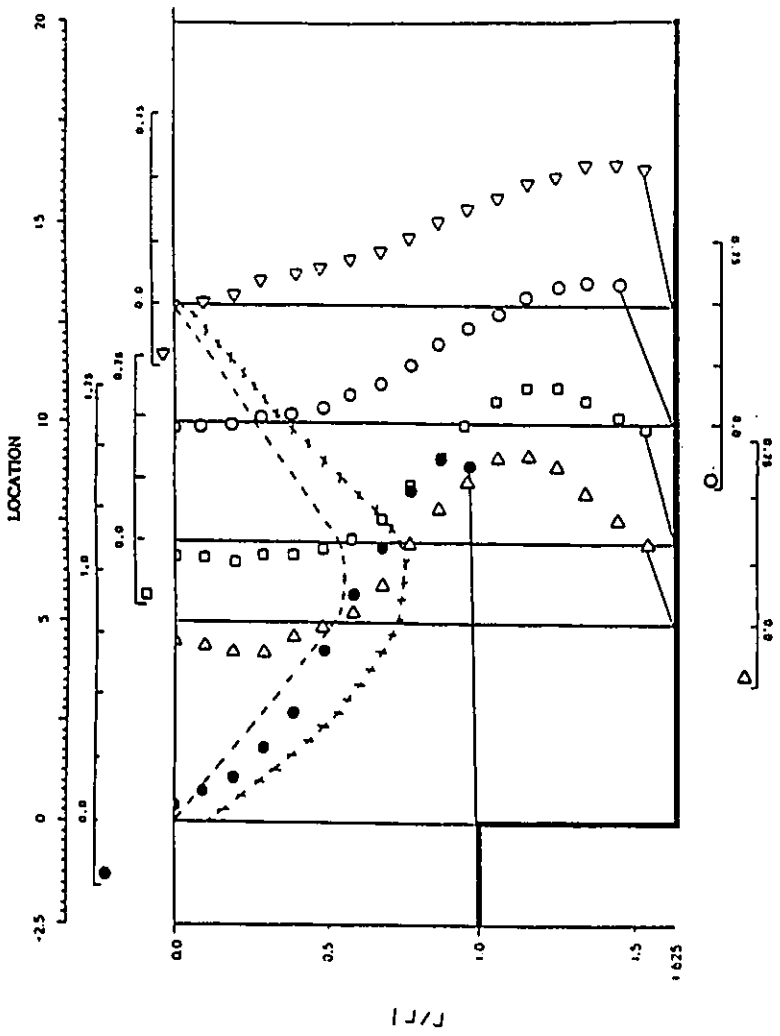

Figure 5.10: Axial Velocity Profiles for $r_2/r_1 = 1.625$, $\Omega = 0.511$

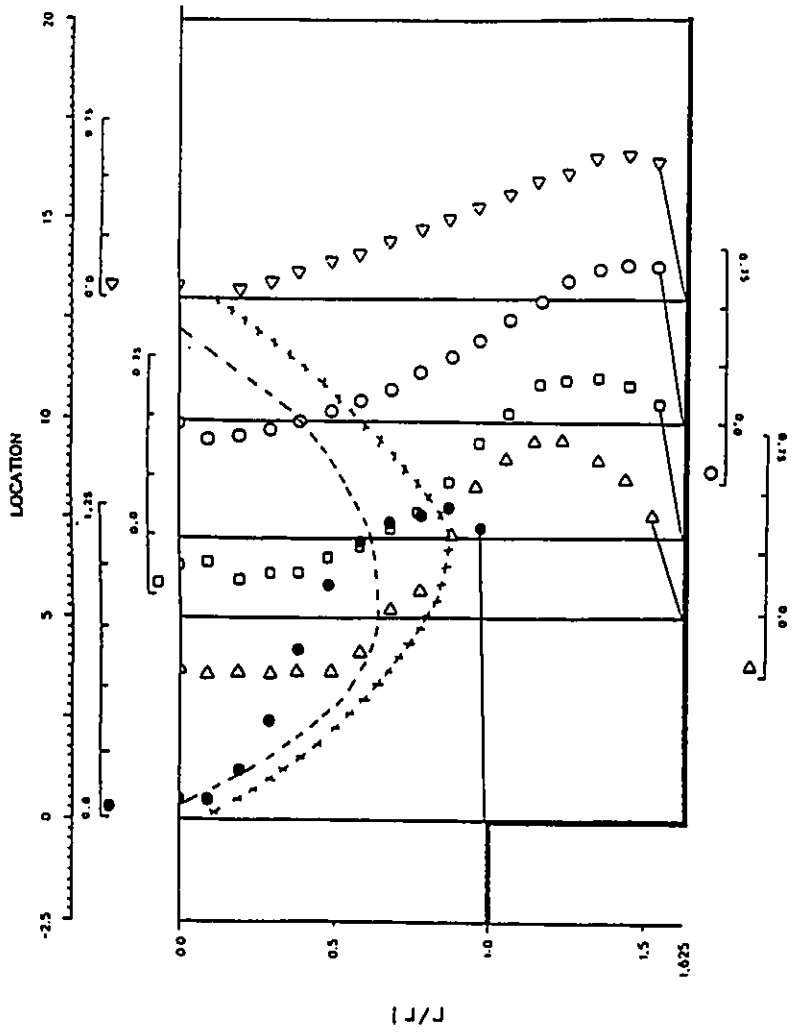

Figure 5.11: Axial Velocity Profiles for $r_2/r_1 = 1.625$, $\Omega = 0.485$

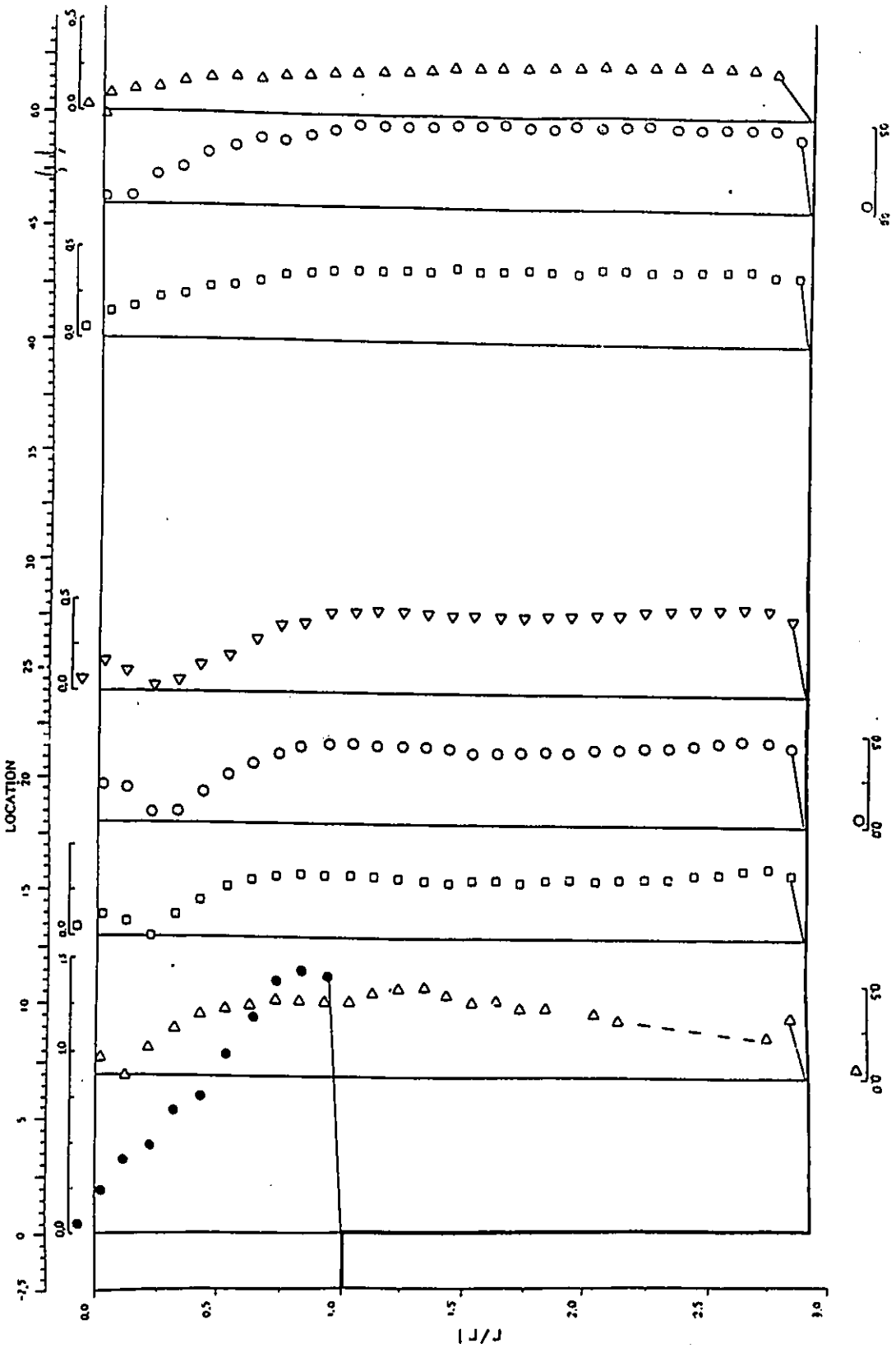

Figure 5.12: Tangential Velocity Profiles for $r_2/r_1 = 2.813$, $\Omega = 1.038$

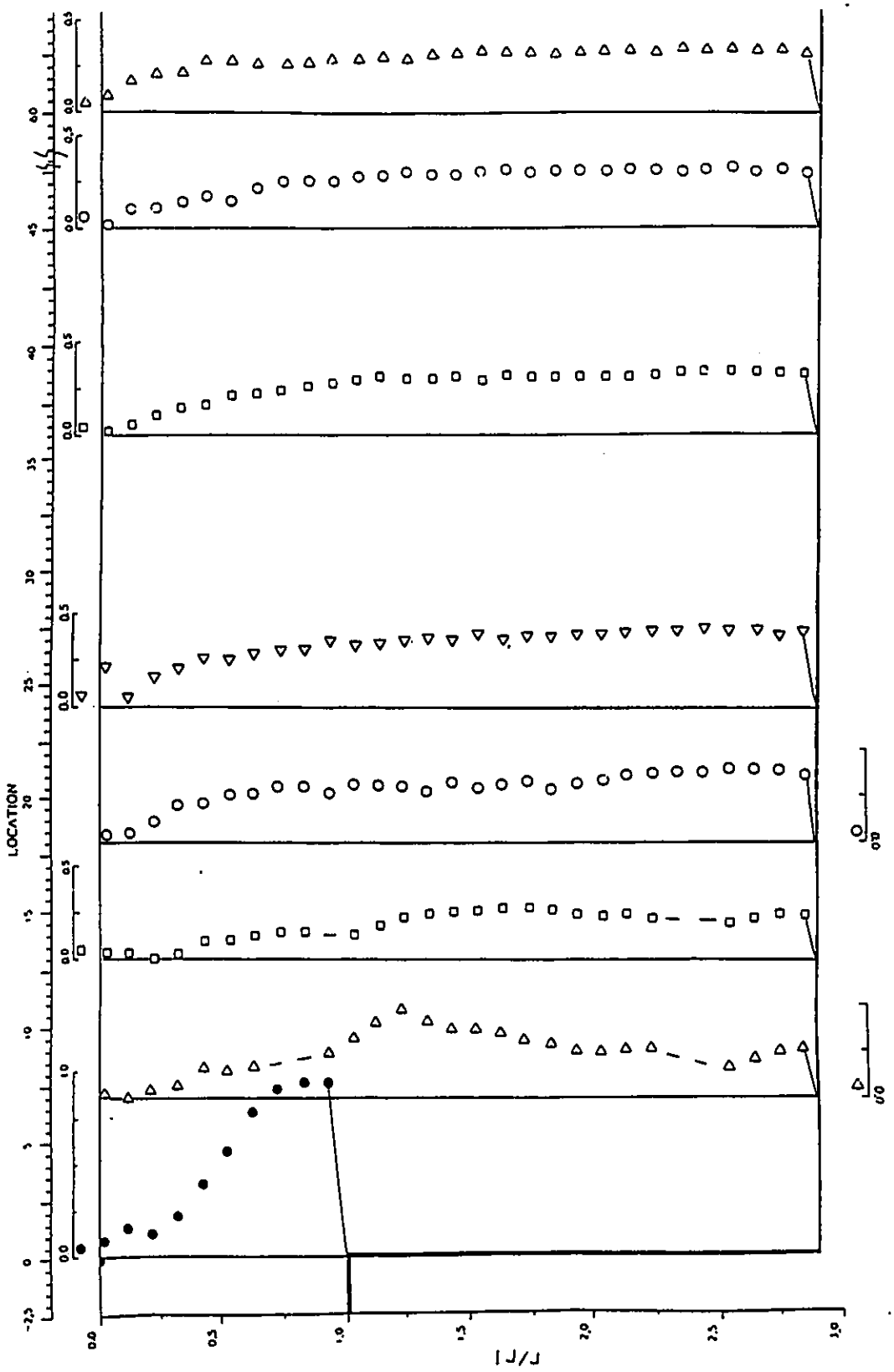

Figure 5.13: Tangential Velocity Profiles for $r_2/r_1 = 2.813$, $\Omega = 0.639$

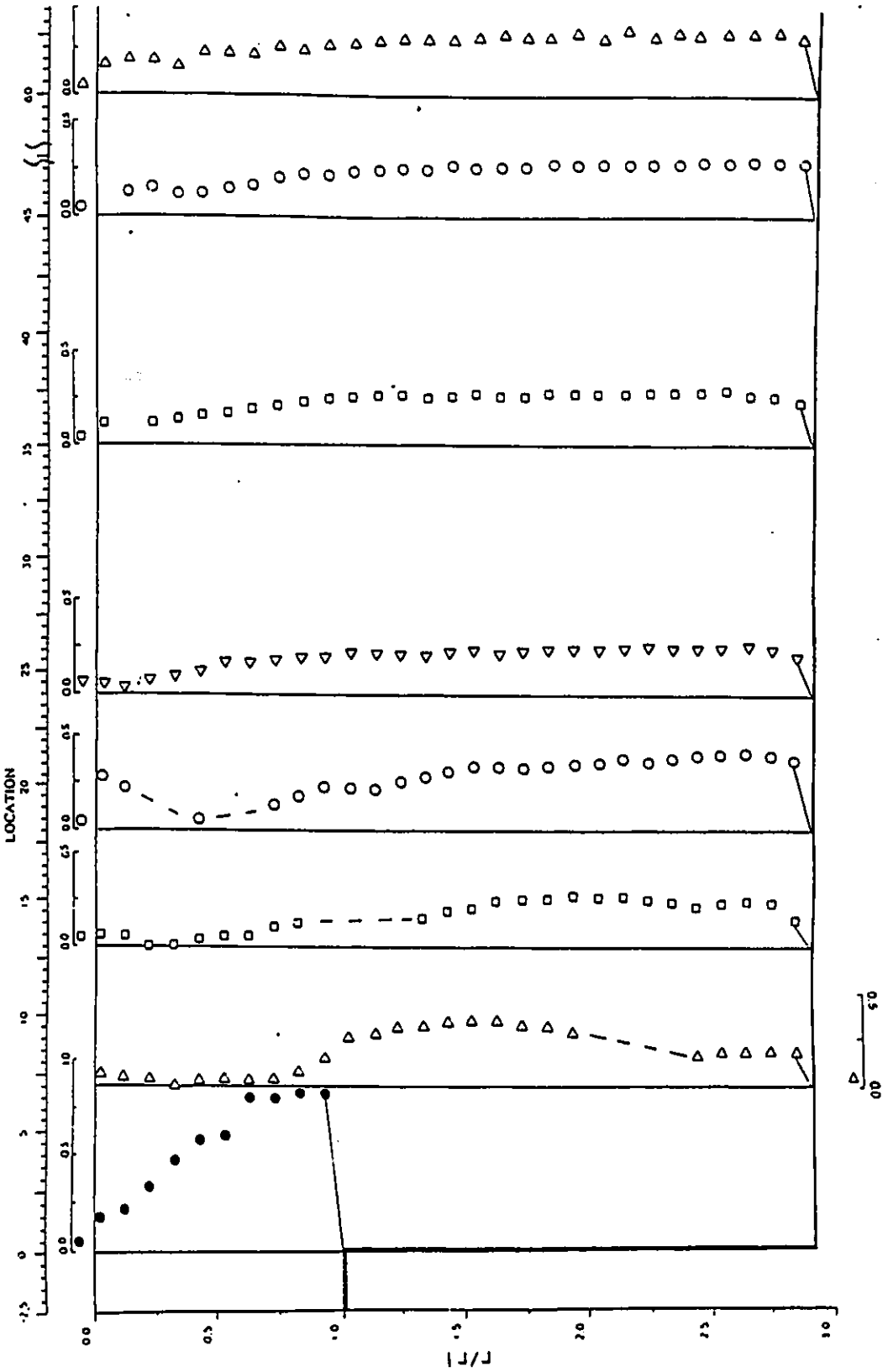

Figure 5.14: Tangential Velocity Profiles for $r_2/r_1 = 2.813$, $\Omega = 0.506$

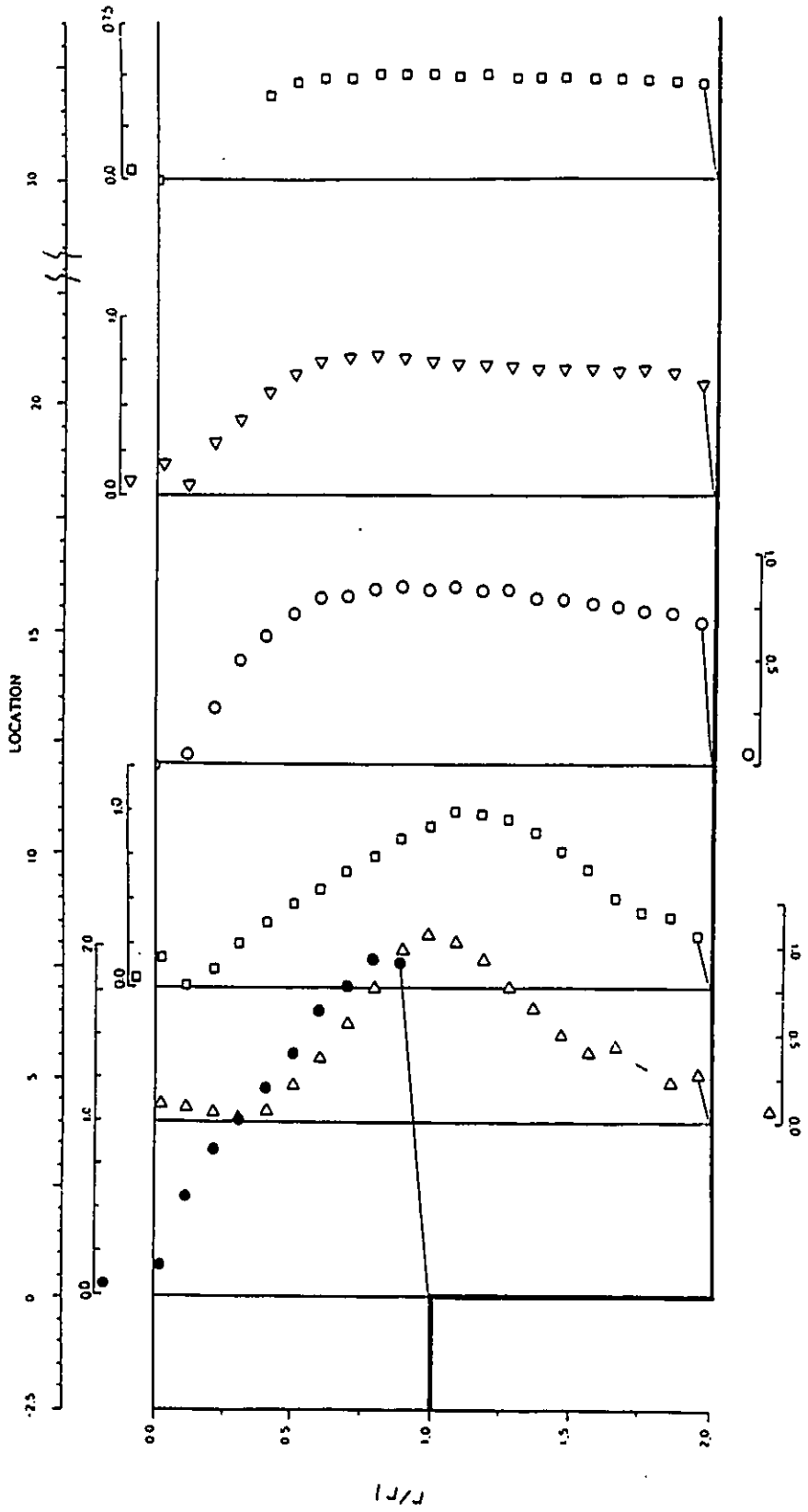

Figure 5.15: Tangential Velocity Profiles for r_2/r_1=2.0, Ω = 1.437

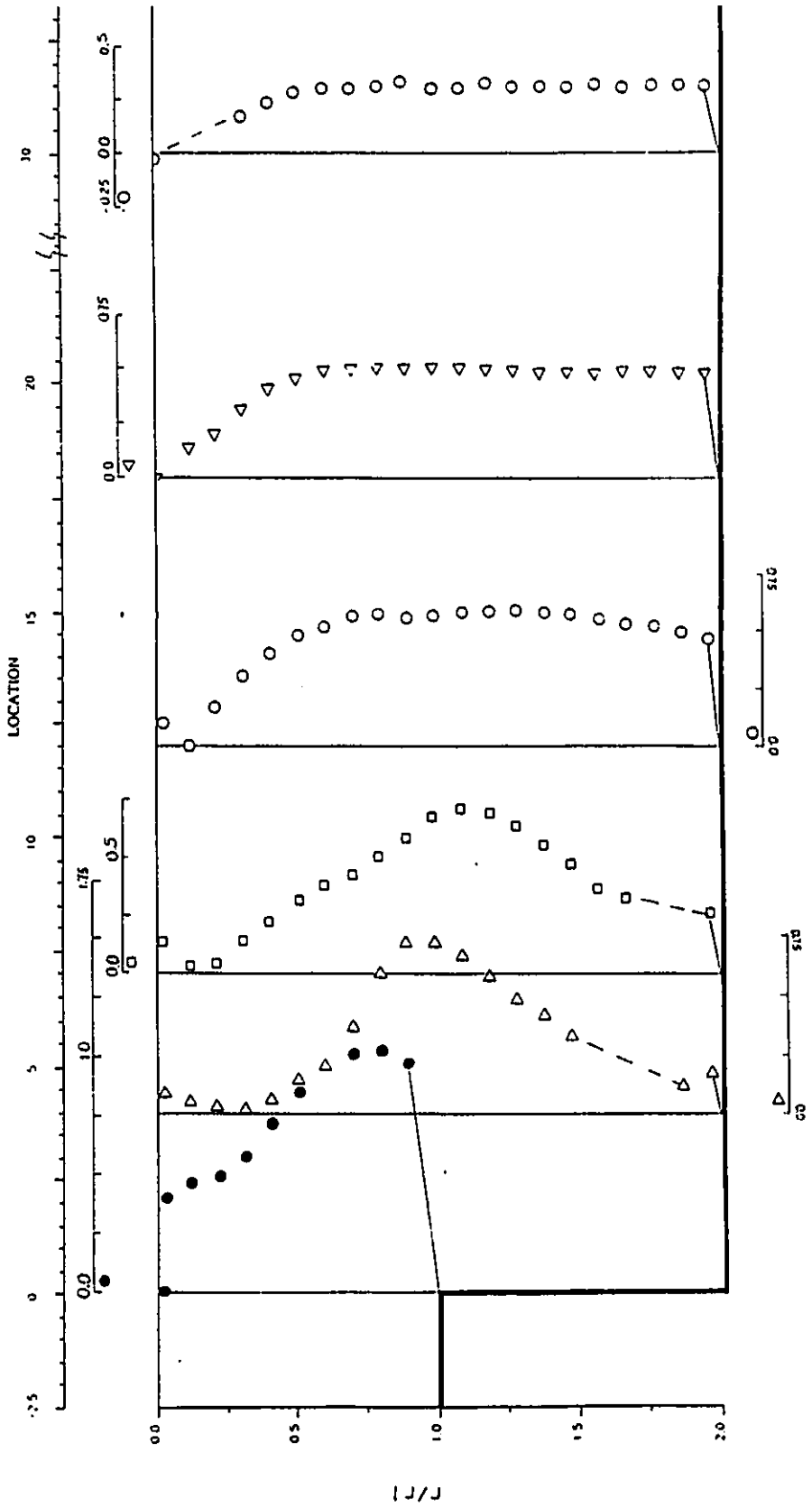

Figure 5.16: Tangential Velocity Profiles for $r_2/r_1 = 2.0$, $\Omega = 1.129$

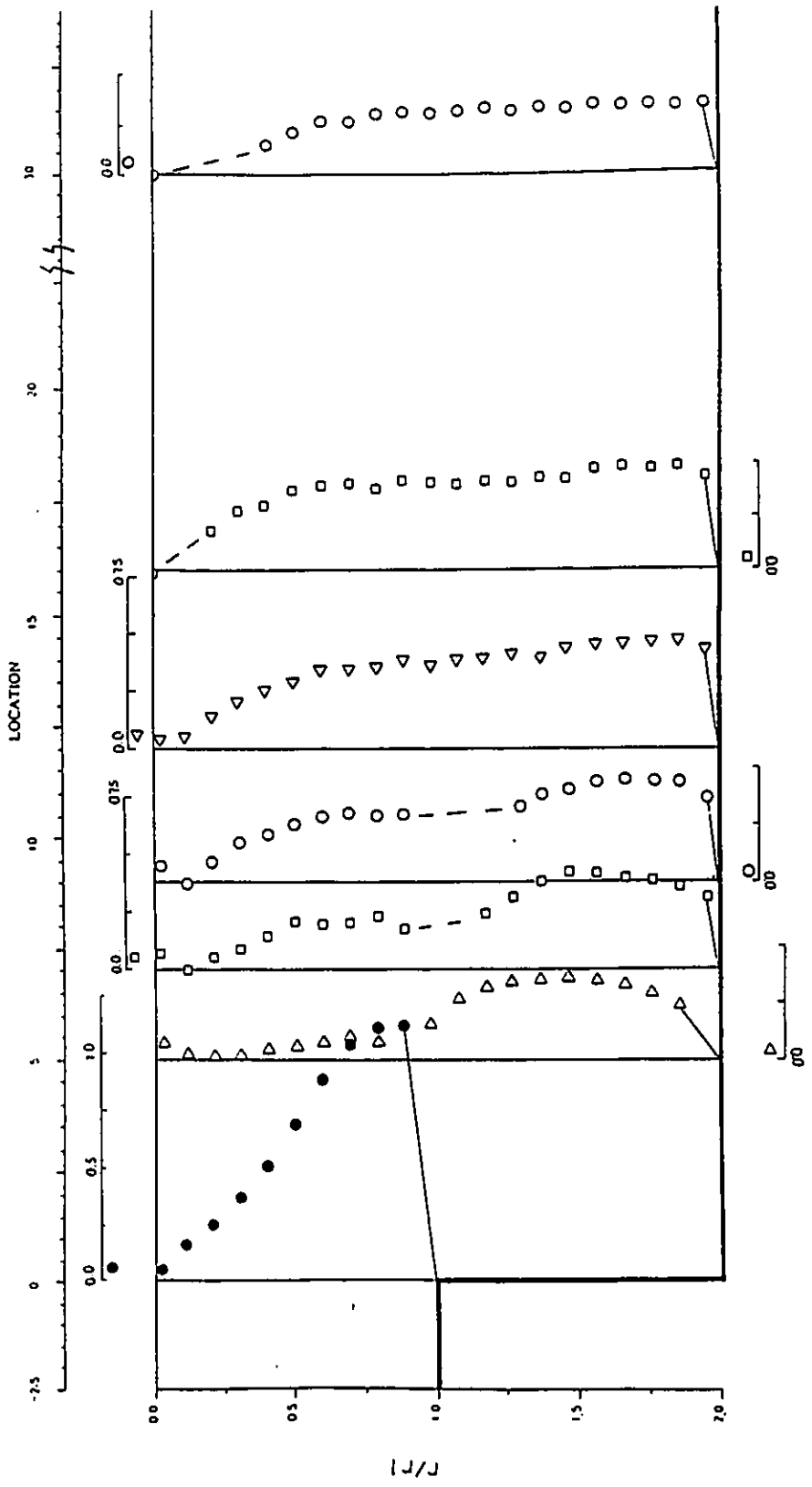

Figure 5.17: Tangential Velocity Profiles for $r_2/r_1 = 2.0$, $\Omega = 0.676$

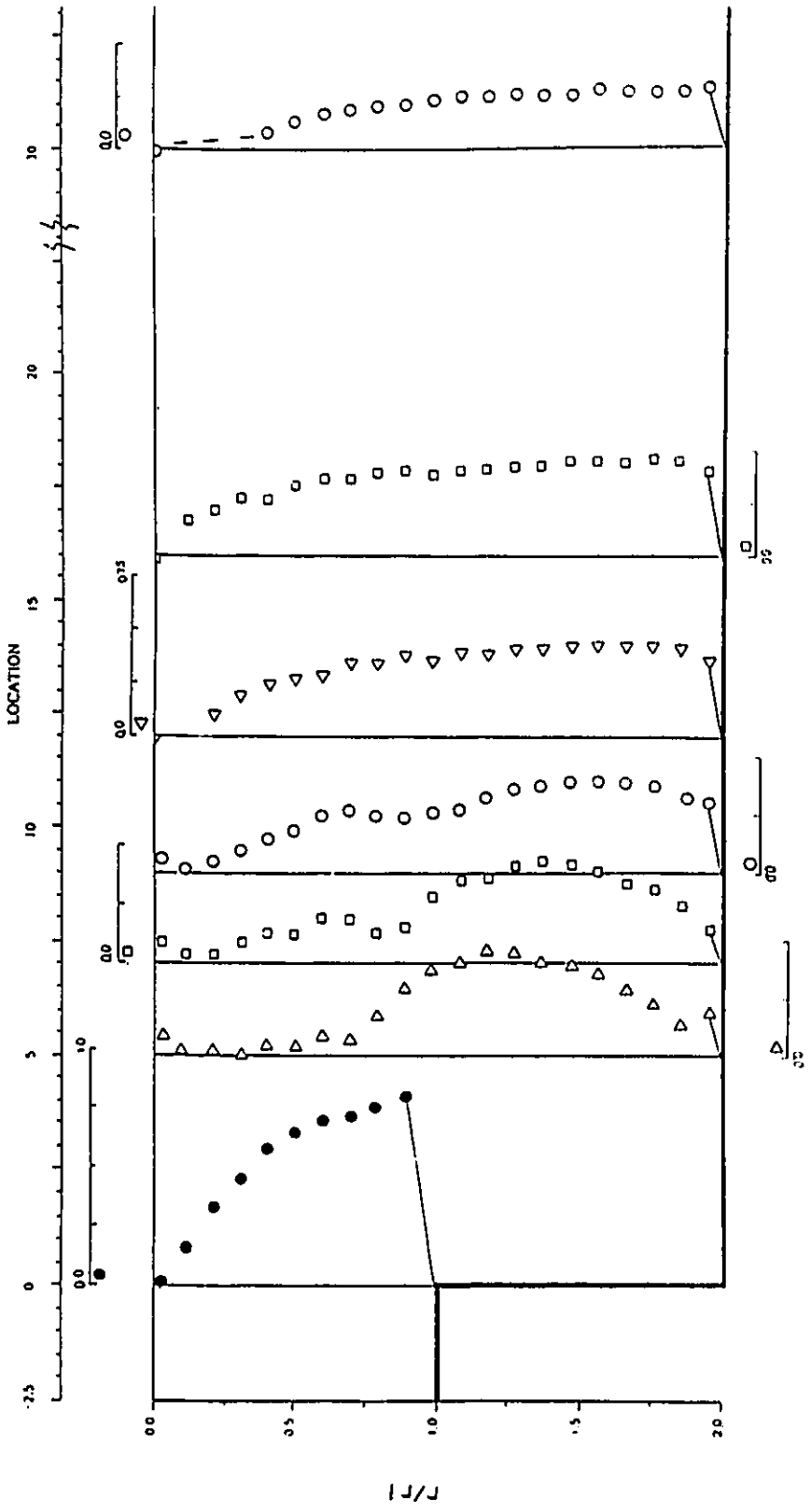

Figure 5.18: Tangential Velocity Profiles for $r_2/r_1 = 2.0$, $\Omega = 0.452$

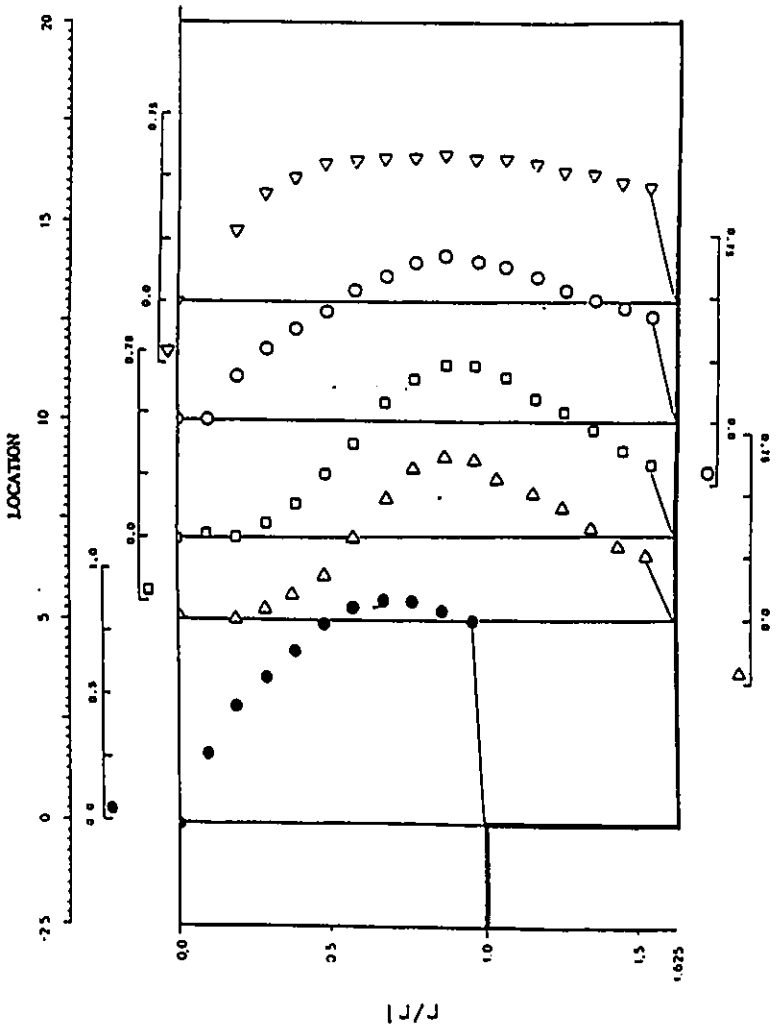

Figure 5.19: Tangential Velocity Profiles for $r_2/r_1 = 1.625$, $\Omega = 0.641$

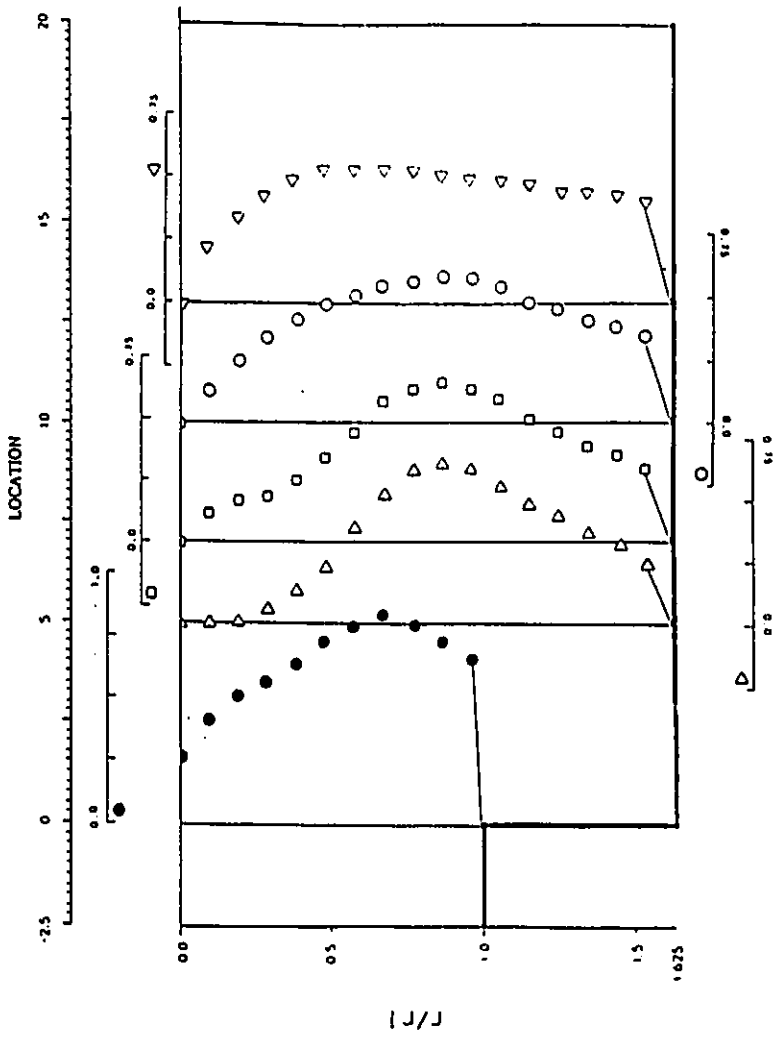

Figure 5.20: Tangential Velocity Profiles for $r_2/r_1 = 1.625$, $\Omega = 0.58$

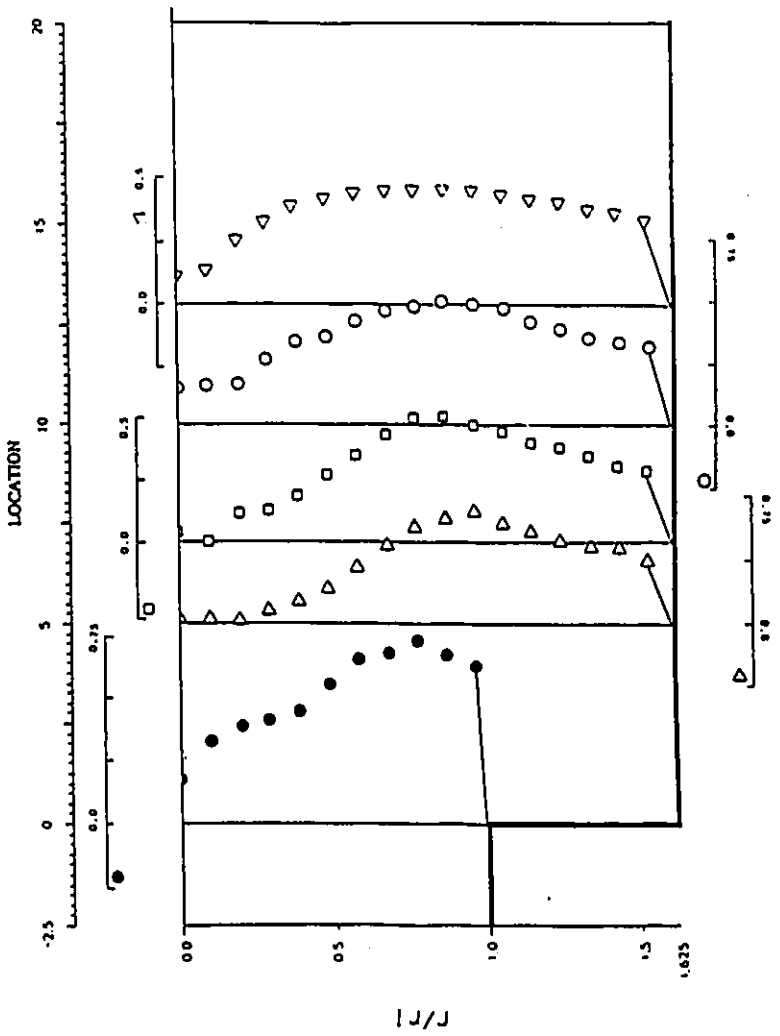

Figure 5.21: Tangential Velocity Profiles for $r_2/r_1 = 1.625$, $\Omega = 0.511$

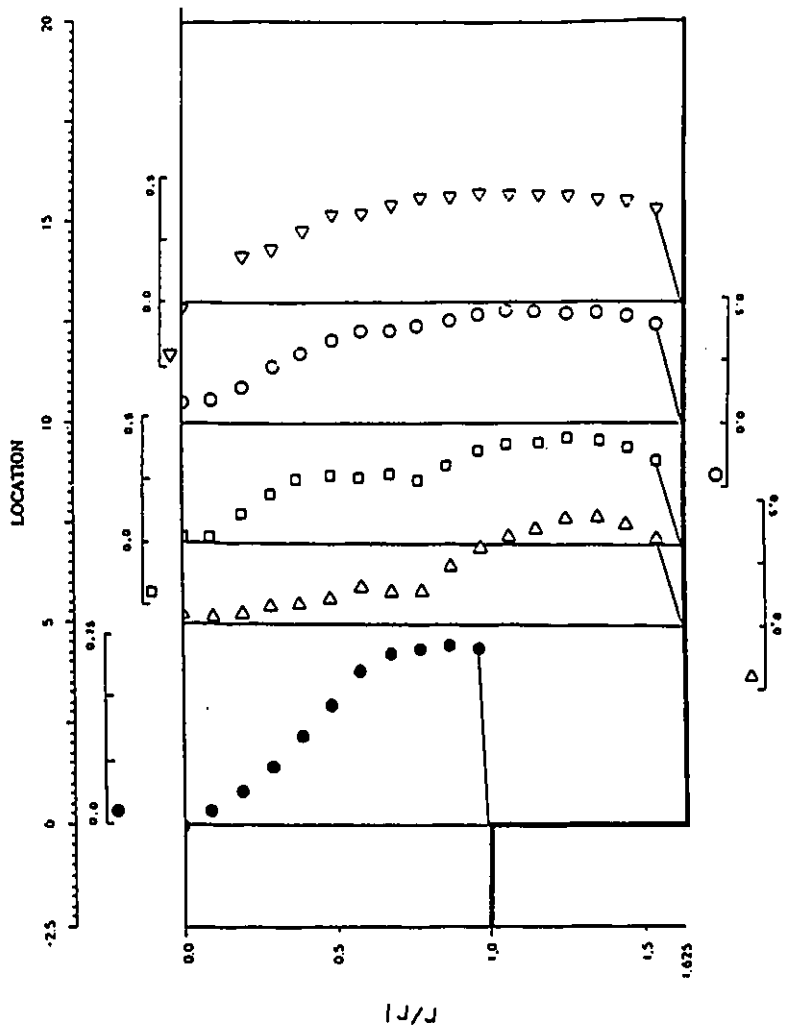

Figure 5.22: Tangential Velocity Profiles for $r_2/r_1 = 1.625$, $\Omega = 0.485$

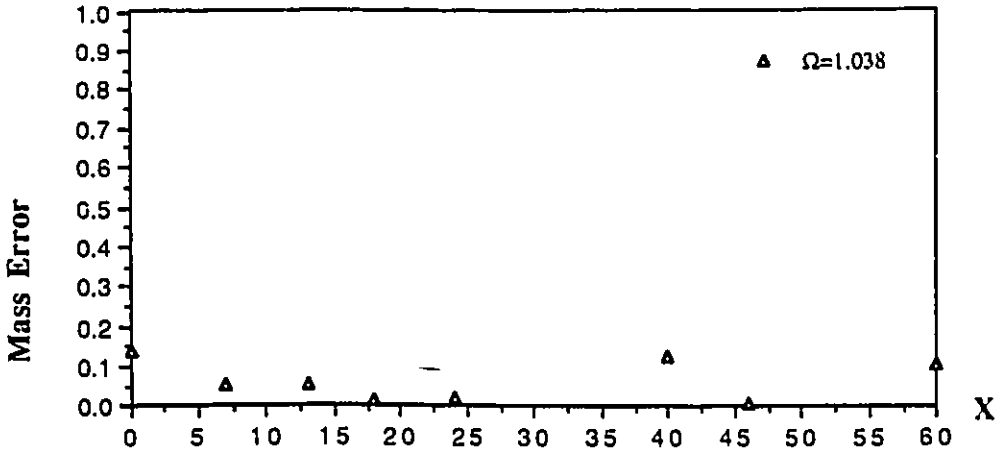

Figure 5.23: Mass Error Fraction vs. X for $r_2/r_1 = 2.813$, $\Omega = 1.038$

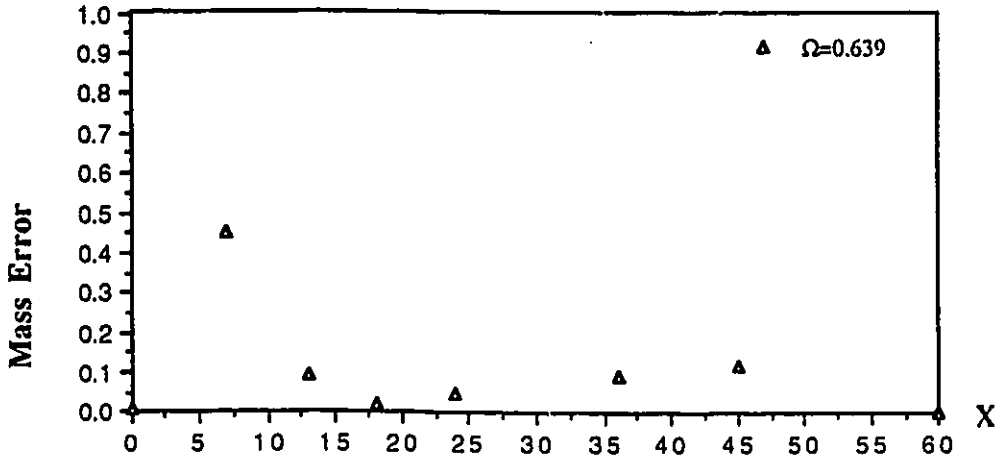

Figure 5.24: Mass Error Fraction vs. X for $r_2/r_1 = 2.813$, $\Omega = 0.639$

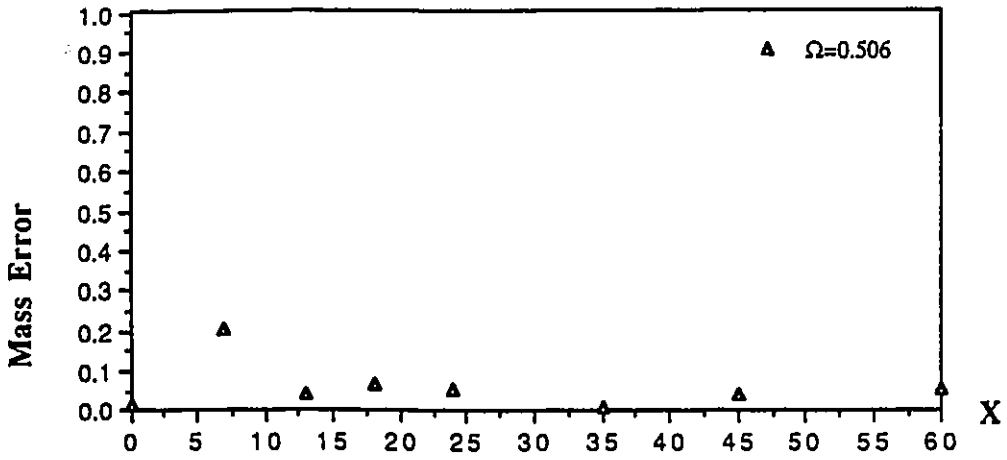

Figure 5.25: Mass Error Fraction vs. X for $r_2/r_1 = 2.813$, $\Omega = 0.506$

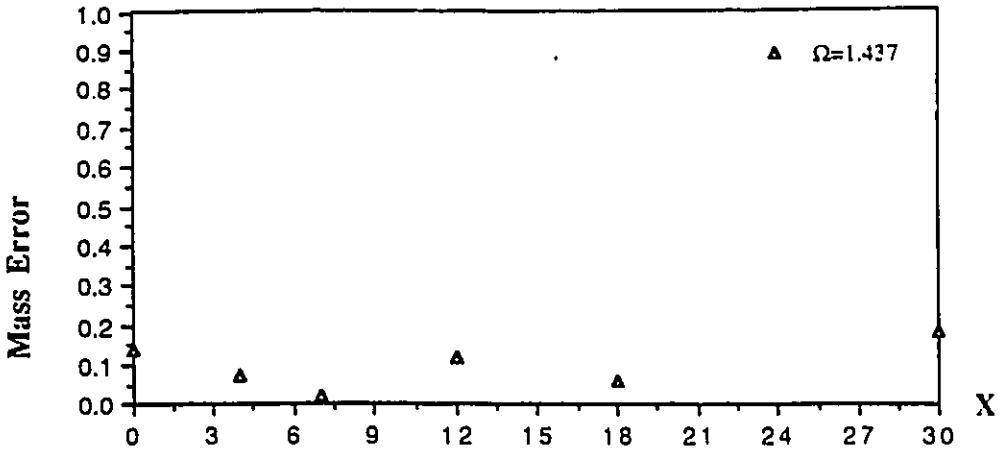

Figure 5.26: Mass Error Fraction vs. X for $r_2/r_1 = 2.0$, $\Omega = 1.437$

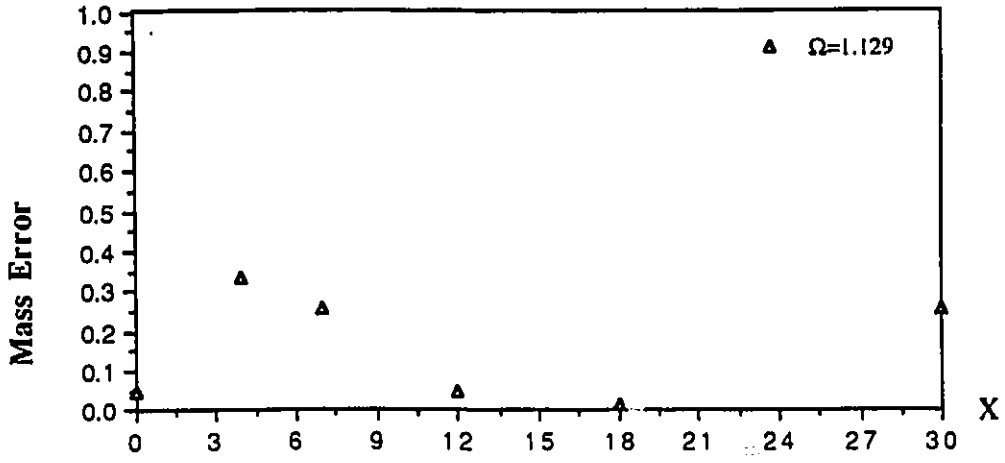

Figure 5.27: Mass Error Fraction vs. X for $r_2/r_1 = 2.0$, $\Omega = 1.129$

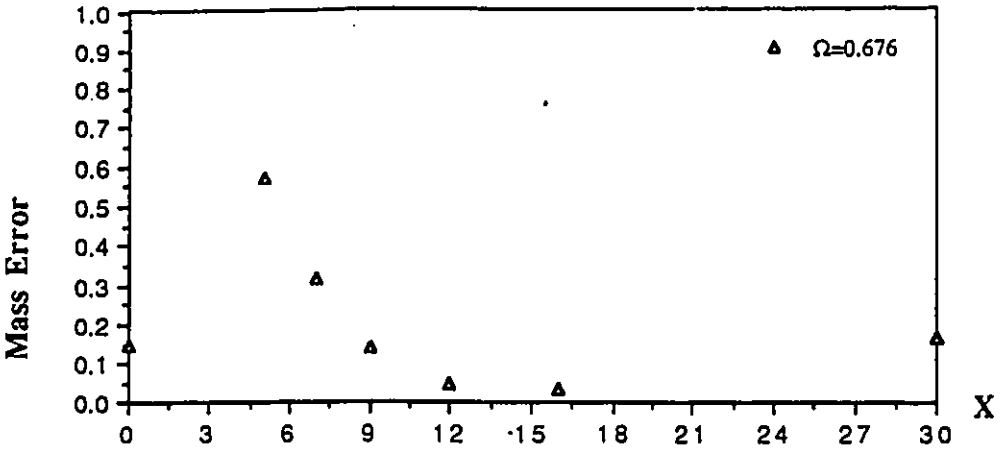

Figure 5.28: Mass Error Fraction vs. X for $r_2/r_1 = 2.0$, $\Omega = 0.676$

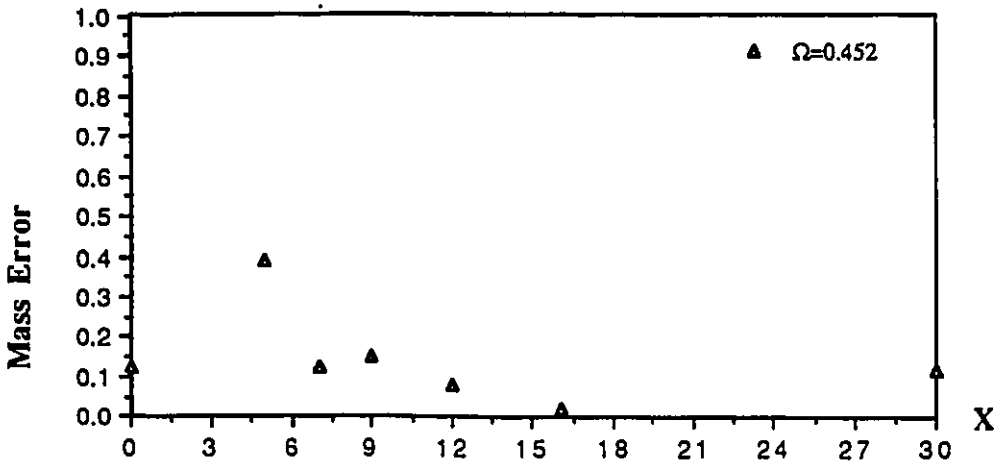

Figure 5.29: Mass Error Fraction vs. X for $r_2/r_1 = 2.0$, $\Omega = 0.452$

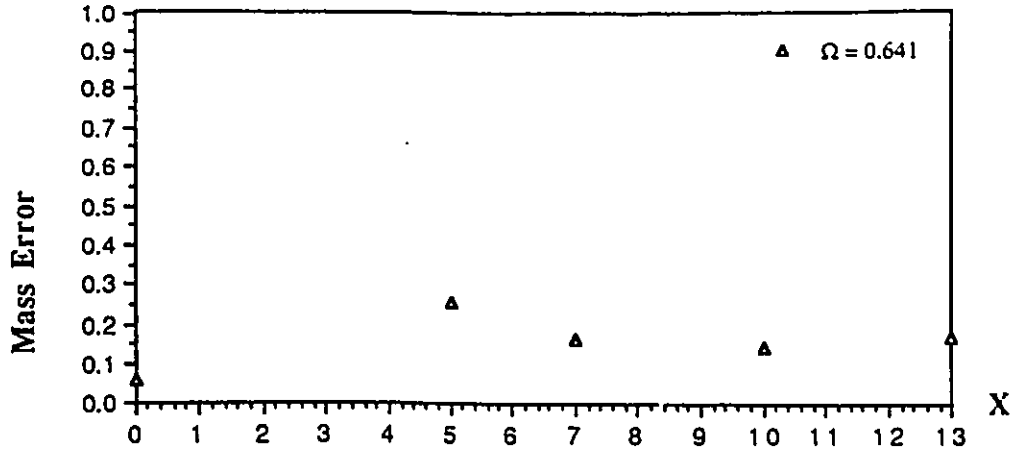

Figure 5.30: Mass Error Fraction vs. X for $r_2/r_1 = 1.625$, $\Omega = 0.641$

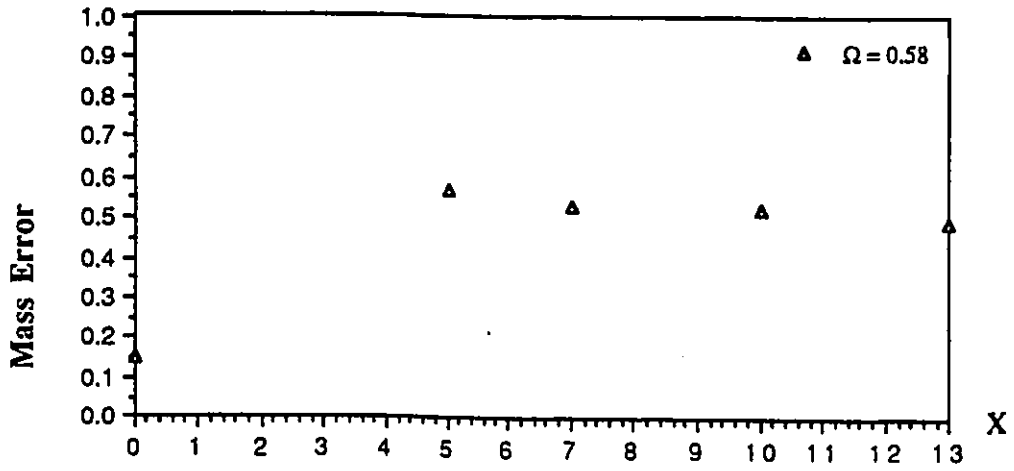

Figure 5.31: Mass Error Fraction vs. X for $r_2/r_1 = 1.625$, $\Omega = 0.58$

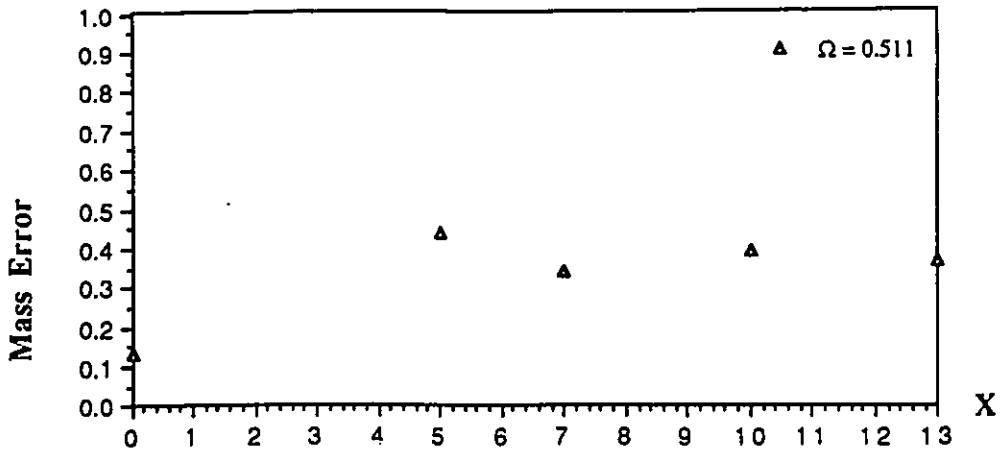

Figure 5.32: Mass Error Fraction vs. X for $r_2/r_1 = 1.625$, $\Omega = 0.511$

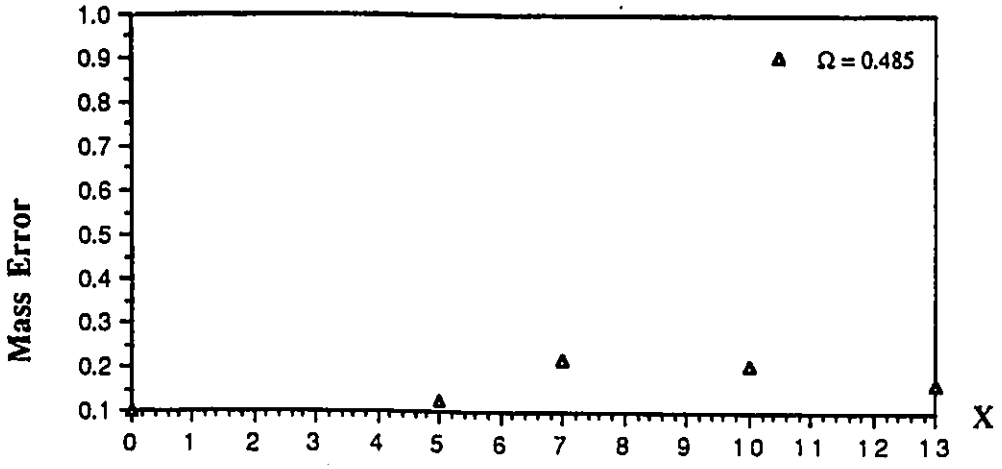

Figure 5.33: Mass Error Fraction vs. X for $r_2/r_1 = 1.625$, $\Omega = 0.485$

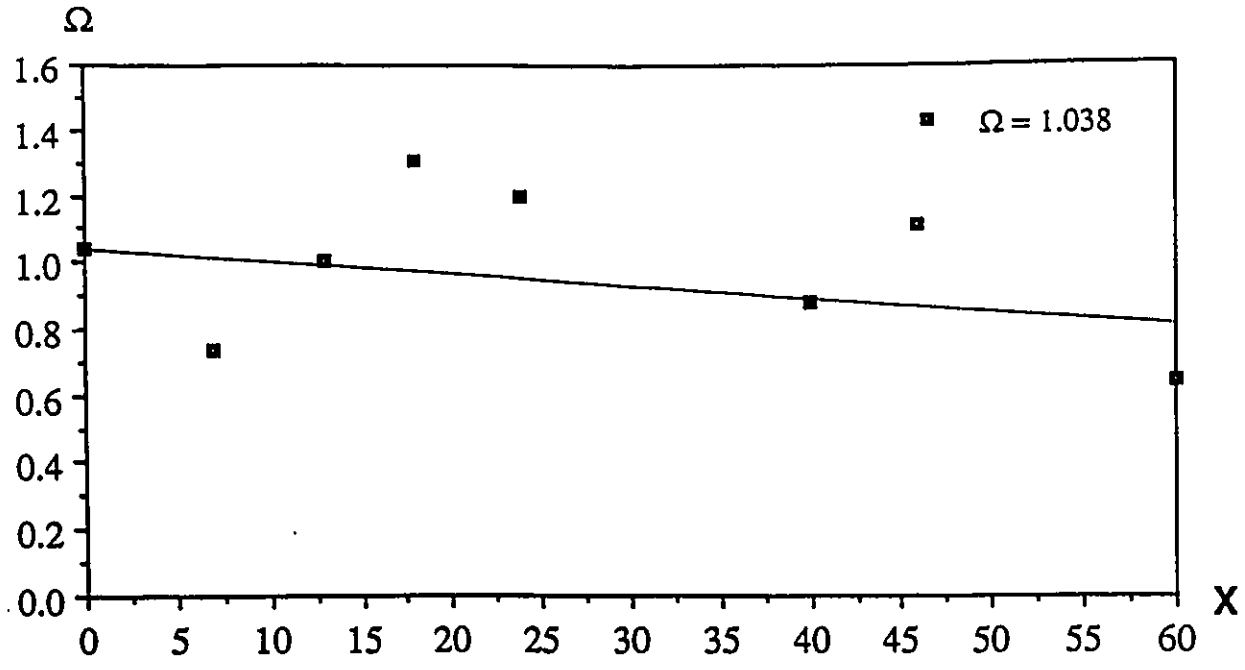

Figure 5.34: Ω vs. X for $r_2/r_1 = 2.813$, $\Omega = 1.038$

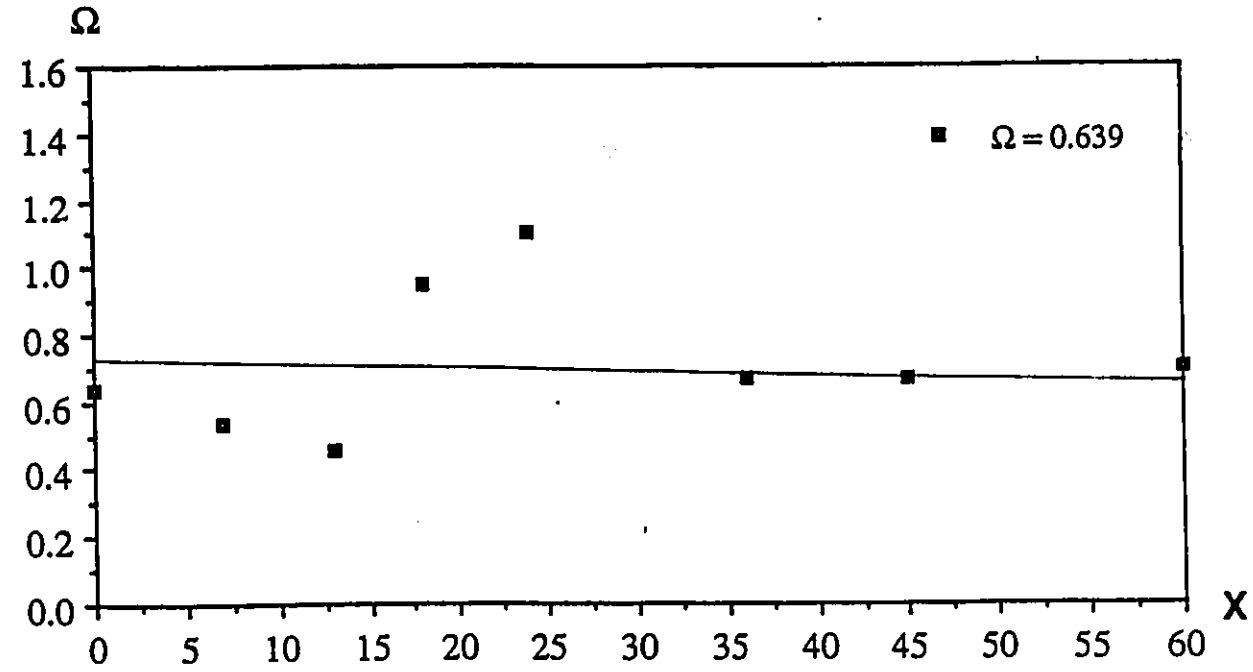

Figure 5.35: Ω vs. X for $r_2/r_1 = 2.813$, $\Omega = 0.639$

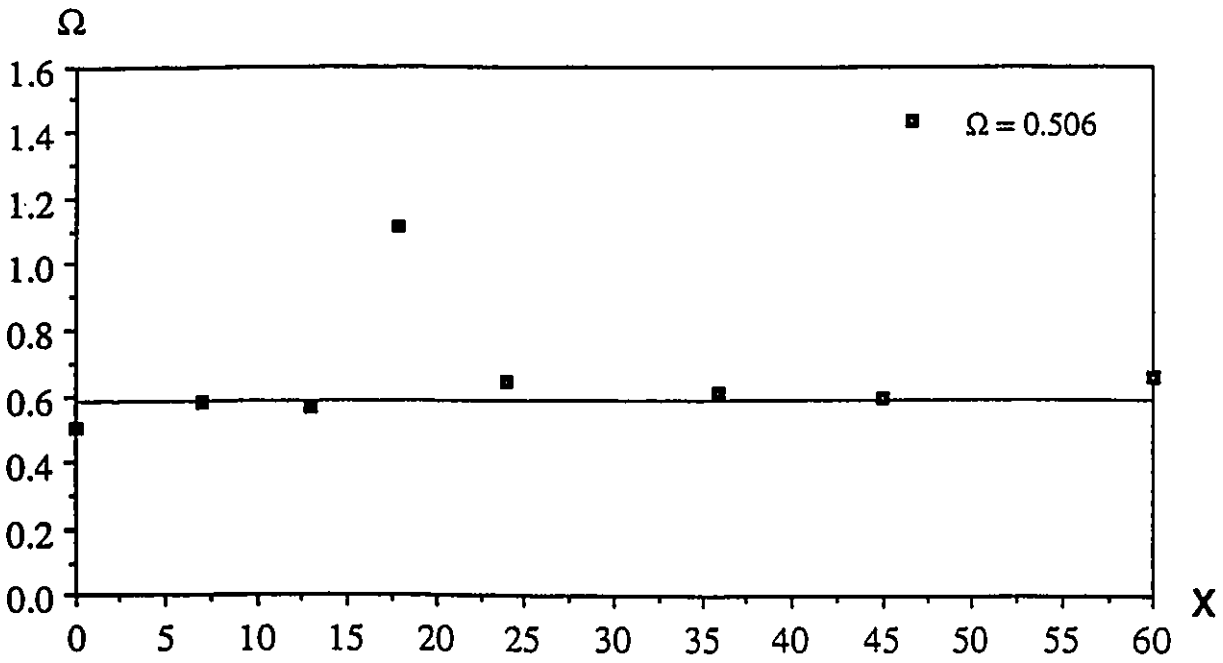

Figure 5.36: Ω vs. X for $r_2/r_1 = 2.813$, $\Omega = 0.506$

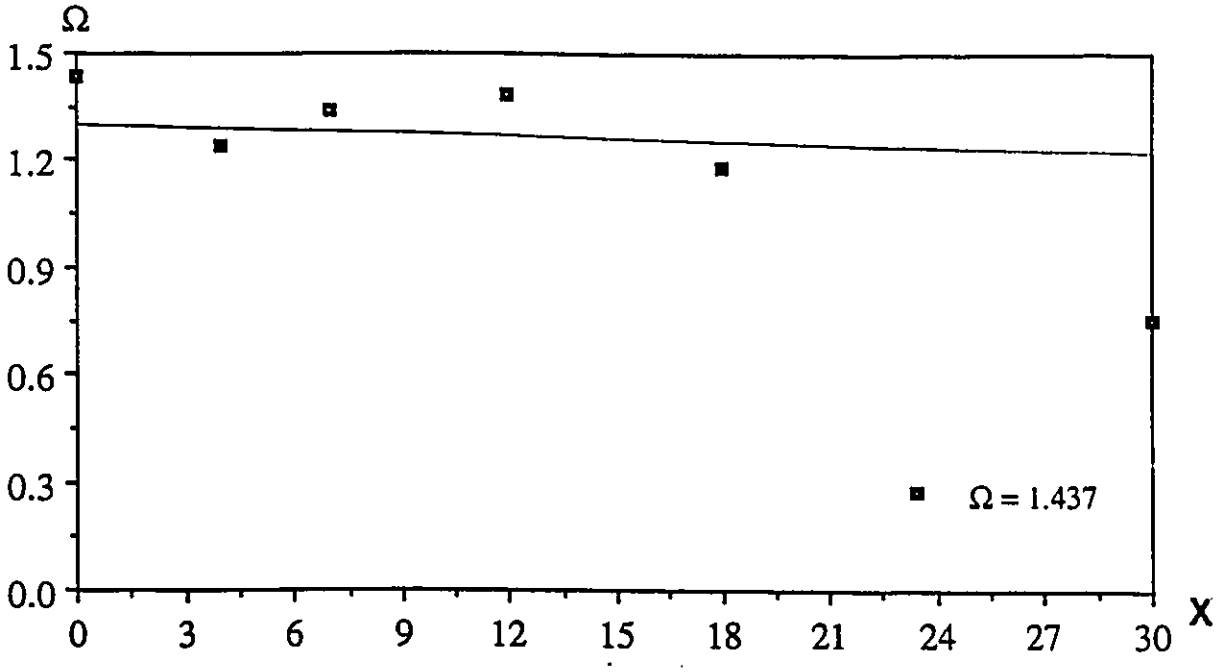

Figure 5.37: Ω vs. X for $r_2/r_1 = 2.0$, $\Omega = 1.437$

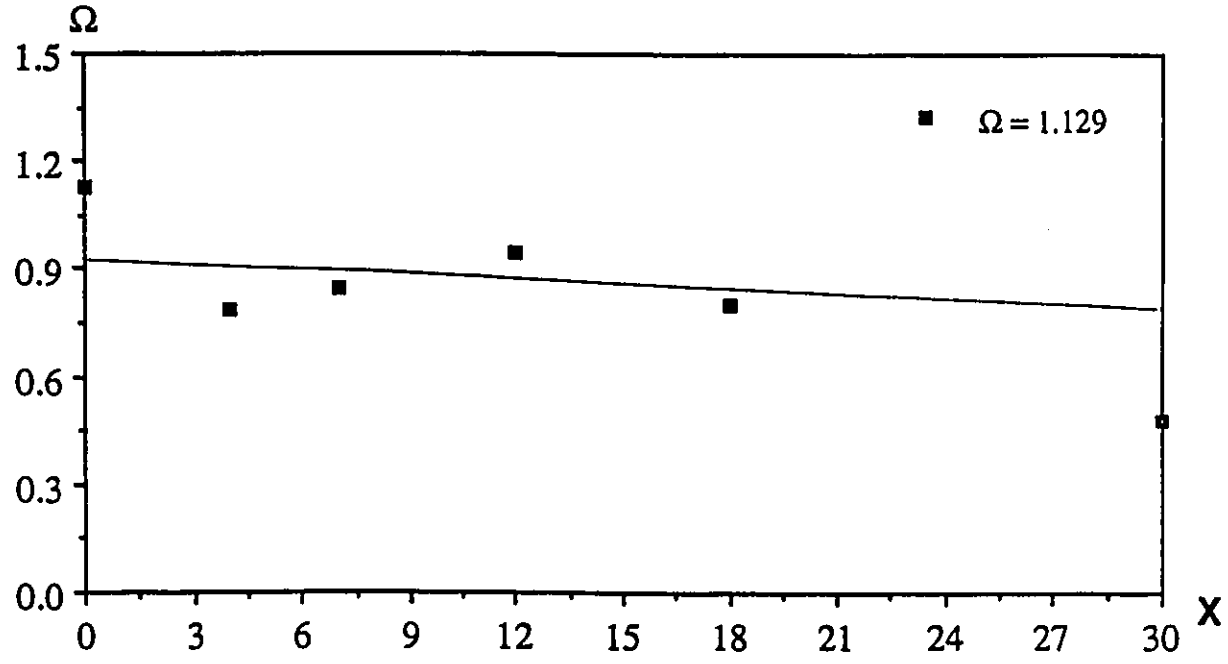

Figure 5.38: Ω vs. X for $r_2/r_1 = 2.0$, $\Omega = 1.129$

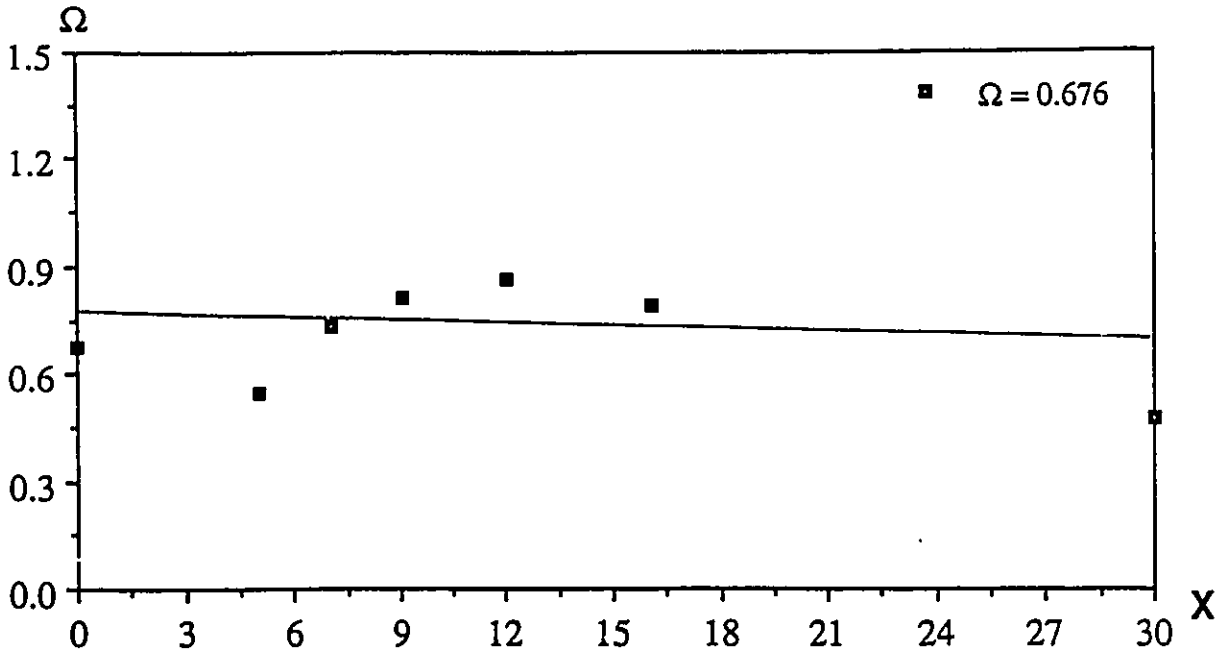

Figure 5.39: Ω vs. X for $r_2/r_1 = 2.0$, $\Omega = 0.676$

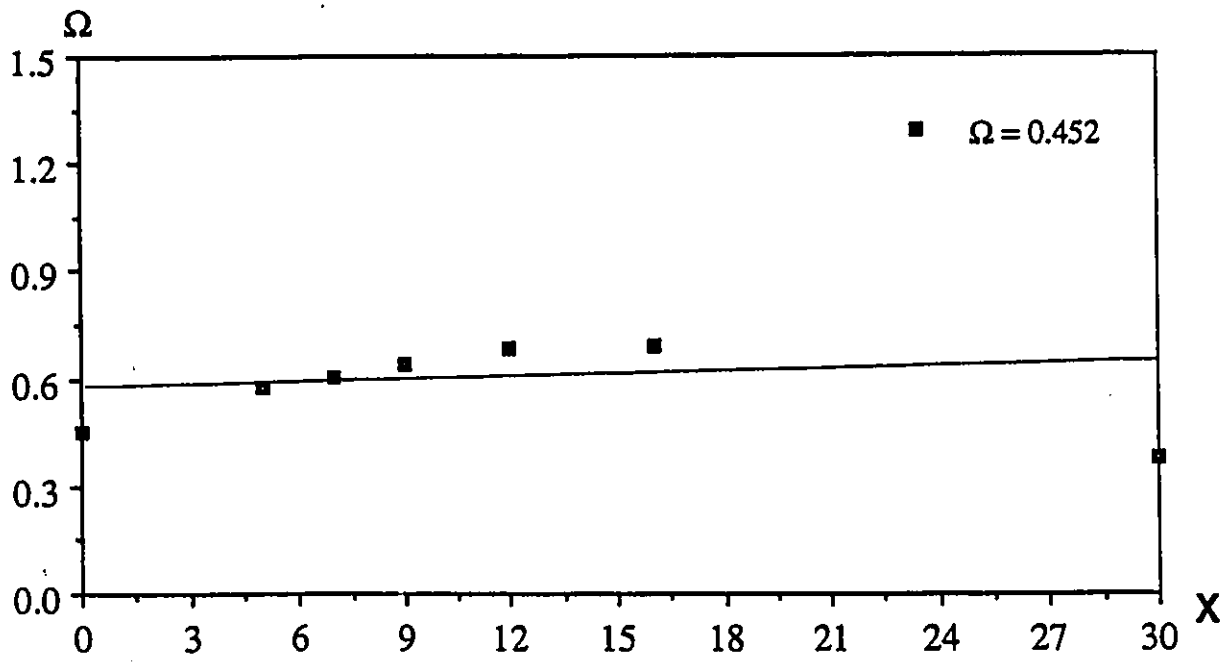

Figure 5.40: Ω vs. X for $r_2/r_1 = 2.0$, $\Omega = 0.452$

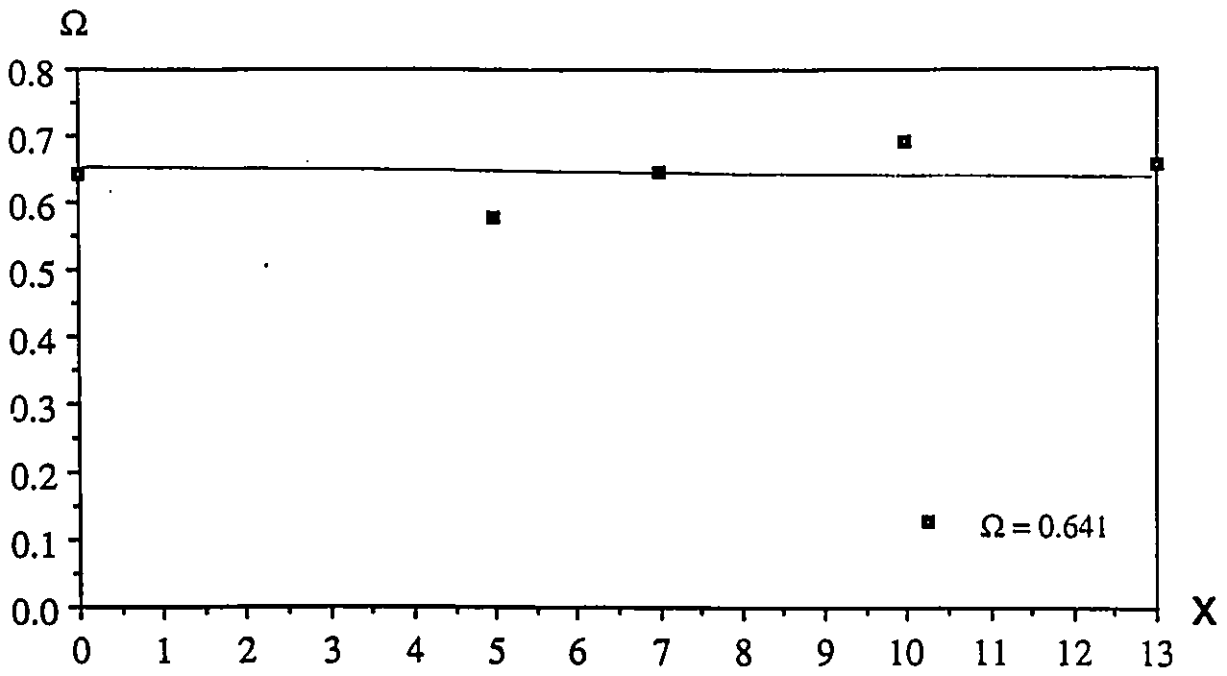

Figure 5.41: Ω vs. X for $r_2/r_1 = 1.625$, $\Omega = 0.641$

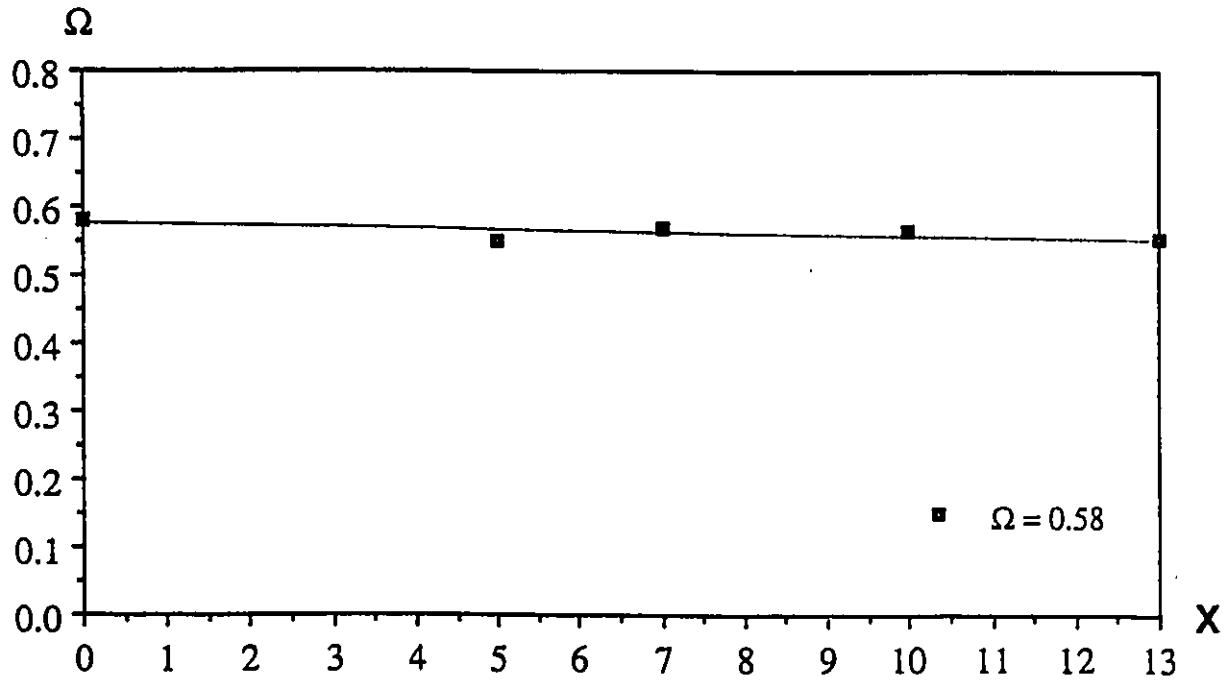

Figure 5.42: Ω vs. X for $r_2/r_1 = 1.625$, $\Omega = 0.58$

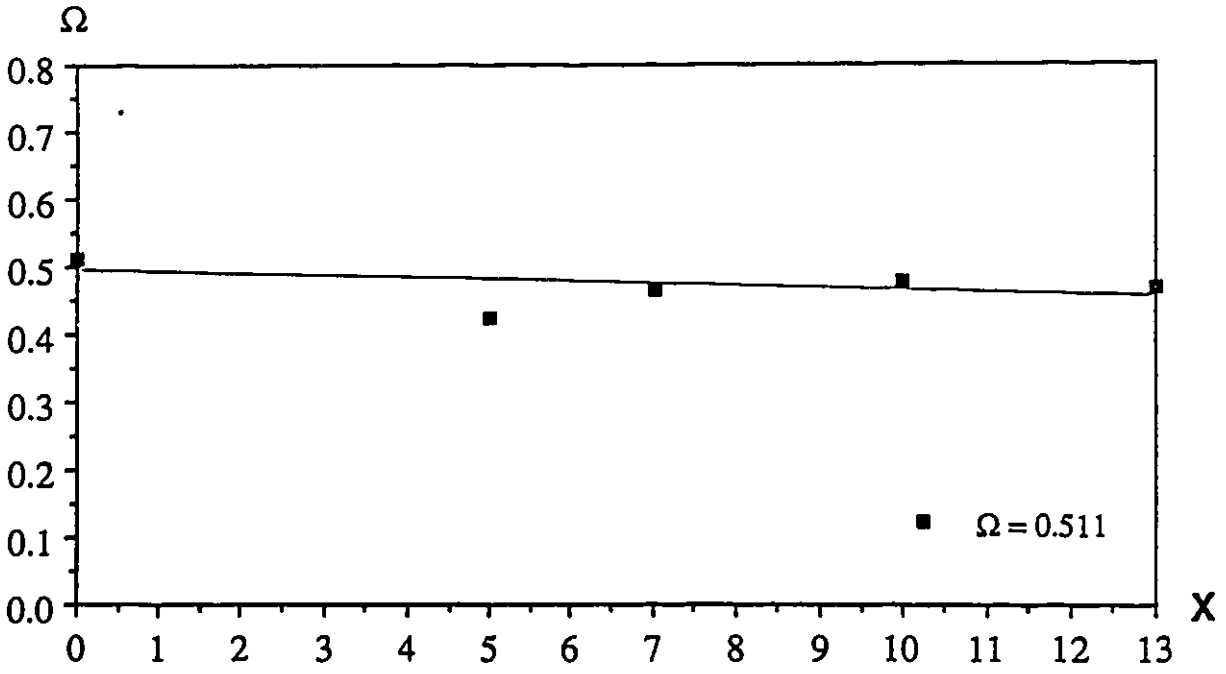

Figure 5.43: Ω vs. X for $r_2/r_1 = 1.625$, $\Omega = 0.511$

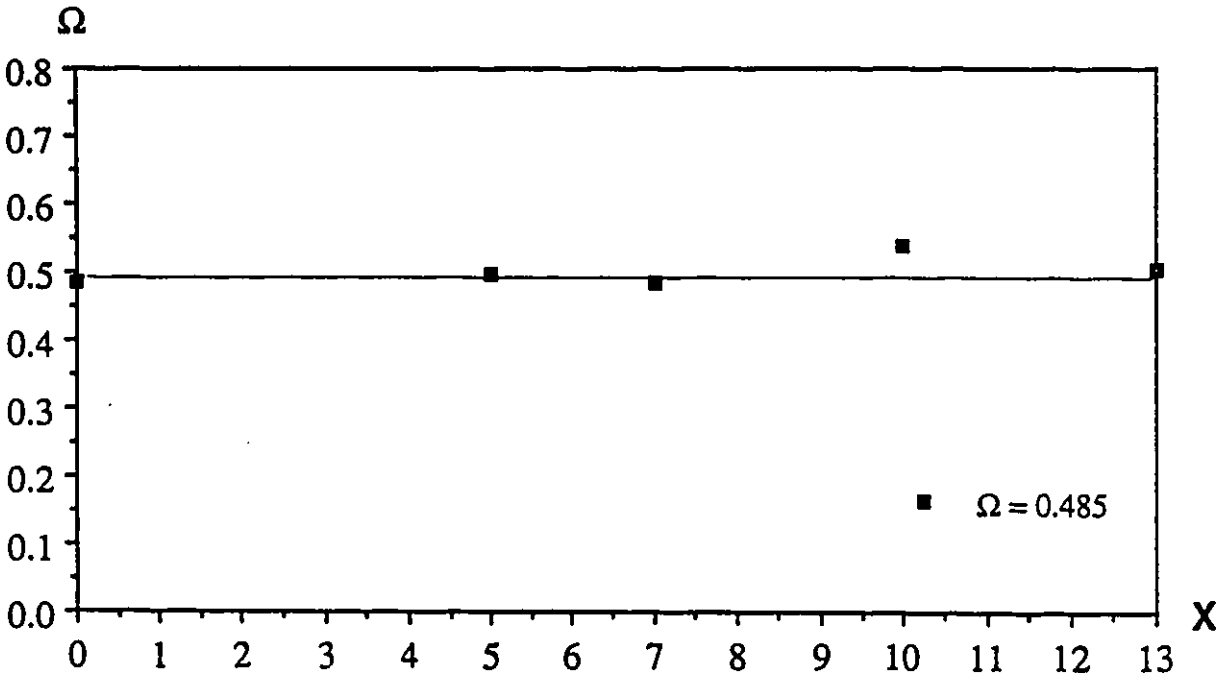

Figure 5.44: Ω vs. X for $r_2/r_1 = 1.625$, $\Omega = 0.485$

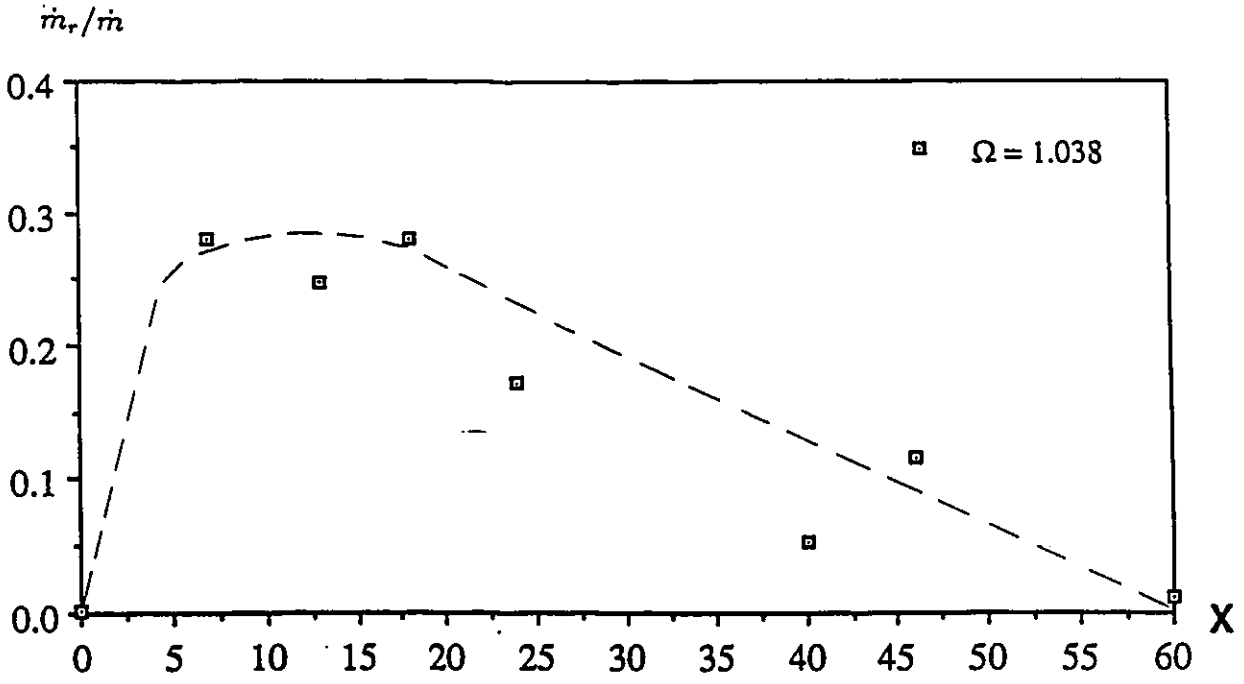

Figure 5.45: $\dot{m}_r/\dot{m}$ vs. X for $r_2/r_1 = 2.813$, $\Omega = 1.038$

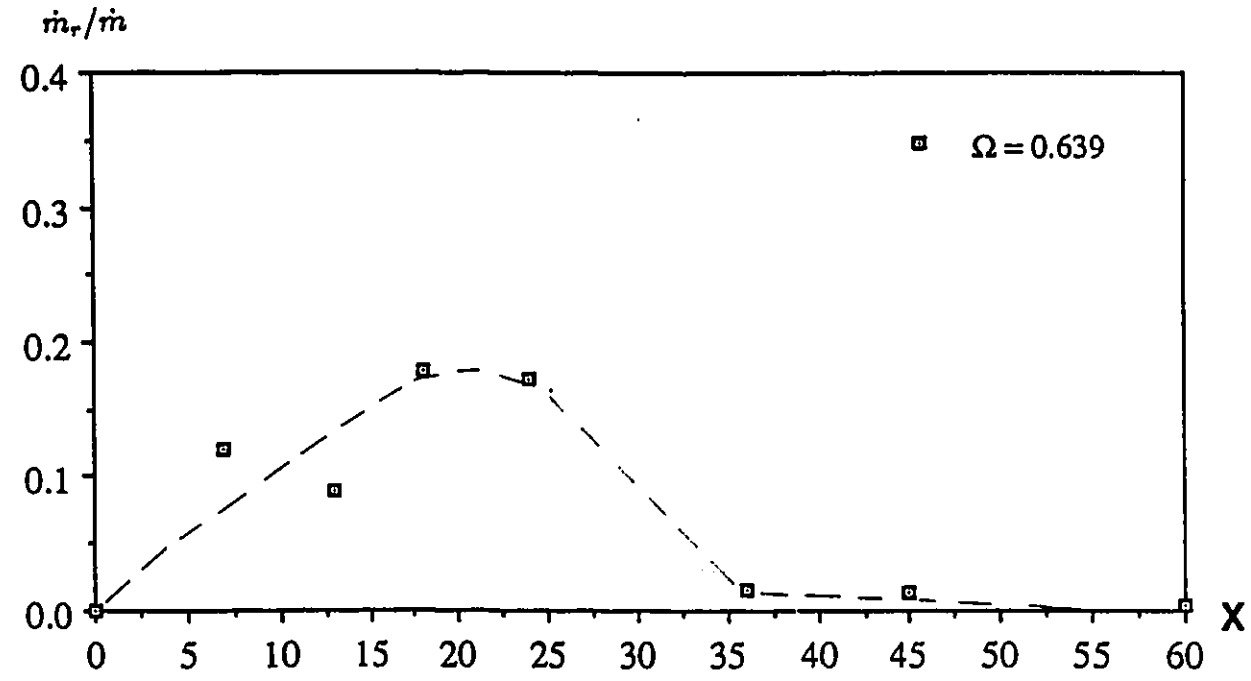

Figure 5.46: $\dot{m}_r/\dot{m}$ vs. X for $r_2/r_1 = 2.813$, $\Omega = 0.639$

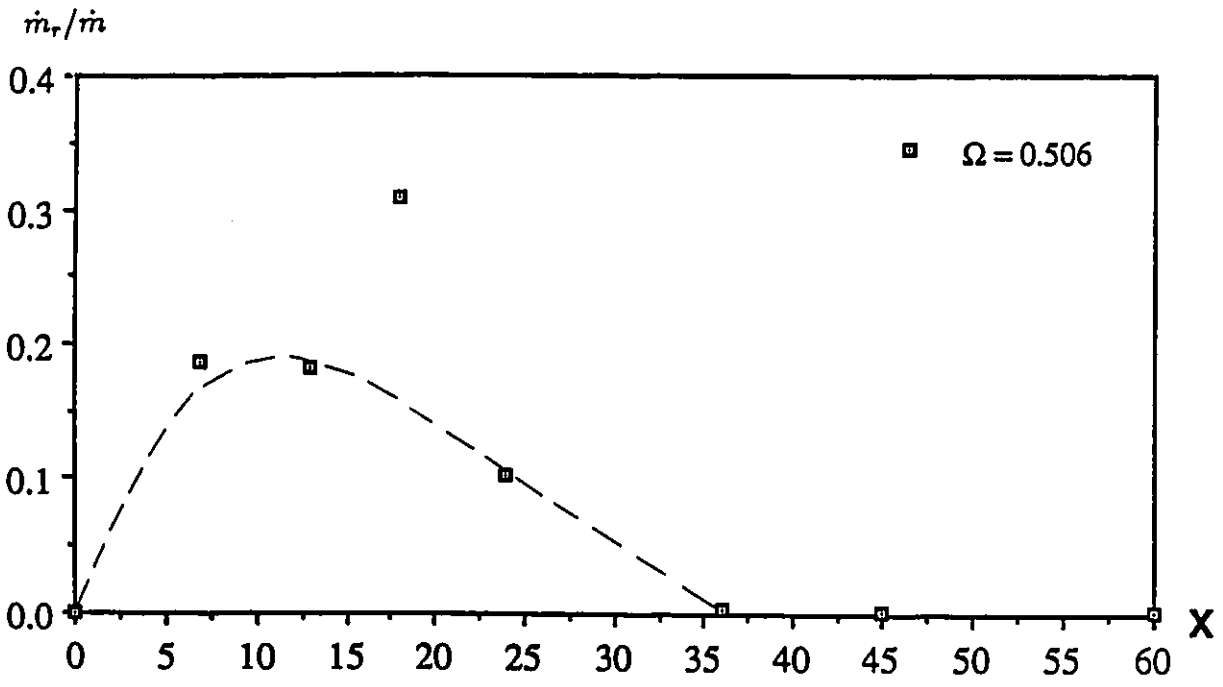

Figure 5.47: $\dot{m}_r/\dot{m}$ vs. X for $r_2/r_1 = 2.813$, $\Omega = 0.506$

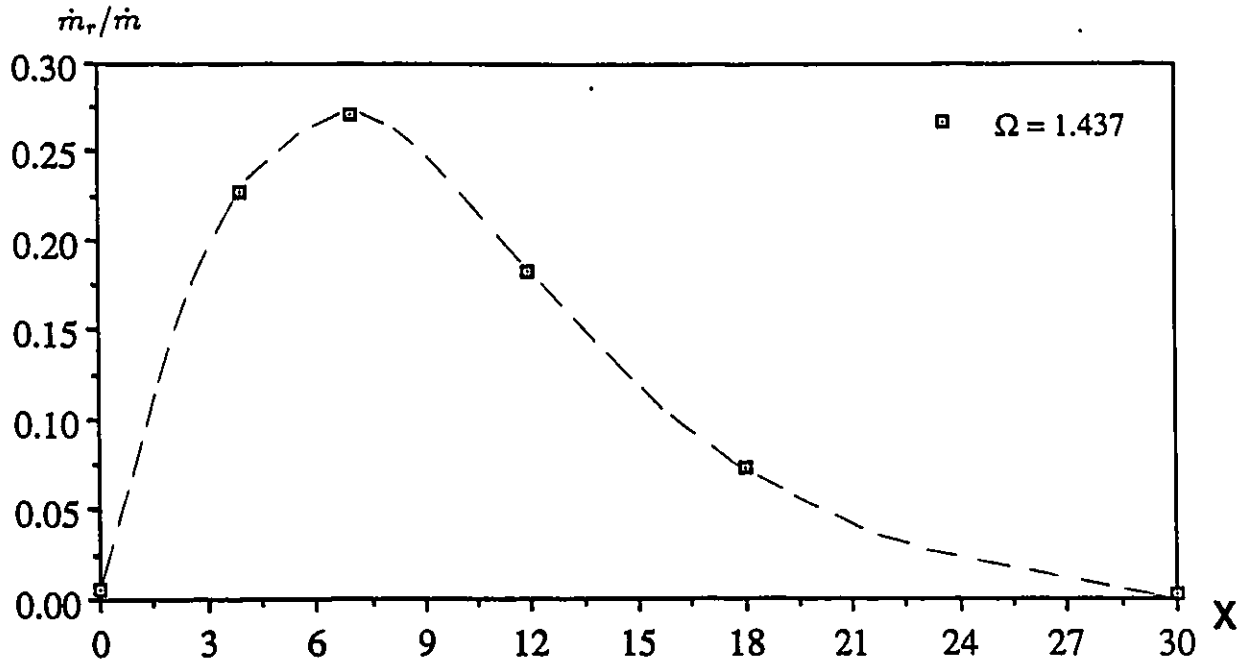

Figure 5.48: $\dot{m}_r/\dot{m}$ vs. X for $r_2/r_1 = 2.0$, $\Omega = 1.437$

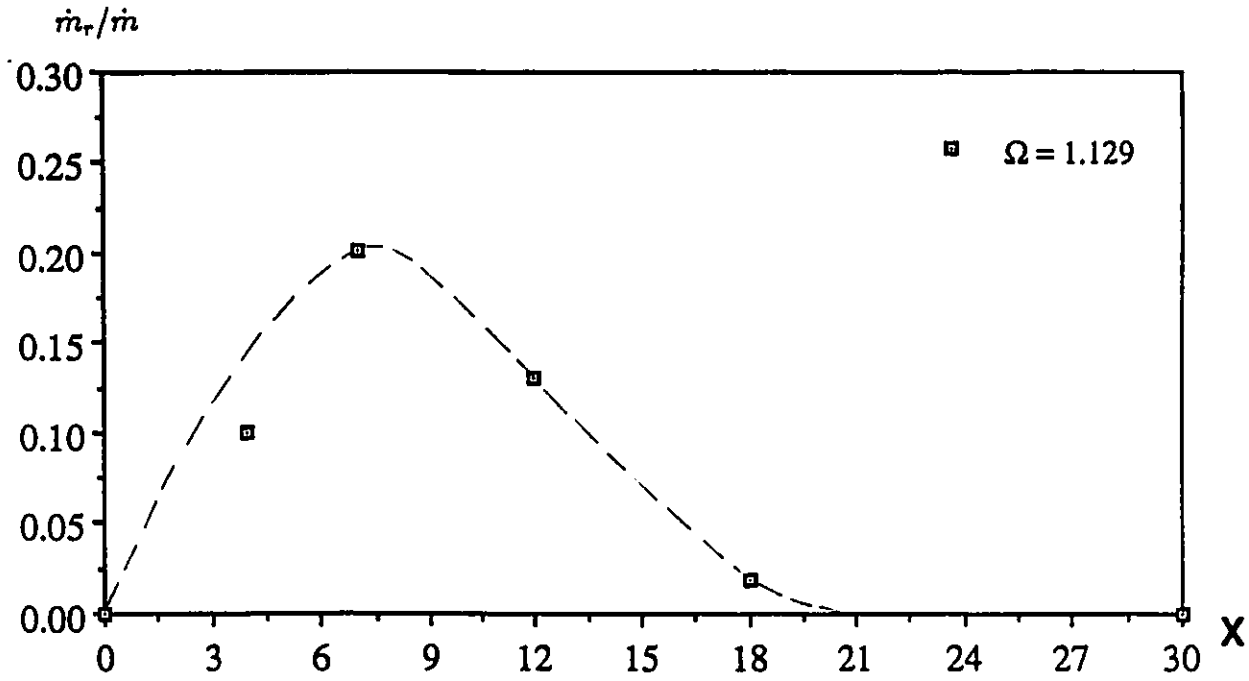

Figure 5.49: $\dot{m}_r/\dot{m}$ vs. X for $r_2/r_1 = 2.0$. $\Omega = 1.129$

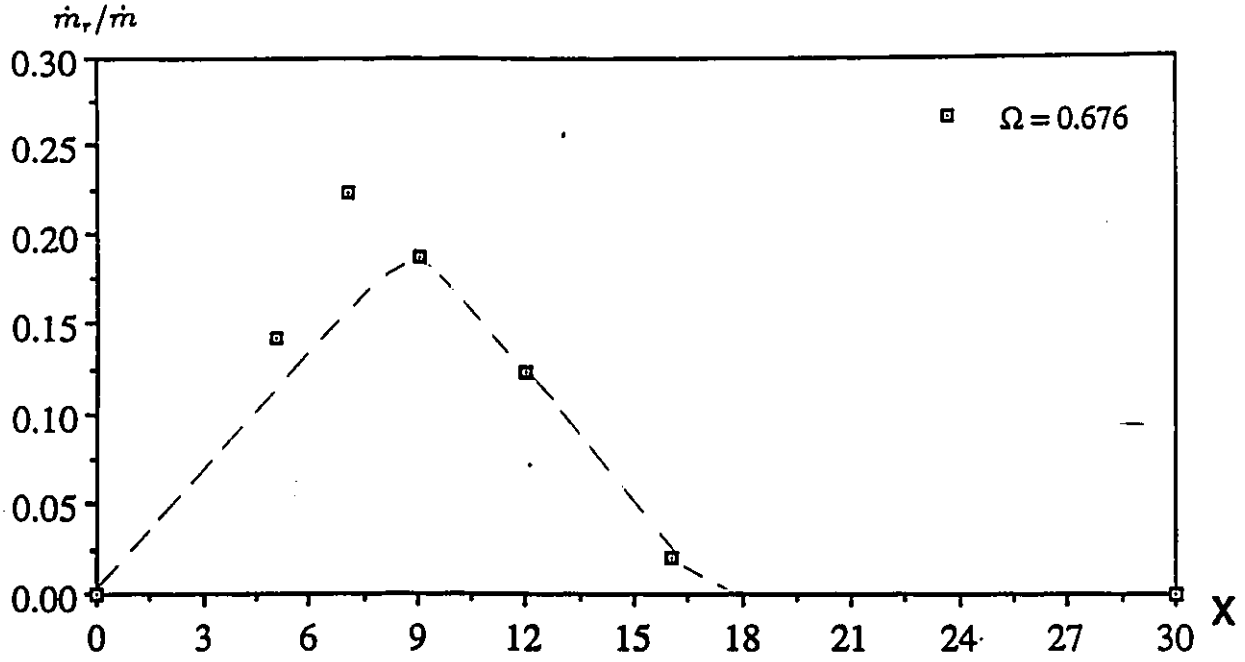

Figure 5.50: $\dot{m}_r/\dot{m}$ vs. X for $r_2/r_1 = 2.0$, $\Omega = 0.676$

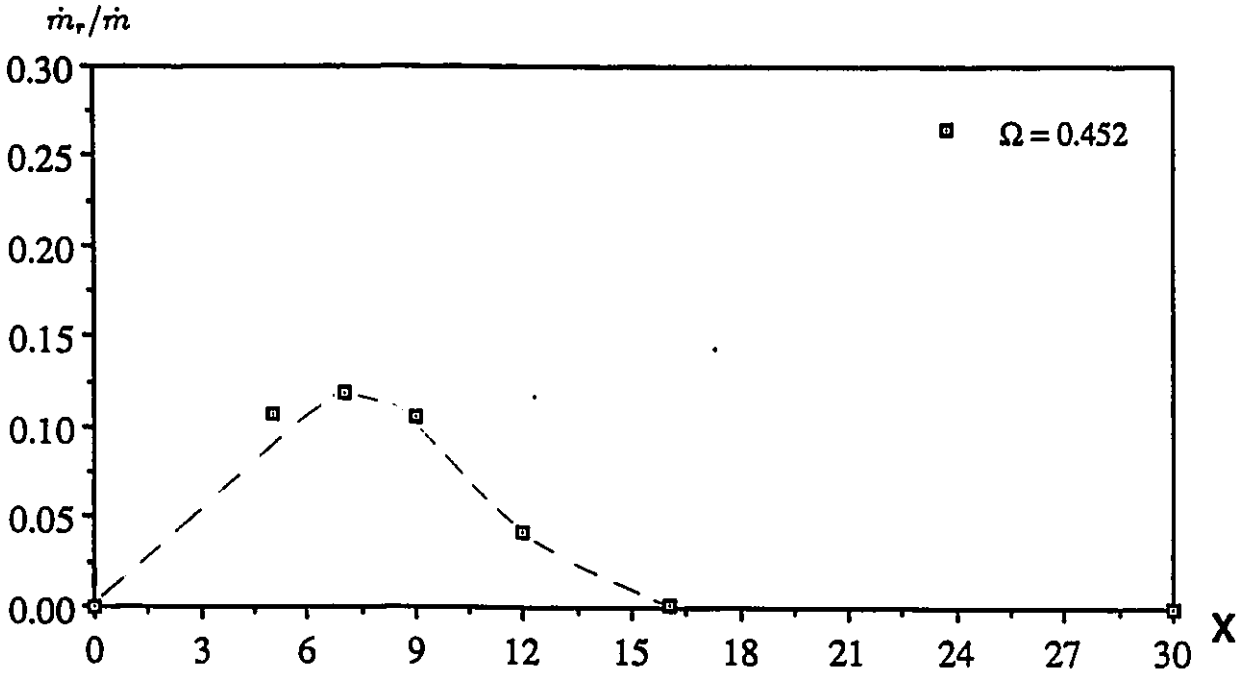

Figure 5.51: $\dot{m}_r/\dot{m}$ vs. X for $r_2/r_1 = 2.0$, $\Omega = 0.452$

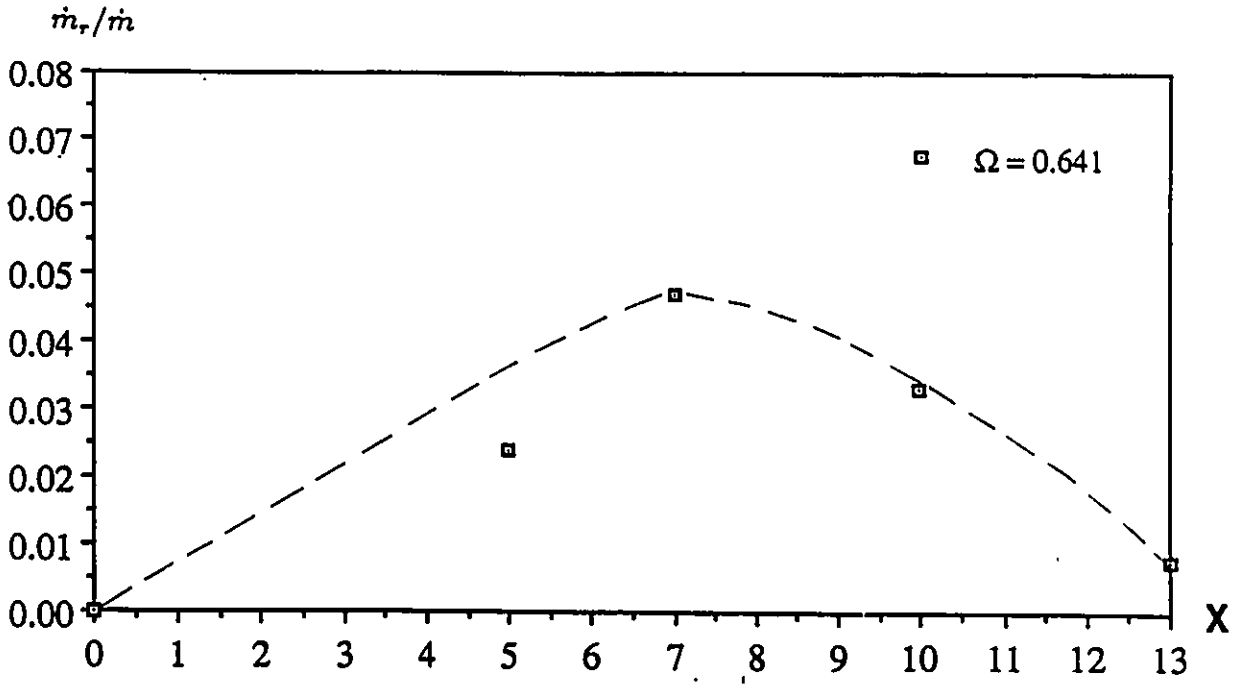

Figure 5.52: $\dot{m}_r/\dot{m}$ vs. X for $r_2/r_1 = 1.625$, $\Omega = 0.641$

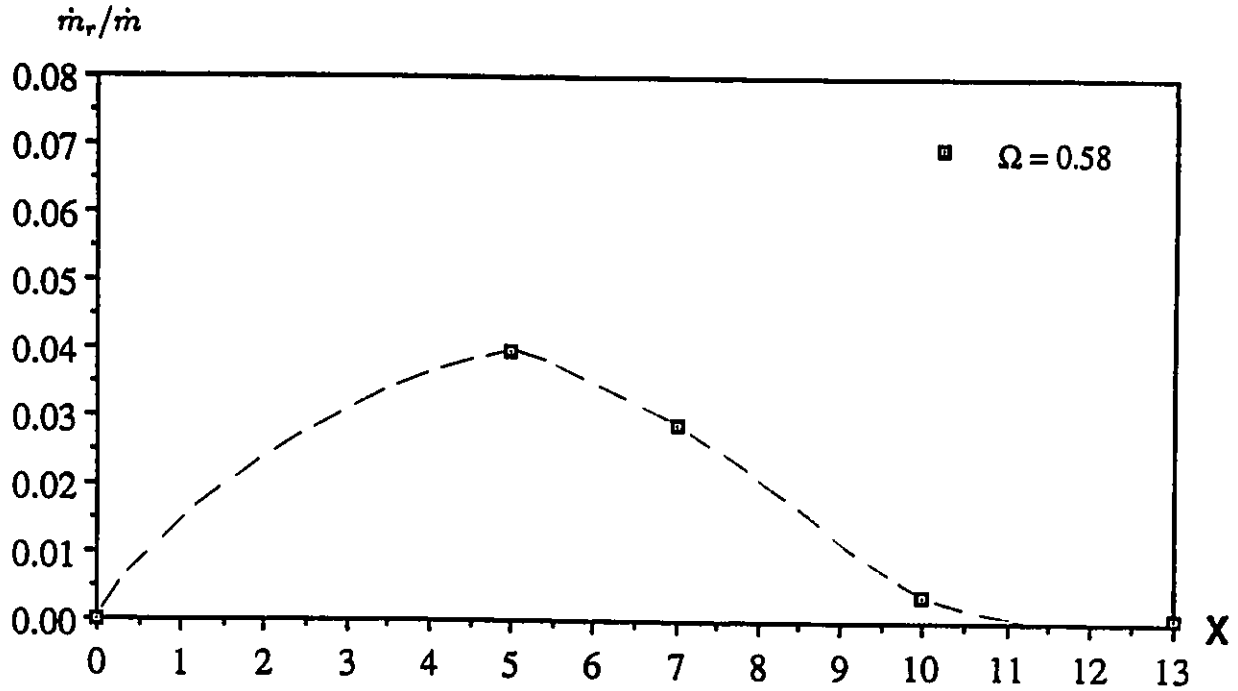

Figure 5.53: $\dot{m}_r/\dot{m}$ vs. X for $r_2/r_1 = 1.625$, $\Omega = 0.58$

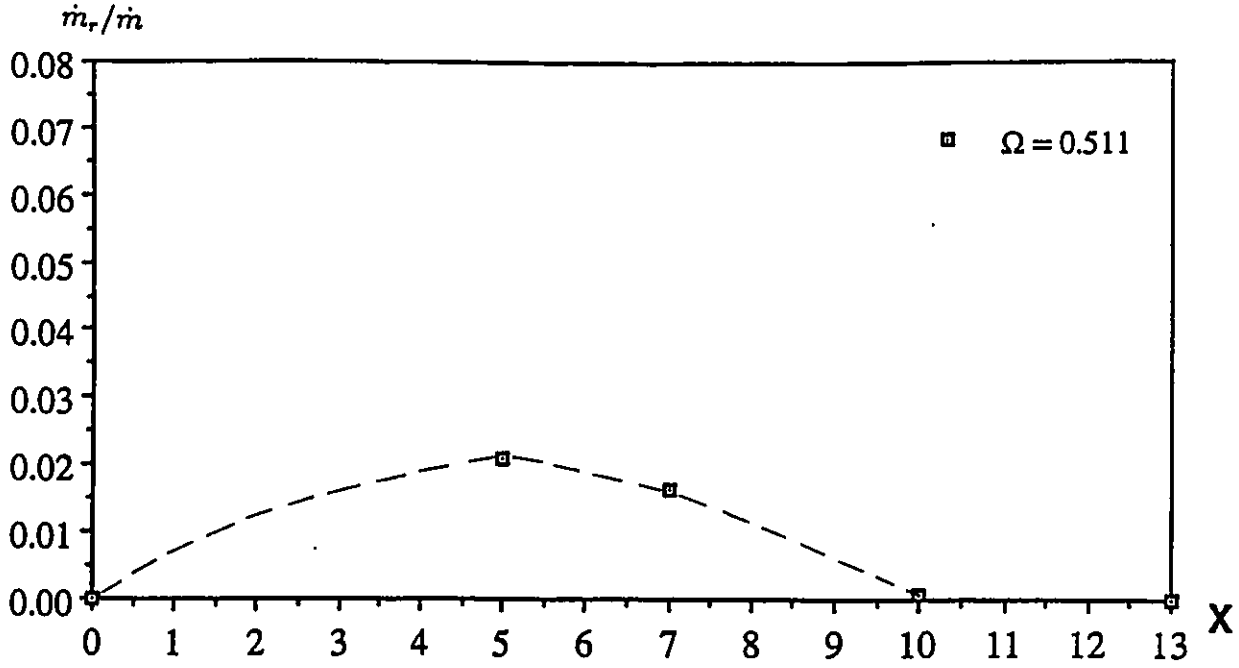

Figure 5.54: $\dot{m}_r/\dot{m}$ vs. X for $r_2/r_1 = 1.625$, $\Omega = 0.511$

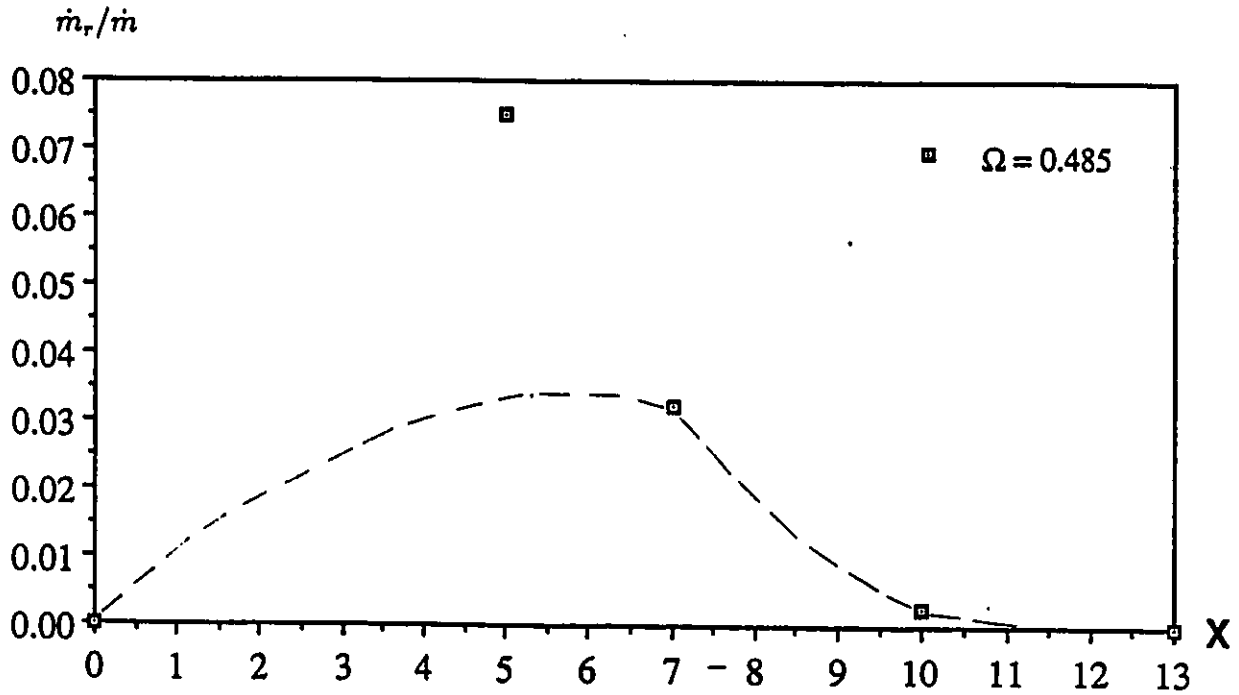

Figure 5.55: $\dot{m}_r/\dot{m}$ vs. X for $r_2/r_1 = 1.625$, $\Omega = 0.485$

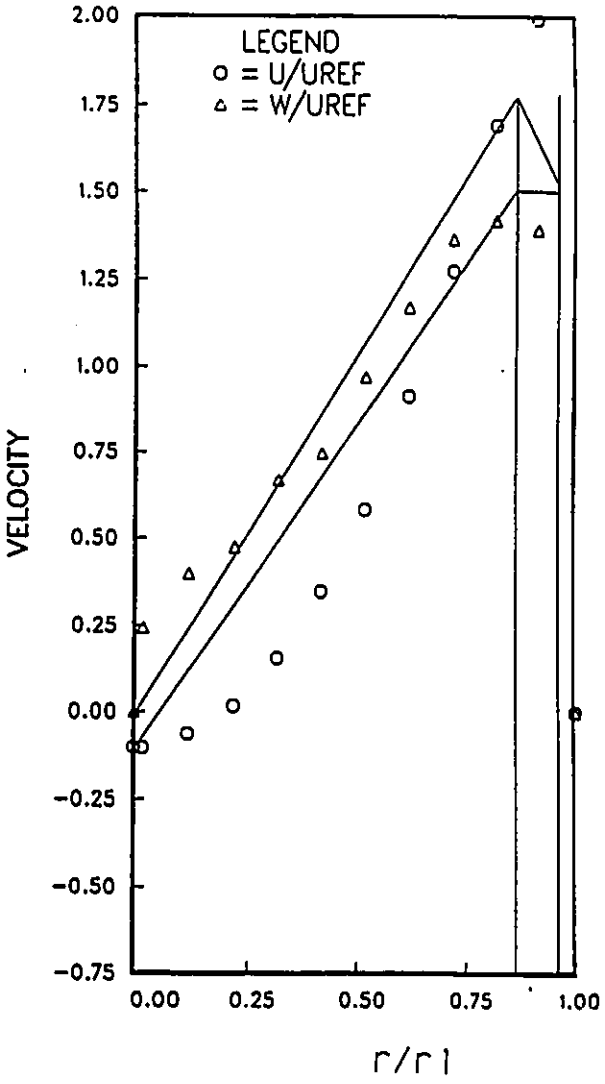

Figure 5.56: Fitted Inlet Velocity Profiles for $r_2/r_1 = 2.813, \Omega = 1.038$

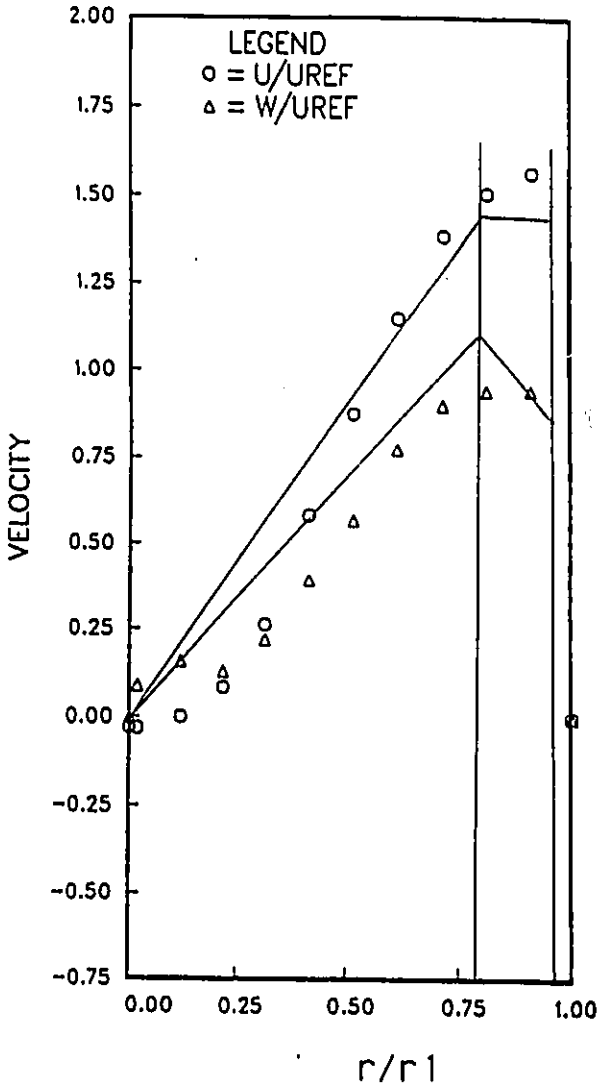

Figure 5.57: Fitted Inlet Velocity Profiles for $r_2/r_1 = 2.813, \Omega = 0.639$

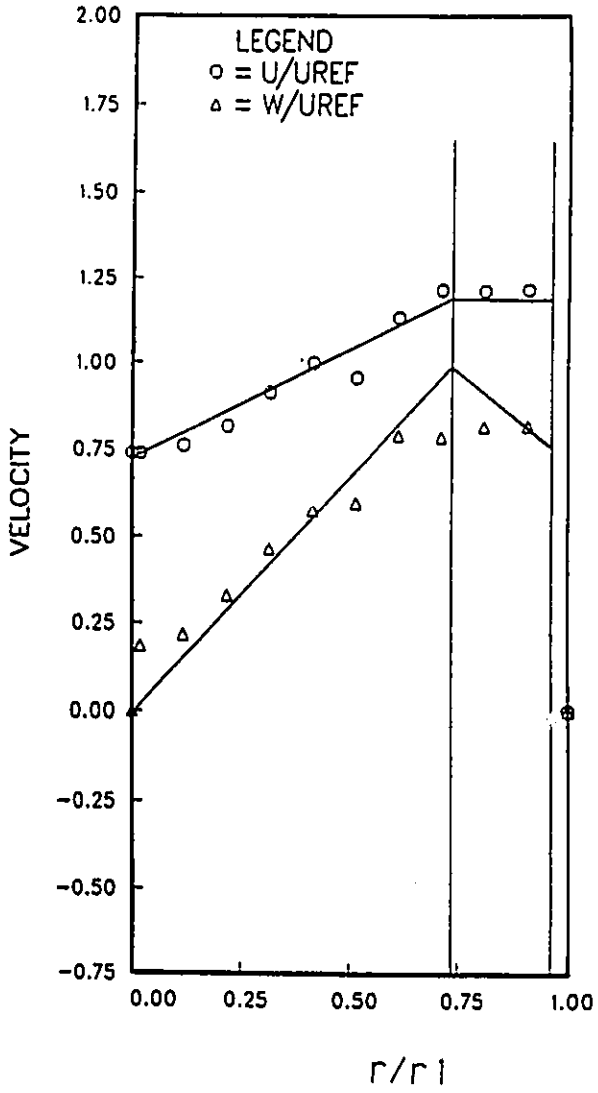

Figure 5.58: Fitted Inlet Velocity Profiles for $r_2/r_1 = 2.813$, $\Omega = 0.506$

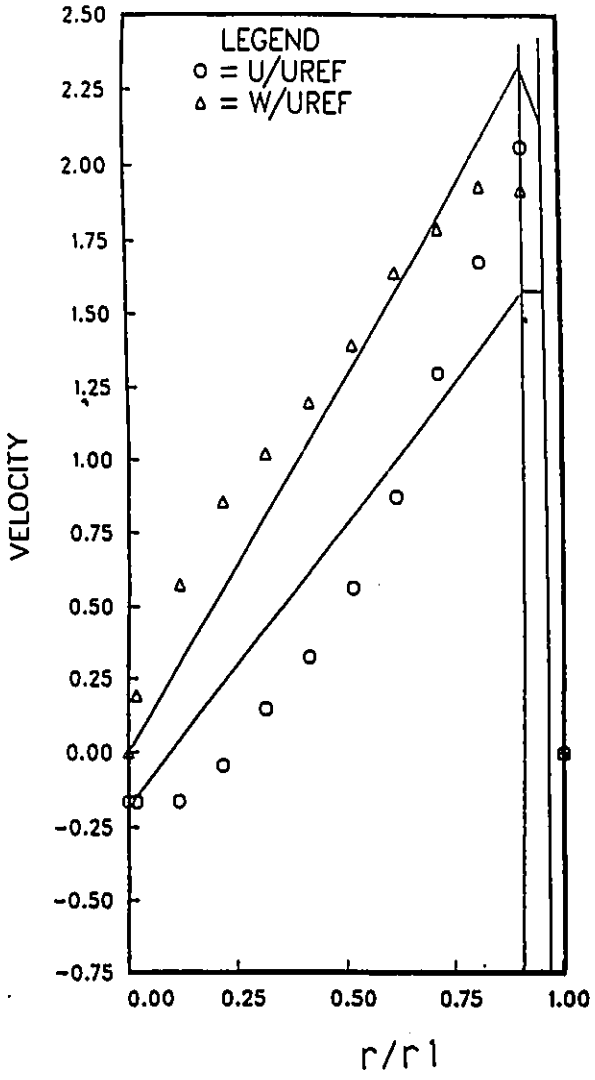

Figure 5.59: Fitted Inlet Velocity Profiles for $r_2/r_1 = 2.0$, $\Omega = 1.437$

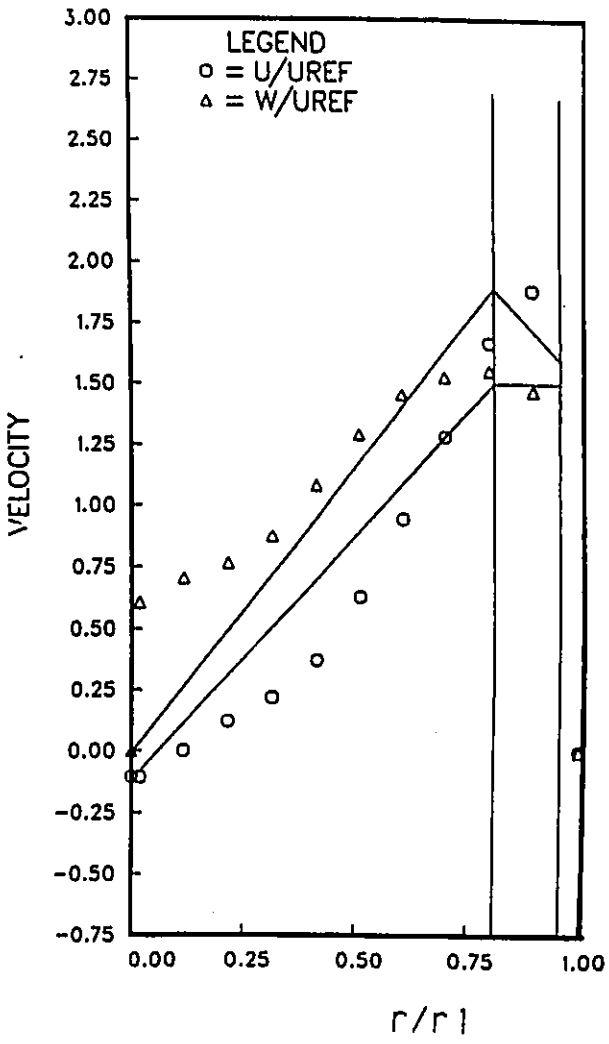

Figure 5.60: Fitted Inlet Velocity Profiles for $r_2/r_1 = 2.0$, $\Omega = 1.129$

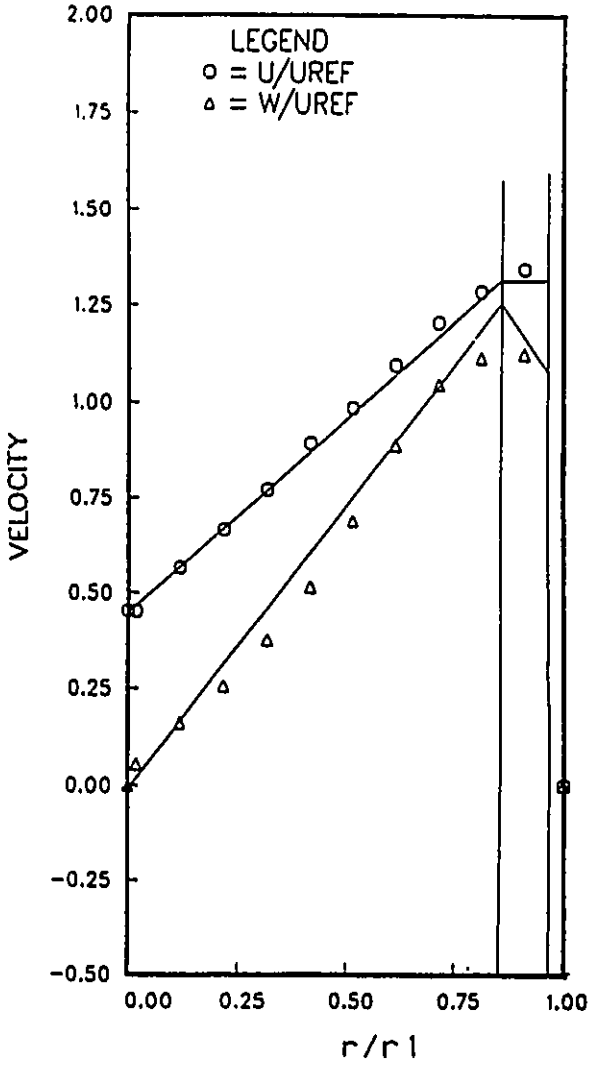

Figure 5.61: Fitted Inlet Velocity Profiles for $r_2/r_1 = 2.0$, $\Omega = 0.676$

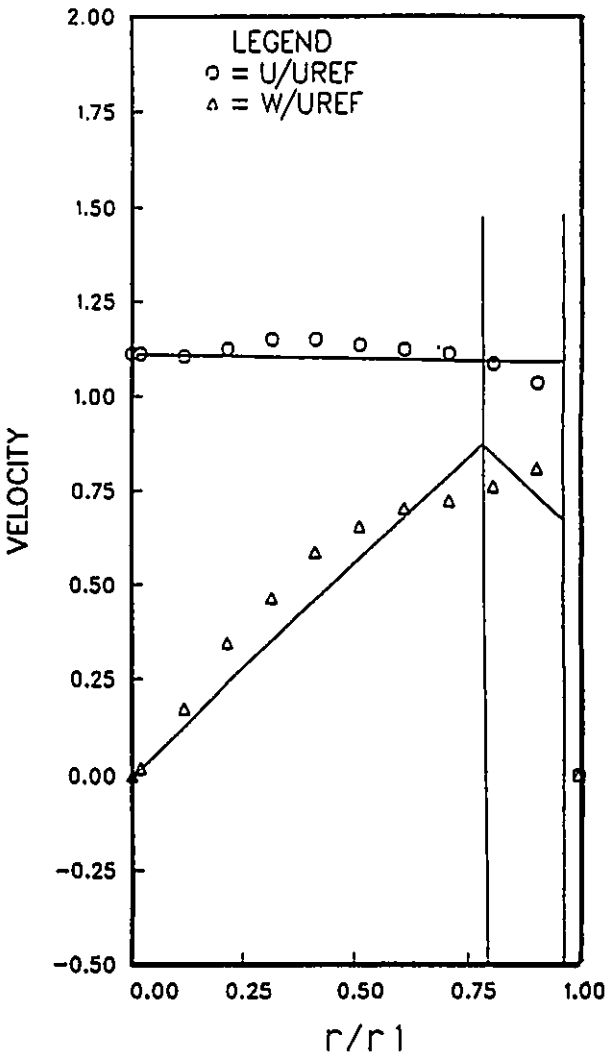

Figure 5.62: Fitted Inlet Velocity Profiles for $r_2/r_1 = 2.0$, $\Omega = 0.452$

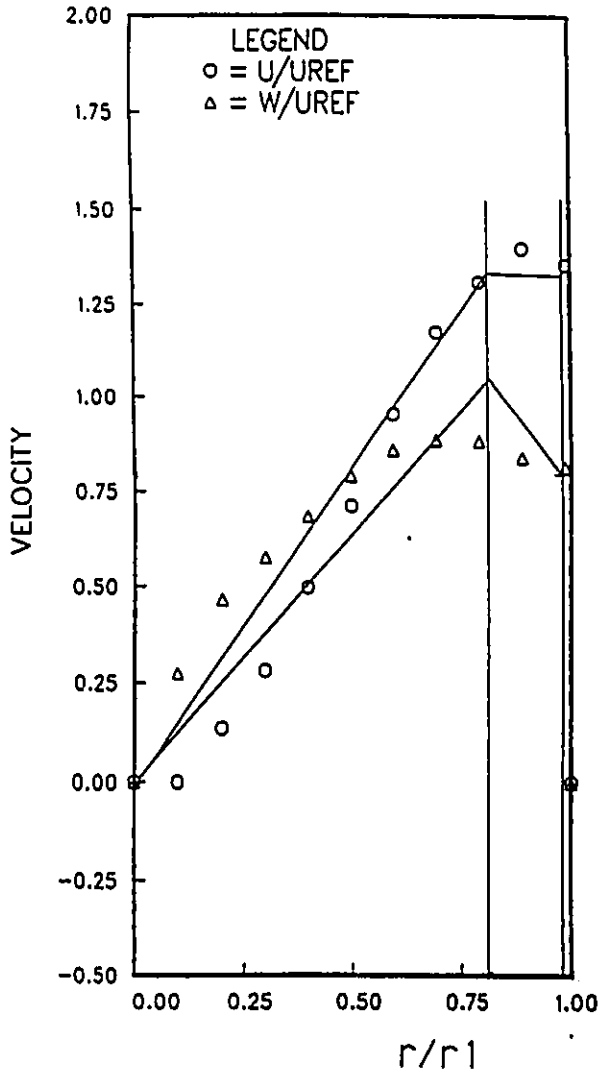

Figure 5.63: Fitted Inlet Velocity Profiles for $r_2/r_1 = 1.625$, $\Omega = 0.641$

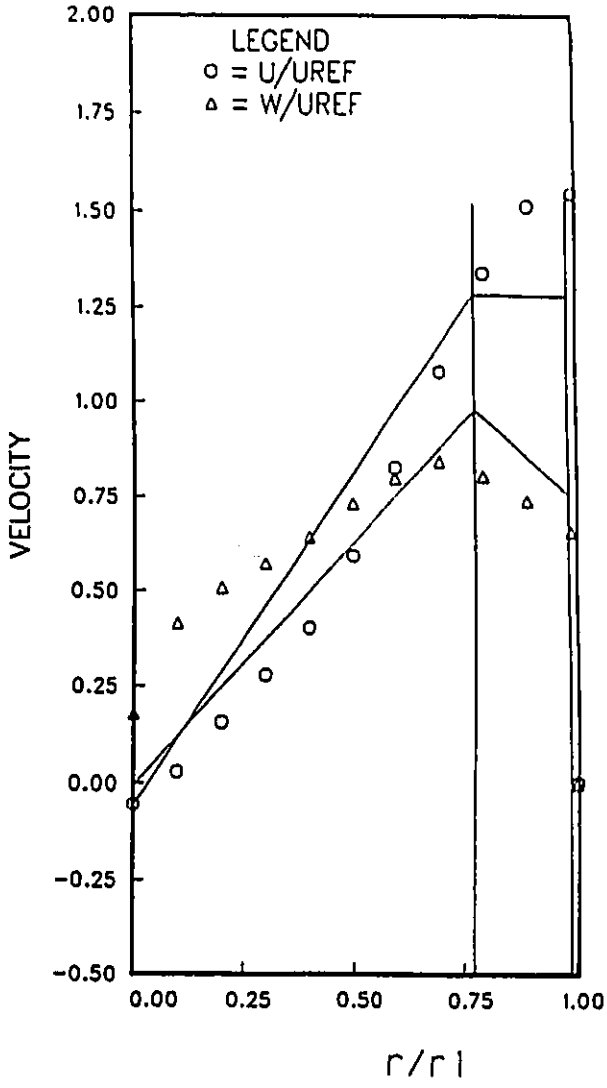

Figure 5.64: Fitted Inlet Velocity Profiles for $r_2/r_1 = 1.625$, $\Omega = 0.58$

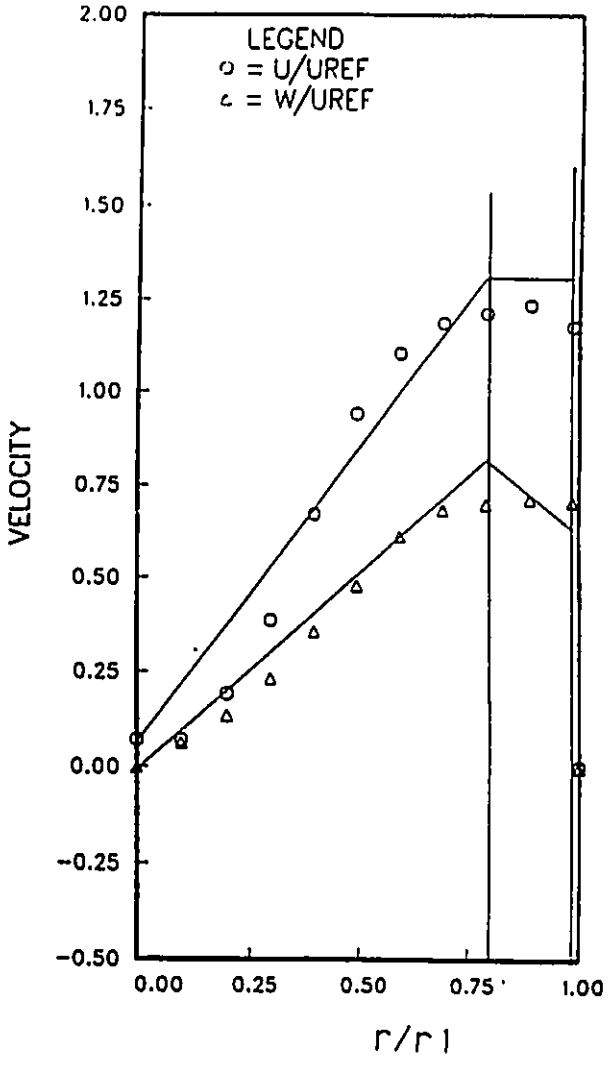

Figure 5.65: Fitted Inlet Velocity Profiles for $r_2/r_1 = 1.625$, $\Omega = 0.511$

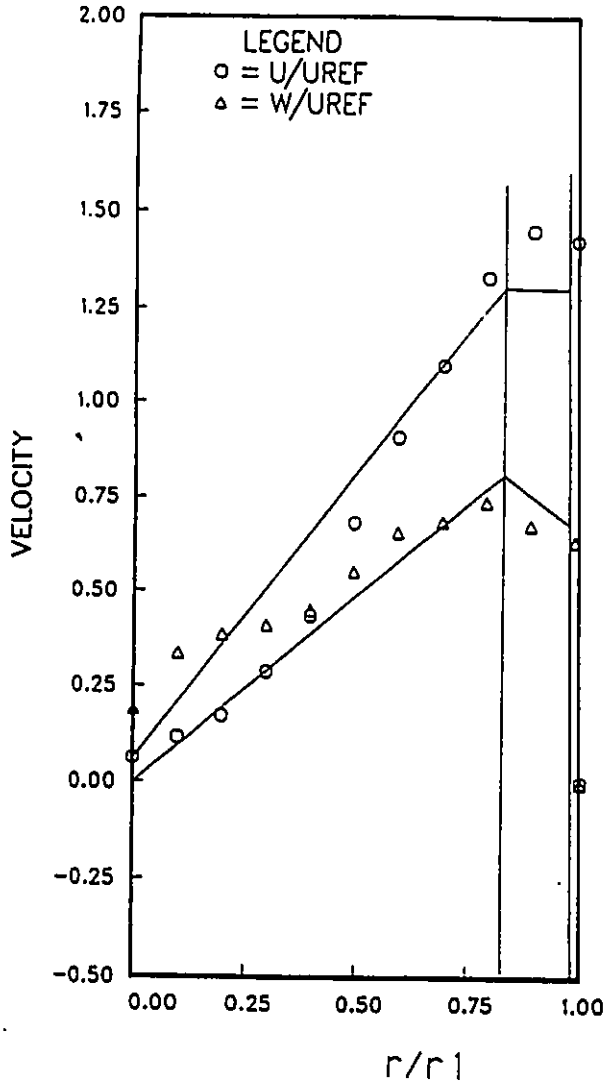

Figure 5.66: Fitted inlet velocity profiles for $r_2/r_1 = 1.625$. $\Omega = 0.485$

r_2/r_1	Ω	λ	Γ_1	a_1/r_1	$u_1/\bar{u}_{ref}$	$w_1/\bar{u}_{ref}@a_1$	$w_1/\bar{u}_{ref}@r_\beta$
2.813	1.038	-0.069	66.621	0.854	1.492	1.782	1.522
2.813	0.639	-0.002	38.428	0.778	1.384	1.128	0.878
2.813	0.506	0.621	32.423	0.745	1.187	0.994	0.741
2.000	1.437	-0.107	93.008	0.911	1.592	2.332	2.125
2.000	1.129	-0.072	72.317	0.852	1.492	1.938	1.652
2.000	0.676	0.344	46.726	0.854	1.314	1.251	1.067
2.000	0.452	1.010	30.550	0.798	1.102	0.874	0.698
1.625	0.641	-0.104	41.189	0.819	1.349	1.014	0.830
1.625	0.580	-0.002	37.367	0.776	1.272	0.971	0.753
1.625	0.511	0.048	33.824	0.831	1.301	0.820	0.682
1.625	0.485	0.050	31.656	0.806	1.279	0.792	0.638

Table 5.1: Fitted Inlet Velocity Profile Parameters.

r_2/r_1	Ω	$\dot{m}_r/\dot{m}$ (model)	$\dot{m}_r/\dot{m}$ (exp)	$u_{02}/\bar{u}_{ref}$ (model)	$u_{02}/\bar{u}_{ref}$ (exp)	r_c/r_2 (model)	r_c/r_2 (exp)
2.813	1.038	0.42	0.28	0.30	0.35	0.59	0.57
2.813	0.639	0.24	0.18	0.20	0.15	0.55	0.53
2.813	0.506	0.16	0.18	0.15	0.24	0.52	0.46
2.000	1.437	0.21	0.27	0.36	0.54	0.54	0.45
2.000	1.129	0.16	0.20	0.29	0.41	0.52	0.40
2.000	0.676	0.08	0.18	0.19	0.23	0.46	0.45
2.000	0.452	0.011	0.12	0.06	0.14	0.31	0.40
1.625	0.641	0.033	0.05	0.17	0.16	0.39	0.42
1.625	0.580	0.032	0.04	0.16	0.15	0.387	0.36
1.625	0.511	0.027	0.02	0.15	0.13	0.37	0.30
1.625	0.485	0.026	0.02	0.14	0.22	0.369	0.36

Table 5.2: Comparison of Analytical Results with Experimental Results at $\kappa = 1.0$.

Chapter 6

Conclusions

The structure of the central recirculation zone in enclosed swirling flow has been studied. Experiments were conducted to measure the central recirculation zones in a sudden expansion. A simple mathematical model was established to predict the flow in a sudden expansion. Comparisons were made to evaluate the model by using some examples.

For non-reacting swirling flow issuing into an axi-symmetric sudden expansion, experiments show that the back flow velocities increase with the swirl intensities and the expansion ratios. This results in the size of the recirculation zone increasing with the swirl intensity (Ω) and the expansion ratio. However, the diameter of the recirculation zone does not change greatly with Ω, and it increases proportional to the expansion ratio. Accordingly, the recirculating mass flow also increases with Ω.

The model used the three integral equations with assumed velocity profiles to predict the recirculating mass flow, back flow velocity and radius of back flow zone. To evaluate the model, the fitted velocity profiles based on the measured inlet velocity profiles were employed to compare to the experimental results. The overall average error between the comparisons is 22%. Considering the simplicity of the model this agreement is satisfactory. The Reynolds number is in the fully turbulent range, approximately equal to 10^6.

If the shear coefficient κ is allowed to take different values for different expansion ratios, the agreement between the model and experimental results will be better. Thus, the relationships between them need to be explored. Also flows with hub and with combustion could become the future work.

List of References

[1] V.N. Afrosimova, "Study of the Aerodynamics of a Furnace Space," *Thermal Engineering, (USSR)* Vol. 14, pp. 10–15, 1967.

[2] B.J. Baker, P. Hutchinson, E.E. Khalil and J.H. Whitelaw, "Measurements of Three Velocity Components in a Model Furnace With and Without Combustion," *15th Symposium (International) Combustion,* pp. 553–559, 1974.

[3] S.A. Beltagui and N.R.L. Maccallum, "Aerodynamics of Vane-Swirled Flames Expension in Furnaces," *Journal of the Institute of Fuel,* Vol. 49, pp. 183–193, 1976.

[4] H.H. Bossel, "Swirling Flows in Streamtubes of Variable Cross-section," *AIAA Journal,* Vol. 11, pp. 1161–1165, 1973.

[5] R.D. Brum, G.S. Samuelsen "Two-Component Laser Anemometry Measurements of Non-Reacting and Reacting Complex Flows in A Swirl-Stabilized Model Combustor," *Experiments in Fluids,*Vol. 5, pp. 95–102, 1987.

[6] D.W. Bryer and R.C. Pankhurst, **Pressure-probe Methods for Determining Wind Speed and Flow Direction**, Her Majesty's Stationery Office, London, 1971.

[7] M. Chattree, I. Celik, and S. Singh, "Analysis of Turbulent Swirling Flow in a Model Combustor," *ASME Fluids Engineering Division, Industrial Application of Fluid Mechanics,* Vol. 54, pp. 41–45, 1987.

[8] C.Y. Chow, "Swirling Flow in Tubes of Non-uniform Cross-sections," *Journal of Fluid Mechanics,* Vol. 38, Part 4, pp. 843–854, 1969.

[9] T.F. Dixon, J.S. Truelove, and T.F. Wall, "Aerodynamic Studies on Swirled Coaxial Jets from Nozzles with Divergent Quarl," *Journal of Fluids Engineering,* Vol. 105, pp. 197–203, 1983.

[10] V.M. Domkundwar, V. Sriramulu, and M.C. Gupta, "Analysis of Swirling Recirculating Reacting Turbulent Jets Passing through Diffusers," *Combustion and Flame,*Vol. 33, pp. 241–249, 1978.

[11] M.P. Escudier and J.J. Keller, "Vortex Breakdown: A Two-Stage Transition", *AGARD Conference Proceedings on Aerodynamics of Vortical Type Flows in Three Dimensions*, No. 342, pp. 25-1-25-8, Rotterdam, 1983.

[12] J.H. Faler and S. Leibovich, "Disrupted States of Vortex Flow and Vortex Breakdown," *The Physics of Fluids,* Vol. 20, No. 9, pp. 1385–1399, 1977.

[13] T.M. Farag, M. Shimizu, M.Arai and H.Hiroyasu, "Flow Measurement in a Swirl Combustor in Two Case of With and Without Combustion," *Bulletin of JSME,*Vol. 27, No. 25, pp. 521–528, 1984.

[14] I.Glassman, **Combustion**, Academic Press 1987

[15] F.C. Gouldin, "Probe Measurements in Multi-Dimensional Reacting Flows," *AGARD Conference Proceeding on Testing and Measurements Techniques in Heat Transfer and Combustion,* Brussels, 1980

[16] W.L.H. Hallett and R. Günther, "Flow and Mixing in Swirling Flow in a Sudden expansion", *The Canadian Journal of Chemical Engineering,* Vol. 62, pp. 149–155, 1984.

[17] W.L.H. Hallett, "A Swirl Generator for Independent Variation of Swirl Parameter and Velocity Profile Shape", *AIAA Journal,* Vol. 24, No. 7, pp 1212–1213,1986.

[18] W.L.H. Hallett and D.J. Toews, "The Effect of Inlet Conditions and Expansion Ratio on the Onset of the Reversal in Swirling Flow in a Sudden Expansion", *Experiments in Fluids*, Vol. 5, pp. 129–133, 1987.

[19] W.L.H. Hallett, "A Simple Model for the Critical Swirl in a Swirling Sudden Expansion Flow" *Journal of Fluids Engineering*, Vol. 110, pp. 155–160, June 1988.

[20] W.L.H. Hallett and V. Tavasoli, "The Effect of a Central Hub on Critical Swirl in a Swirling Sudden-Expansion Flow", *Journal of the Institute of Energy*, Vol. 64, pp. 82–88, June 1991.

[21] K.H.Khalil, F.M. El-Mahallawy and H.A. Moneib, "Effect of Combustion Air Swirl on the Flow Pattern in a Cylindrical Oil Fired Furnace," *16th Symposium (International) Combustion*, pp. 135–143,1976.

[22] E.Krause, "A Contribution to the Problem of Vortex Breakdown", *AGARD Conference Proceedings on Aerodynamics of Vortical Type Flow in Three Dimensions*, No.324, pp. 26-1-26-4, Rotterdam, 1983.

[23] I. Kubo and F.C. Gouldin, "Numerical Calculations of Turbulent Swirling Flow," *ASME Journal of Fluids Engineering*, Vol. 97, pp. 310–315, 1975.

[24] A.Mager "Incompressible, Viscous, Swirling Flow Through a Nozzle," *AIAA Journal*,Vol. 9. No.4 pp. 649–654, 1971.

[25] A.Mager "Dissipation and Breakdown of a Wing-Tip Vortex," *Journal of Fluid Mechanics*,Vol. 55. Part 4, pp.609–628, 1972.

[26] T. Mahmud, J.S. Truelove, and T.F. Wall, "Flow Characteristics of Swirling Coaxial Jets from Divergent Nozzles", *ASME Journal of Fluids Engineering*, Vol. 109. pp. 275–282, 1987

[27] M.L. Mathur and N.R.L. Maccallum, "Swirling Air Jets Issuing From Vane Swirlers. Part 2: Enclosed Jets", *Journal of the Institute of Fuel*, Vol. 40, pp. 238–245, 1967.

[28] P. McGrath, "An Instruction Manual for Use of the Five-Hole Probe (DC-125) in the Swirl Generator", University of Ottawa. May,1984.

[29] H.L. Morton, "Effect of Swirl on Turbulent Flow in the Front End of Gas Turbine Main Burners," *AIAA* Paper No. 71-2, 1971.

[30] A.N. Rao, V. Ganesan, K.V. Gopalakrishnan and R. Natarajan, "Experimental and Theoretical Investigations of Vane- Generator Swirling Flows in a Circular Chamber", *Journal of the Institute of Energy*, Vol. 56, pp. 137–144,1983.

[31] D.L. Rhode, D.G. Lilley, and D.K. McLaughlin, "On the Prediction of Swirling Flowfields Found in Axisymmetric Combustor Geometries," *ASME Journal of Fluids Engineering*, Vol. 104, pp. 378–384, 1982.

[32] D.L. Rhode, D.G. Lilley, and D.K. McLaughlin, "Mean Flowfields in Axisymmetric Combustor Geometries with Swirl," *AIAA Journal*, Vol. 21, No.4 pp. 593–600, 1983.

[33] T. Sarpkaya, "Effect of the Adverse Pressure Gradient on Vortex Breakdown," *AIAA Journal*, Vol. 12, No. 5, pp. 602–607, 1974.

[34] G.L. Scharrer and D.G. Lilley, "Five-Hole Pitot Probe Measurements of Swirl, Confinement and Nozzle Effects on Confined Turbulent Flow," *AIAA* Paper No. 84-1605, 1984.

[35] H. Schlichting, **Boundary-Layer Theory,** McGraw-Hill Book Company, Seventh Edition, 1979.

[36] N. Syred and J.M. Beer, "Combustion in Swirling Flows: A Review," *Combustion and Flame*, Vol. 23, pp. 143–201, 1974.

[37] V. Tavasoli, "The Effect Of A Central Hub On The Onset Of Flow Reversal In A Swirling Sudden Expansion." *Thesis, Master of Applied Science. Mechanical Engineering, University of Ottawa.* December. 1988.

[38] H.L.Wu and N.Fricker, "The Characteristics of Swirl-Stabilized Natural Gas Flames. Part 2: The behavior of Swirling Jet Flames in a Narrow Cylindrical Furnace" *Journal of the Institute of Fuel.* Vol. 49, pp. 144–151, September, 1976.

Appendix A: Data Reduction Program

```
C     ****************************************************************
C     *   THE PROGRAMME OF THE STRUCTURE OF CENTRAL RECIRCULATION    *
C     *             ZONE IN ENCLOSED SWIRLING FLOW                   *
C     *                                                              *
C     *                                                              *
C     ****************************************************************


C     ****************************************************************
C     ALL THE VALUES START TO READ AT AXIS.

C     ****************************************************************
      PARAMETER (NN=35)
      DIMENSION P(NN),R(NN),PR(NN),U(NN),V(NN),W(NN),VT(NN),R2(NN)
      DIMENSION PSTPW(NN),PSTHPW(NN),UBACK(NN),VTUREF(NN),UUREF(NN)
      DIMENSION VUREF(NN),WUREF(NN),MFUNC(NN),GTFUNC(NN),GXFUNC(NN)
      DIMENSION UNI(NN),AP4P5(NN),AP1P2(NN),AP1PW(NN),APTCH(NN)
      DIMENSION PSTPWD(NN),OP(NN)

      REAL MANO,MT1,MIG,MA1,MTOT1,MREC,LT,LTI,LA,LAI,MFUNC
      COMMON LTH,SL,FLAG,N,R1,T,LT,LTI,LA,LAI
      COMMON PBAR,PBAR1,AP1PB,TKELV,AXIS,MANO,THROAT
      COMMON UNI,AP4P5,AP1P2,AP1PW,APTCH,NB,OP
      COMMON R,U,V,W,VT,PSTPW,PSTHPW,R2
      COMMON VUREF,WUREF,UUREF,VTUREF,MFUNC,GTFUNC,GXFUNC
      COMMON MIG,MT1,MA1,MTOT1,MREC,RATIO,S,S1,GT,GX,ERROR
      COMMON GTD,GXD,RE,ZETA1,UREF
      COMMON PREF,PFORCE,PDEM,THRUST,THRUSD,PSTPWD
C     ****************************************************************

      CALL INPUT
      CALL CV(AP1PB,TKELV,PBAR1,AXIS,N,P,R,R1,PR,U,W,V,VT,PSTPW,
     -        UNI,AP4P5,AP1P2,AP1PW,APTCH,NB,OP)
```

```
      CALL IMF(P,R,PR,U,W,V,NB,R1,MIG)
      CALL CMF(MIG,TKELV,PBAR,MANO,LT,LTI,LA,LAI,MT1,MA1,MTOT1,ERROR)
      CALL BM(P,R,U,NB,MIG,MREC,RATIO)
      CALL PP(P,R,W,NB,R2,PSTHPW)
      CALL PRE(R,U,NB,THROAT,MIG,PSTPW,UREF,RE,PREF,PFORCE,PDEM)
      CALL RVC(VT,U,W,V,NB,UREF,PREF,PSTPW,UUREF,WUREF,VUREF,
     -         VTUREF,PSTPWD)
      CALL SN1(MT1,MA1,THROAT,SL,S,ZETA1)
      CALL SN2(P,R,PR,U,W,NB,R1,UREF,MIG,THROAT,PFORCE,S1,GTD,GXD,GT,
     -         GX,THRUST,THRUSD)

      CALL MSFUN(P,R,U,MIG,NB,MFUNC)
      CALL CSF(PR,R,U,W,NB,R1,GT,GX,GTFUNC,GXFUNC)
      CALL FIGURE(R,UUREF,WUREF,NB,THROAT)
      CALL OUTPUT
      STOP
      END


C     ******************************************************
C     *            SUBROUTINE  INPUT                       *
C     ******************************************************
C     *             VARIABLE DECLARATION                   *
C     ******************************************************
C     * R1:      RADIUS OF TEST SECTION                    *
C     * LTH:     LENGTH OF TEST SECTION                    *
C     * FLAG:    FOR OUTPUT FORMAT CONTROL                 *
C     * AXIS:    TEST SECTION RADIUS AT AXIAL READ(MM);    *
C     * MANO:    INCLINED MANOMETER ANGLE;                 *
C     * PBAR:    BAROMETRIC PRESSURE(MMHG);                *
C     * THROAT:  RADIUS AT THROAT;                         *
C     * TKELV:   ROOM TEMPERATURE (K);                     *
C     ******************************************************
```

```
      SUBROUTINE INPUT
      REAL MANO,LT,LTI,LA,LAI

      COMMON LTH,SL,FLAG,N,R1,T,LT,LTI,LA,LAI
      COMMON PBAR,PBAR1,AP1PB,TKELV,AXIS,MANO,THROAT
C     ******************************************************


      READ(1,15)T,PBAR,R1,FLAG,LTH,N
      READ(1,25)LT,LTI,LA,LAI,SL
      READ(1,1) AP1PB,AXIS

      TKELV=T+273.15
      PBAR1=PBAR*133.32
      MANO=8.73
      THROAT=0.0508

 1    FORMAT(2X,2F10.4)
 15   FORMAT(2X,4F10.4,2X,I3,2X,I3)
 25   FORMAT(2X,5F10.4)

      RETURN
      END




C     ******************************************************
C     * SUBROUTINE   COMPUTES THE VELOCITIES AND MASS FLOW  *
C     ******************************************************
C     *            VARIABLE DECLARATION                     *
C     ******************************************************
```

```
C     * R:        MEASUREMENT OF TEST SECTION RADIUS ARRAY;  *
C     * P:        AIR DENSITY ARRAY;                         *
C     * U:        AXIAL VELOCITY ARRAY(M/S);                 *
C     * W:        TANGENTICAL VELOCITY ARRAY(M/S);           *
C     * V:        RADIAL VELOCITY ARRAY(M/S);                *
C     * X:        YAW ANGLE (RADIUS);                        *
C     * VT:       TOTAL VELOCITY ARRAY;                      *
C     * PR:       DENSITY TIMES RADIUS ARRAY;                *
C     * UNI:      MEASUREMENT VALUES OF THE RADIUS ARRAY(MM);*
C     * MIG:      INTERGRAL MASS FLOW;                       *
C     * PITCH:    ANGLE IS DISCRIBED BY RADIUS ARRAY;        *
C     * APITCH:   ANGLE IS DISCRIBED BY DEGREE ARRAY;        *
C     * P1P2:     DIFFREENCE PRESSURE (P1-P2,PA) ARRAY;      *
C     * P1PW:     DIFFERENCE PRESSURE (P1-PW, PA) ARRAY;     *
C     * P4P5:     DIFFERENCE PRESSURE (P4-P5, PA) ARRAY;     *
C     * PSTPW:    DIFFERENCE PRESSURE (PST-PW, PA) ARRAY;    *
C     * AP1P2:    DIFFERENCE PRESSURE (P1-P2, TORR) ARRAY;   *
C     * AP1PW:    DIFFERENCE PRESSURE (P1-PW, TORR) ARRAY;   *
C     * AP4P5:    DIFFERENCE PRESSURE (P4-P5, TORR) ARRAY;   *
C     * AP1PBAR: DIFFERENCE PRESSURE (P1-PBAR,PA);           *
C     ******************************************************


C      ************************************************************
C      *          SUBROUTINE  COMPUTE VELOCITIES                  *
C      ************************************************************
      SUBROUTINE CV(AP1PB,TKELV,PBAR1,AXIS,N,P,R,R1,PR,U,W,V,VT,PSTPW,
     -              UNI,AP4P5,AP1P2,AP1PW,APTCH,NE,OP)
      PARAMETER (NN=35)
      DIMENSION PITCH(NN),P1P2(NN),P1PW(NN),P4P5(NN),PSTPW(NN)
      DIMENSION UNI(NN),APTCH(NN),AP1P2(NN),AP1PW(NN),AP4P5(NN)
      DIMENSION P(NN),PR(NN),R(NN),U(NN),W(NN),V(NN),VT(NN),OP(NN)
C      ************************************************************
```

```
      DO 100 K=1,N
      READ(1,11) UNI(K),AP4P5(K),AP1P2(K),AP1PW(K),APTCH(K)
100   CONTINUE

      DO 110 K=1,N
          R(K)=-(UNI(K)-AXIS)/1000.
          PITCH(K)=APTCH(K)*0.01745
          P1P2(K)=AP1P2(K)*133.32
          P4P5(K)=AP4P5(K)*133.32
          P1PW(K)=AP1PW(K)*133.32
110   CONTINUE

      P1PBAR=AP1PB*133.32
      PW=P1PBAR-P1PW(4)
      II=0

      DO 111 J=1,N
         IF (ABS(P1P2(J)) .GE. 0.1)  THEN
            B=P4P5(J)/P1P2(J)
            IF (B .LE. 0.1779)  THEN
              X=(B+0.166)/0.0326
            ELSE
              X=(B+0.3)/0.0453
            END IF
         ELSE
           X=0.
         END IF

         IF (ABS(X).GT.40) THEN
            COEFV=0
            COFTP=0
            II=II+1
            OP(II)=R(J)
            GOTO 111
```

```
      ELSE
        COEFV1= 0.9572+(0.2406E-02*X)-(0.169E-03*X**2)
     -          -(0.4108E-06*X**3)+(0.3069E-06*X**4)

        COEFV2=((0.8975*X**5)-(0.1722*X**6)-
     -          (0.1266E-02*X**7)+(0.3939E-04*X**8))*(1E-09)

        COEFV3=(1E-15)*(0.4499*X**9)
        COEFV=COEFV1+COEFV2+COEFV3

        IF((X .GE.0) .AND. (X .LE. 10)) THEN
         COFTP=0.
        ELSE
         COFTP1=-0.4161E-02-(0.2027E-03*X)-(0.1657E-03*X**2)

         COFTP2=(-0.4862E-05*X**3)-(0.6963E-06*X**4)
     -          +(0.1214E-07*X**5)

         COFTP3=((0.5103*X**6)-(0.996E-02*X**7)-
     -          (0.1225E-03*X**8)+(0.2878E-05*X**9))*(1E-09)

         COFTP=COFTP1+COFTP2+COFTP3
        END IF

      X=X*0.01745
      END IF

      K=J-II
      R(K)=R(J)
      PITCH(K)=PITCH(J)
      P1P2(K)=P1P2(J)
      P4P5(K)=P4P5(J)
      P1PW(K)=P1PW(J)

    PSTPW(K)=P1PW(K)-P1P2(K)*COEFV*(1+COFTP)
```

```
      P(K)=0.46446*(PSTPW(K)+PW+PBAR1)/(TKELV*133.32)
      VT(K)=SQRT(2*COEFV*P1P2(K)/P(K))
      U(K)=VT(K)*COS(X)*COS(PITCH(K))
      W(K)=VT(K)*COS(X)*SIN(PITCH(K))
      V(K)=VT(K)*SIN(X)*(-1.)
      PR(K)=P(K)*R(K)
111   CONTINUE

      VT(K+1)=0.0
      U(K+1)=0.0
      V(K+1)=0.0
      W(K+1)=0.0
      PSTPW(K+1)=0.0
      P(K+1)=0.46446*(PW+PBAR1)/(TKELV*133.32)
      R(K+1)=R1
      PR(K+1)=P(K)*R1
      NB=K+1

      DO 112 I= K+2,N
         R(I)=0.
         PITCH(I)=0.
         P1P2(I)=0.
         P4P5(I)=0.
112      P1PW(I)=0.

      IF (R(1) .NE. 0.0) THEN
      DO 113 I=NB+1,2, -1
        R(I)=R(I-1)
        U(I)=U(I-1)
        V(I)=V(I-1)
        W(I)=W(I-1)
        PSTPW(I)=PSTPW(I-1)
        P(I)=P(I-1)
        PR(I)=PR(I-1)
        VT(I)=VT(I-1)
```

```
 113    CONTINUE

        R(1)=0.0
        U(1)=U(2)
        V(1)=0.
        W(1)=0.
        PSTPW(1)=PSTPW(2)
        P(1)=0.46446*(PSTPW(1) +PW+PBAR1)/(TKELV*133.32)
        PR(1)=0.0
        VT(1)=ABS(U(1))
        NB=NB+1
      END IF

 11   FORMAT(2X,5F10.4)
      RETURN
      END


C     ********************************************************
C     *      SUBROUTINE   COMPUTE INTEGRAL MASS FLOW         *
C     *      DUMMY: ARRAY IS EQUAL TO ONE ALL THE TIME;      *
C     ********************************************************

      SUBROUTINE IMF(P,R,PR,U,W,V,NB,R1,MIG)
      PARAMETER (NN=35)
      DIMENSION PR(NN),DUMMY(NN),P(NN),U(NN),V(NN),W(NN),R(NN)
      REAL MIG
C     ************************************************************


      DO 200 I=1,NB
 200     DUMMY(I)=1.
      CALL TRAP(PR,U,DUMMY,DUMMY,R,NB,TT)
      MIG=6.2832*TT
      RETURN
```

```
      END


C     ********************************************************
C     *   SUBROUTINE   COMPUTE THEORETICAL PRESSURE PSTHPW   *
C     ********************************************************

      SUBROUTINE  PP(P,R,W,NB,R2,PSTHPW)
      PARAMETER (NN=35)
      DIMENSION RI2(NN),W2(NN),P2(NN),R2(NN),P(NN),W(NN),R(NN)
      DIMENSION PSTHPW(NN)
C     ************************************************************


      DO 300 K=2,NB
          P2(NB-K+1)=P(K)
          W2(NB-K+1)=W(K)
          RI2(NB-K+1)=1./R(K)
          R2(NB-K+1)=R(K)
300   CONTINUE
      IF (R(1).NE. 0.0) THEN
        P2(NB)=P(1)
        W2(NB)=W(1)
        RI2(NB)=1./R(1)
        R2(NB)=R(1)
        N1=NB
        DO 330 II=2,N1
         CALL TRAP(P2,W2,W2,RI2,R2,II,TT)
         PSTHPW(II)=TT
330     CONTINUE
      ELSE
        N1=NB-1
        DO 333 II=2,N1
         CALL TRAP(P2,W2,W2,RI2,R2,II,TT)
```

```
          PSTHPW(II)=TT
 333      CONTINUE
          PSTHPW(NB)=PSTHPW(N1)
        END IF
          PSTHPW(1)=0.0

        RETURN
        END



C       ***************************************************
C       * SUBROUTINE  COMPUTE SWIRL NUMBER 1              *
C       * B:  WIDTH OF INLET GATES;                       *
C       * S:  THEORETICAL SWIRL NUMBER;                   *
C       * N1: INLET GATES;                                *
C       ***************************************************



        SUBROUTINE SN1(MT1,MA1,THROAT,SL,S,ZETA1)
        PARAMETER (NN=35)
        REAL MA1,MT1
C       *****************************************

             N1=4
             B=0.0256
             E=THROAT-B/2.
C            P=1.29
C            GT=(MT1**2.)*E/P*N1*B*SL
C            I=(MT1+MA1)**2./P*3.1416*(THROAT**2.)
             ZETA1=MT1/(MT1+MA1)
             S=((ZETA1**2.)*3.1416*E*THROAT)/(N1*B*SL)
        RETURN
```

```
      END


C     ***************************************************
C     * SUBROUTINE  COMPUTE SWIRL NUMBER 2              *
C     * S1:    MEASUREMENT OF SWIRL NUMBER;             *
C     * GX:    THE AXIAL FLUX OF AXIAL MOMENTUM;        *
C     * GT:    THE AXIAL FLUX OF TANGENTIAL MOMENTUM;   *
C     * GXD:   NON-DIMENSIONAL AXIAL MOMENTUM;          *
C     * GTD:   NON-DIMENSIONAL TANGENTIAL MOMENTUM;     *
C     ***************************************************

      SUBROUTINE SN2(P,R,PR,U,W,NB,R1,UREF,MIG,THROAT,PFORCE,
     -               S1,GTD,GXD,GT,GX,THRUST,THRUSD)

      PARAMETER (NN=35)
      DIMENSION  P(NN),PR(NN),U(NN),W(NN),R(NN)
      REAL MIG
C     ***********************************************************


      CALL TRAP(P,R,U,U,R,NB,TT)
      GX=6.2832*TT
      CALL TRAP(PR,U,W,R,R,NB,TT)
      GT=6.2832*TT
      S1=ABS(GT/(THROAT*GX))
      GTD=ABS(GT/(THROAT*MIG*UREF))
      GXD=ABS(GX/(MIG*UREF))
      THRUST=PFORCE+GX
      THRUSD=ABS(THRUST/(MIG*UREF))
      RETURN
      END
```

```
C      ******************************************************
C      * SUBROUTINE  COMPUTE PRESSURES                      *
C      * Q:     VOLUMETRIC FLOW RATE;                       *
C      * UREF:  REFERENCE AXIAL VELOCITY;                   *
C      * PREF:  REFERENCE PRESSURE;                         *
C      ******************************************************

       SUBROUTINE PRE(R,U,NB,THROAT,MIG,PSTPW,UREF,RE,PREF,PFORCE,PDEM)
       PARAMETER (NN=35)
       DIMENSION U(NN),R(NN),PSTPW(NN),DUMMY(NN)
       REAL MIG
C      ******************************************************

       DO 500 I=1,NB
 500     DUMMY(I)=1.

      CALL TRAP(U,R,DUMMY,DUMMY,R,NB,TT)
      Q=6.2832*TT
      A=(THROAT**2)
      UREF=Q/(3.1416*A)
      PREF=(MIG*Q)/(2*(3.1416**2)*(A**2))
      CALL TRAP(PSTPW,R,DUMMY,DUMMY,R,NB,TT)
      PFORCE=ABS(6.2832*TT)
      PDEM=ABS(PFORCE/(MIG*UREF))
      RE=(2.*UREF*THROAT)/0.0000150
      RETURN
      END
```

```
C      ***************************************************
C      * SUBROUTINE COMPUTE REFERENCE VELOCITIES          *
C      * PFORCE:PRESSURE FORCE;                           *
C      ***************************************************

       SUBROUTINE RVC(VT,U,W,V,NB,UREF,PREF,PSTPW,UUREF,WUREF,VUREF,
      -               VTUREF,PSTPWD)
       PARAMETER (NN=35)
       DIMENSION U(NN),V(NN),W(NN),VT(NN),PSTPWD(NN),PSTPW(NN)
       DIMENSION UUREF(NN),WUREF(NN),VUREF(NN),VTUREF(NN)
C      ***************************************************************



       DO 550 J=1,NB
         UUREF(J)=U(J)/UREF
         WUREF(J)=W(J)/UREF
         VUREF(J)=V(J)/UREF
         VTUREF(J)=VT(J)/UREF
         PSTPWD(J)=PSTPW(J)/PREF
 550   CONTINUE
       RETURN
       END




C      ***************************************************
C      *  SUBROUTINE  COMPUTE BACKFLOW MASS FLOW RATE     *
C      *  MREC:  BACKFLOW MASS FLOW RATE;                 *
C      ***************************************************

       SUBROUTINE BM(P,R,U,NB,MIG,MREC,RATIO)
```

```
      PARAMETER (NN=35)
      DIMENSION P(NN),UBACK(NN),DUMMY(NN),R(NN),U(NN)
      DIMENSION PP(NN),RR(NN)
      REAL MREC,MIG
C     ******************************************************

      II=1
      DO 700 K=1,NB
         IF (U(K).LT.0.0)  THEN
            UBACK(II)=0.5*(ABS(U(K))-U(K))
            IF((U(K)*U(K+1)).LT.0.0) THEN
              R0=R(K) + (R(K+1)-R(K))*(0.-U(K))/(U(K+1)-U(K))
              P0=P(K) + (P(K+1)-P(K))*(R0-R(K))/(R(K+1)-R(K))
              N1=II
            ELSE
              II=II+1
            END IF
         END IF
 700  CONTINUE


         DO 770 I=1,N1+1
 770        DUMMY(I)=1.
         DO 771 I=1,N1
            RR(I)=R(I)
 771        PP(I)=P(I)
         UBACK(N1+1)=0.
         RR(N1+1)=R0
         PP(N1+1)=P0
      CALL TRAP(PP,RR,UBACK,DUMMY,RR,N1+1,TT)
      MREC=6.2832*TT
      RATIO=MREC/MIG
      RETURN
      END
```

```
C     ************************************************
C     * SUBROUTINE  COMPUTE MASS-FLOW STREAM FUNCTION *
C     * MFUNC:  STREAM FUNCTION;                      *
C     ************************************************


      SUBROUTINE MSFUN(P,R,U,MIG,NB,MFUNC)
      PARAMETER (NN=35)
      DIMENSION P(NN),R(NN),U(NN),MFUNC(NN)
      REAL MIG,MFUNC
C     ************************************************


      DO 810 I=1,NB
  810    MFUNC(I)=0.0

      DO 820 K=2,NB
         TRAP3=(P(K)*U(K)*R(K)+P(K-1)*U(K-1)*R(K-1))*(R(K)-R(K-1))/2.
         MFUNC(K)=MFUNC(K-1)+6.2832*TRAP3/MIG
  820 CONTINUE
       RETURN
       END


C     ************************************************************
C     *  SUBROUTINE  COMPUTES THE STREAM FUNTION(MOMENTUM FLUX) *
C     *  GXFUNC: NON-DIMENSIONAL AXIAL MOMENTUM;                *
C     ************************************************************

      SUBROUTINE CSF(PR,R,U,W,NB,R1,GT,GX,GTFUNC,GXFUNC)
```

```
      PARAMETER (NN=35)
      DIMENSION  PR(NN),P(NN),R(NN),U(NN),W(NN),GTFUNC(NN),GXFUNC(NN)
C     ****************************************************************



      DO 910 J=1,NB
        GXFUNC(J)=0.0
        GTFUNC(J)=0.0
 910  CONTINUE

      DO 920  I=2,NB
         TRAP1=(PR(I)*U(I)*W(I)*R(I)+PR(I-1)*U(I-1)*W(I-1)*
     -             R(I-1))*(R(I)-R(I-1))/2.

         GTFUNC(I)=GTFUNC(I-1)+6.2832*TRAP1/GT

         TRAP2=(PR(I)*U(I)*U(I)+PR(I-1)*U(I-1)*U(I-1))*
     -             (R(I)-R(I-1))/2.

            GXFUNC(I)=GXFUNC(I-1)+6.2832*TRAP2/GX
  920  CONTINUE
       RETURN
       END



C      ****************************************************************
C      * SUBROUTINE  COMP. MASS FLOWS BASED ON THE INLET CONDITION
C      *
C      * LA:  INCLINED WATER INTINAL DISPLACEMENT IN CM ALONG THE
C      *      MANOMETER CONNECTED TO THE AXIAL PRESSURE TAP;
C      *
C      * LT:  INCLINED WATER INTINAL DISPLACEMENT IN CM ALONG THE
C      *      MANOMETER CONNECTED TO THE TANGENTIAL PRESSURE TAP;
```

```
C      *
C      * PA:  AXIAL GATE PRESSURE;
C      * PT:  TANGENTIAL GATE PRESSURE;
C      *
C      * LAI: INCLINED WATER FINAL DISPLACEMENT IN CM ALONG THE
C      *      MANOMETER CONNECTED TO THE AXIAL PRESSURE TAP;
C      *
C      * LTI: INCLINED WATER FINAL DISPLACEMENT IN CM ALONG THE
C      *      MANOMETER CONNECTED TO THE TANGENTIAL PRESSURE TAP;
C      *
C      * ZETA: THE RATIO OF THE TANGENTIAL MASS FLOWRATE TO THE TOTAL
C      *       MASS FLOWRATE;
C      ************************************************************


       SUBROUTINE CMF(MIG,TKELV,PBAR,MANO,LT,LTI,LA,LAI,
      -               MT1,MA1,MTOT1,ERROR)
       PARAMETER (NN=35)
       REAL LT, LA, LTI, LAI, MANO,MTOT1,MT1,MA1,MIG
C      ************************************************************


       PT=(98.1*SIN(MANO*0.017453)+0.4807)*(LTI-LT)
       PA=(98.1*SIN(MANO*0.017453)+0.4807)*(LAI-LA)
       MT1=0.007836*SQRT((PBAR-PT/133.32)*PT/TKELV)
       MA1=0.0019056*SQRT((PBAR-PA/133.32)*PA/TKELV)
       MTOT1=MT1+MA1
       ZETA=MT1/MTOT1
       ERROR=ABS((MIG-MTOT1)/MTOT1)*100
       RETURN
       END


C      ******************************************
C      *  SUBROUTINE  TRAPEZOIDAL RULE          *
```

```
C      ********************************************
       SUBROUTINE   TRAP(AA, BB, CC, DD, RTT, N, TT)
       PARAMETER (NN=35)
       DIMENSION AA(NN), BB(NN), CC(NN), DD(NN), RTT(NN)
C      ********************************************************

       TT=0.
       DO 1100 J=2,N
       TT1=AA(J)*BB(J)*CC(J)*DD(J)+AA(J-1)*BB(J-1)*CC(J-1)*DD(J-1)
       TT=TT+TT1*(RTT(J)-RTT(J-1))/2.
 1100  CONTINUE
       RETURN
       END

C      ************************************************************
C      SUBROUTINE  FIGURE IS FOR PLOTTING THE GRAPH OF THE
C      VELOCITY PROFILES
C      ************************************************************

       SUBROUTINE FIGURE(R,UUREF,WUREF,NB,THROAT)
       PARAMETER (NN=35)
       DIMENSION UUREF(NN),WUREF(NN),R(NN),RR(NN)

       DO 2100 I=1,NB
 2100     WUREF(I)=ABS(WUREF(I))
       DO 2110 J=1,NB
 2110     RR(J)=R(J)/THROAT

       CALL ANYDEV
       CALL PAGE(11.,8.5)
       CALL NOBRDR
       CALL AREA2D(9.5,6.5)
       CALL FRAME
```

```
      CALL DUPLX
      CALL XREVTK
      CALL YREVTK
      CALL YAXANG(0)
      CALL HEADIN('1.625 PT. 100-5 ',16,1.2,1)
      CALL XNAME ('R/R1$',100)
      CALL YNAME ('VELOCITY$',100)
      CALL THKFRM( .01)
      CALL GRAF(0.0,0.25,3.,-0.5,0.25,2.0)

      CALL MARKER (1)
      CALL THKCRV(.01)
      CALL CURVE(RR,UUREF,NB,-1)
      CALL SETCLR('GREEN')

      CALL MARKER (2)
      CALL THKCRV(.01)
      CALL CURVE(RR,WUREF,NB,-1)
      CALL SETCLR('RED')

      CALL LINES('U/UREF$',IPAK,1)
      CALL SETCLR('RED')
      CALL LINES('W/UREF$',IPAK,2)
      CALL SETCLR('RED')
C     CALL LEGEND(IPAK,3,0.5,5.8)
      CALL ENDPL(0)
      CALL DONEPL

      RETURN
      END



C     ****************************************
C     *   SUBROUTINE  PRINT ALL OF RESULTS   *
```

```
C     ****************************************

      SUBROUTINE OUTPUT
      PARAMETER (NN=35)
      DIMENSION P(NN),R(NN),PR(NN),U(NN),V(NN),W(NN),VT(NN),R2(NN)
      DIMENSION PSTPW(NN),PSTHPW(NN),UBACK(NN),VTUREF(NN),UUREF(NN)
      DIMENSION VUREF(NN),WUREF(NN),MFUNC(NN),GTFUNC(NN),GXFUNC(NN)
      DIMENSION UNI(NN),AP4P5(NN),AP1P2(NN),AP1PW(NN),APTCH(NN)
      DIMENSION PSTPWD(NN),OP(NN)
      REAL MANO,MT1,MIG,MA1,MTOT1,MREC,LT,LTI,LA,LAI,MFUNC

      COMMON LTH,SL,FLAG,N,R1,T,LT,LTI,LA,LAI
      COMMON PBAR,PBAR1,AP1PB,TKELV,AXIS,MANO,THROAT
      COMMON UNI,AP4P5,AP1P2,AP1PW,APTCH,NB,OP
      COMMON R,U,V,W,VT,PSTPW,PSTHPW,R2
      COMMON VUREF,WUREF,UUREF,VTUREF,MFUNC,GTFUNC,GXFUNC
      COMMON MIG,MT1,MA1,MTOT1,MREC,RATIO,S,S1,GT,GX,ERROR
      COMMON GTD,GXD,RE,ZETA1,UREF
      COMMON PREF,PFORCE,PDEM,THRUST,THRUSD,PSTPWD
C     ************************************************************

      WRITE(2,*)
      IF (FLAG.GT.0) THEN
      WRITE(2,2) R1,SL,LTH
      ELSE
      WRITE(2,4) R1,SL,LTH
      END IF
      WRITE(2,52)
      WRITE(2,*)
      WRITE(2,7)
      WRITE(2,*)
      WRITE(2,8)PBAR,T,AP1PB,N
      WRITE(2,*)
      WRITE(2,12)LT,LTI,LA,LAI
      WRITE(2,*)
```

```
      WRITE(2,16)
      DO 105 K=1,N
105      WRITE(2,18) UNI(K),AP4P5(K),AP1P2(K),AP1PW(K),APTCH(K)
      WRITE(2,*)
      WRITE(2,52)
      WRITE(2,20)
      WRITE(2,52)
      WRITE(2,*)
      WRITE(2,*)
      WRITE(2,22)
      DO 115 J=1,NB
115      WRITE(2,24) R(J),VT(J),U(J),W(J),V(J),PSTPW(J),PSTHPW(NB-J+1)
      WRITE(2,*)
      WRITE(2,26)
      DO 125 I=1,NB
125    WRITE(2,28) R(I),UREF,VTUREF(I),UUREF(I),WUREF(I),VUREF(I),
     -              MFUNC(I),GXFUNC(I),GTFUNC(I)
      WRITE(2,*)
      WRITE(2,*)
      WRITE(2,52)
      WRITE(2,30)
      WRITE(2,52)
      WRITE(2,*)
      WRITE(2,32) MIG, MTOT1,ERROR
      WRITE(2,*)
      WRITE(2,*)
      WRITE(2,34) MA1, MT1,ZETA1
      WRITE(2,*)
      WRITE(2,*)
      WRITE(2,36) MREC,RATIO,RE
      WRITE(2,*)
      WRITE(2,*)
      WRITE(2,38) S1,GTD,GXD
      WRITE(2,*)
      WRITE(2,*)
```

```
      WRITE(2,40) PREF,PFORCE,PDEM,THRUST,THRUSD
      WRITE(2,*)
      WRITE(2,*)
      WRITE(2,52)
      WRITE(2,44)
      DO 135 I=1,N-NB+2
  135 WRITE(2,46) OP(I)

C     ****************************************************************
    2 FORMAT(9X,17HEXPERIMENTAL DATA,2X,3HR2=,F8.4,2X,13HSWIRL SETTING,
     -       1X,2HL=,F6.3,3H(M),1X,3HAT.,2X,
     -       17HAXIAL LOCATION X=,I3,4H(CM))
    4 FORMAT(9X,17HEXPERIMENTAL DATA,2X,3HR2=,F8.4,2X,13HSWIRL SETTING,
     -       1X,2HL=,F6.3,3H(M),1X,3HPT.,2X,
     -       17HAXIAL LOCATION X=,I3,4H(CM))
    7 FORMAT(25X,10HINPUT DATA)
    8 FORMAT(9X,5HPBAR=,F6.2,6H(MMHG),5X,2HT=,F4.1,6X,6HAP1PB=,F8:3,
     -       5X,2HN=,I3)
   12 FORMAT(9X,3HLT=,F6.2,2HCM,4X,4HLTI=,F6.2,2HCM,4X,
     -       3HLA=,F6.2,2HCM,4X,4HLAI=,F6.2,2HCM)
   16 FORMAT(10X,3HUNI,1HM,4X,5HP4-P5,3X,5HP1-P2,6X,5HP1-PW,6X,5HPITCH)
   18 FORMAT(7X,3F8.2,3X,F8.2,3X,F8.2)
   20 FORMAT(28X,7HOUTPUTS)
   22 FORMAT(9X,1HR,3H(M),4X,2HVT,5H(M/S),2X,1HU,5H(M/S),2X,
     -        1HW,5H(M/S),2X,1HV,5H(M/S),4X,5HPSTPW,3H(N),
     -        5X,6HPSTHPW,3H(N))
   24 FORMAT(6X,F8.4,1X,4F8.3,4X,F9.3,5X,F8.3)
   26 FORMAT(11X,1HR,7X,4HUREF,4X,6HVTUREF,2X,5HUUREF,4X,5HWUREF,
     -       3X,5HVUREF,6X,5HMFUNC,5X,6HGXFUNC,4X,6HGTFUNC)
   28 FORMAT(6X,F8.4,3X,5F8.3,3X,F8.3,2X,F8.3,2X,F8.3)
   30 FORMAT(28X,19HINTEGRAL QUANTITIES)
   32 FORMAT(11X,19HINTEGRAL MASS FLOW=,F7.4,6H(KG/S),4X,
     -       24HTOTAL METERED MASS FLOW=, F7.4,6H(KG/S),2X,
     -       16HMASS FLOW ERROR=,F6.2,1H%)
   34 FORMAT(11X,24HAXIAL METERED MASS FLOW=,F7.4,6H(KG/S),2X,
```

```
     -        29HTANGENTIAL METERED MASS FLOW=,F7.4,6H(KG/S),
     -        2X,6HZETA1=,F6.2)
  36 FORMAT(11X,24HRECIRCULATING MASS FLOW=,F6.4,6H(KG/S),5X,
     -        18HFRACTION OF TOTAL=,F6.3,4X,3HRE=,F10.2)
  38 FORMAT(11X,10HSWIRL NO.=,F6.2,2X,4HGTD=,F6.3,2X,4HGXD=,F6.3)
  40 FORMAT(11X,5HPREF=,F8.2,4X,7HPFORCE=,F6.2,2X,5HPDEM=,F6.2,
     -        2X,7HTHRUST=,F5.2,2X,7HTHRUSD=,F5.2)
  44 FORMAT(6X,5HNOTE:)
  46 FORMAT(11X,5HAT R=,F6.4,1X,32HTHE MEASURED VALUE OUT OF RANGE.)

  52 FORMAT(9X,51H*****************************************************)
     RETURN
     END
```

Appendix B: Numerical Solution Program

```
C ================================================================
C =       THE CALCULATION OF THE MATHEMATICAL MODEL              =
c =                                                              =
C ================================================================


C ================================================================
C =                    INPUT DATA                                =
C =          R2R1=R2/R1;                                         =
C =          A1R2=A1/R1;                                         =
C =          A2R2=A2/R2;                                         =
C =          ALRB=AL/RB;                                         =
C ================================================================

      IMPLICIT DOUBLE PRECISION (A-H,O-Z)
      DOUBLE PRECISION LEBTA, MRM2

      R1=0.0508
      R2R1=2.813
      R2=R2R1*R1
      A1R1=0.894
      U1=27.28
      A2R2=0.318
      GTD=1.038
      LEBTA=-0.066
      ALRB=1.5

C ================================================
C |    A11=(A1/R1)**2;                           |
C |    A22=(A2/R2)**2;                           |
C |    R22=(R2/R1)**2;                           |
C |    GAMA11=GAMA1/U1R1;                        |
C |    AI1=I1/PI*RHO*U1*U1*R1*R1;                |
```

```
C |     P1=P1-PI*PO1*R1*R1*R2/U1*U1*PI*RHO*R1*R1;          |
C ==================================================

      A2=A2R2*R2
      A11=A1R1**2
      A22=A2R2**2
      R22=((R2/R1)**2)
C ===================================================================

      F1=1.-A11*(1.-LEBTA)/3.
      F2=1.+A11*(LEBTA*0.1-0.6)
      F3=(6.-(A22**(2.5)))/15.
      F4=(4.-(A22**(1.5)))/6.
      GAMA11=GTD*((F1**2)/F2)
      GAMA1=GAMA11*U1*R1
C     GAMA1=0.031
C     GAMA11=GAMA1/(U1*R1)

C ===================================================================

      C1=(R22/A11-3./4.-0.5*DLOG(R22/A11))*((GAMA11)**2)
      C2=1-A11*(0.5-LEBTA/3.-(LEBTA**2)/6.)
      C3=-0.5*R22*(LEBTA**2)-4./3.*(F1**2)/R22
C ===================================================================

      AI1=(1-A11*(0.5-LEBTA/3.-(LEBTA**2)/6.))
      P1=(GAMA11**2)*(R22/A11-3./4.-0.5*DLOG(R22/A11))

C ===================================================================

      WRITE(6,2) GTD,R2R1,LEBTA
      WRITE(6,*)
      WRITE(6,3) A1R1,A2R2,ALRB
      WRITE(6,*)
      WRITE(6,*)
```

```
      WRITE(6,4) GAMA11,AI1,P1
    2 FORMAT(5X,4HGTD=,F8.6,5X,6HR2/R1=,F8.4,2X,6HLEBTA=,F6.4)
    3 FORMAT(5X,5HA1R1=,F6.4,2X,5HA2R2=,F6.4,2X,
     -       6HAL/RB=,F6.4)
    4 FORMAT(5X,12HGAMMA1/U1R1=,F6.3,5X,3HI1=,F6.3,5X,3HP1=,F6.3)
      WRITE(6,*)
      WRITE(6,*)

C ========================================================
C |    U02U1=U02/U1;                                      |
C |    MRM2=MR/M2;                                        |
C |    U02U2=U02/U2;                                      |
C |    W2R2=W2*R2/U1*R1;                                  |
C |    RBR2=RB/R2;                                        |
C |    RCR2=RC/R2;                                        |
C |    U02U11=U02/U1;                                     |
C |    U02UR=U02/UREF;                                    |
C |    BK: LOSS COIFICIENT;                               |
C |    SK: SCHLICHTING COIFICIENT,ROUGHLY K=0.0256;       |
C |    AL: DISTANCE BETWEEN 2 TO S;                       |
C |    AI2=I2/PI*RHO*R1*R1*U1*U1;                         |
C |    P2=(P2-PI*P01*R1*R1*R22)/(PI*RHO*U1*U1*R1*R1);     |
C ========================================================

      WRITE(6,5)
      WRITE(6,*)
C=====================================================================

      SK=0.0
      DO 100 I=1,120
        SK=SK + 0.01
        U02=1.0
      DO 200 J=1,600
        U02=U02+ 0.01
C=====================================================================
```

```
      U02U1=U02/U1
      DU=2.*U1*F1/R22+2.*U02
      U02UR=U02/((0.5*DU-U02)*R22)
      IF (2.*U02/DU .LE.0.0) GOTO 200
      RB=R2*DSQRT(2.*U02/DU)
      RBR2=RB/R2
      RCR2=DSQRT*(0.5*(RBR2))
      F6=A22/4.-0.5*DLOG(A22)
      BK=32.*SK*ALRB

C =================================================================

      C4=-2.*U02*F1/(3.*U1)+R22*((U02/U1)**2)*(0.5*(1-BK)-1./3.)
      IF ((C1+C2+C3+C4)/F6 .LE. 0.0) GOTO 200
      W2R2=DSQRT((C1+C2+C3+C4)/F6)
      U02U11=(GAMA11*F2/W2R2-2*F1*F3)/(R22*(2.*F3-F4))
      W2R21=W2R2*U1*R1

C =================================================================
     IF (ABS(U02U11-U02U1).LT.5D-3)  THEN

C =================================================================

      U2=2.*U1*F1/R22+U02
      MRM2=(U02*U02)/(U2*U2-U02*U02)
      P2=0.5*R22*((LEBTA**2)-((U02/U1)**2)*(1-BK))+(W2R2**2)*F6
      AI2=(4.*(F1**2)/(3.*R22)+2.*U02*F1/(3.*U1)+R22*((U02/U1)**2)/3.)

C =================================================================

      WRITE(6,6)  SK,U02U1,U02U11,MRM2,RCR2,U02UR,U02,BK

   5  FORMAT(4X,2HSK,2X,6HU02/U1,2X,7HU02/U11,3X,5HMR/M2,
     -       6X,5HRC/R2,5X,6HU02/UR,5X,3HU02,5X,2HBK)
```

```
    6    FORMAT(1X,F5.2,2X,F5.3,3X,F5.3,5X,F5.3,5X,F6.3,5X,F6.3,
   _          3X,F6.3,3X,F6.2)


         END IF
  200    CONTINUE
  100    CONTINUE

C ================================================================================
         STOP
         END
```

Appendix C: Fitted Inlet Velocity Profile Program

```
================================================================
   THE PROGRAM OF FITTED INLET VELOCITY PROFILE PARAMETERS
================================================================

10 REM PROGRAM FITPROF1 FITS VELOCITY PROFILES OF THE FORM USED FOR
VORTEX BREA KDOWN MODEL VII TO MEASURE VELOCITY PROFILES
20 REM REVISED 26.2.87 TO INCLUDE COORECTION FOR WALL BOUNDARY LAYER
30 REM VERSION WITH SOLID BODY VORTEX POINT AS INPUT FOR CIRCULATION
40 LPRINT CHR$(27) "B" CHR$(2)
50 LPRINT CHR$(27) "M" CHR$(10)
60 LPRINT "          VELOCITY PROFILE FITS - MODEL VII"
70 LPRINT "     CORRECTION FOR WALL BOUNDARY LAYER APPLIED"
80 LPRINT
90 LPRINT " EXPT.  LAMBDA   A1    GAMMA1   a1    u1/u  w1/u@a1  u1/u
   w1/u@a1     w1/u@rB"
100 LPRINT             (a1/r1)^2   (mm)   (mm)    (for model)    (for
velocity profiles)"
110 LPRINT
120 REM ALL DIMENSIONS IN MM
130 R1=50.6
140 RB=48.34
150 R1RB=(R1/RB)^2
160 INPUT "EXPERIMENT NUMBER ";E$
170 INPUT "CENTRELINE VELOCITY - DIMLESS."LAMU1
180 INPUT "DIMENSIONLESS ANGULAR MOMENTUM FLUX ";OMEGA
190 INPUT "TANGENTIAL VELOCITY IN SOLID BODY REGION - DIM.LESS";W
200 INPUT "RADIUS AT WHICH THIS VELOCITY WAS MEASURED - mm ";R
210 LAMU1=LAMU1/R1RB
220 W=W/R1RB
230 K=W/R
240 SS=OMEGA/RB
250 A2C=-1.4-3.6/LAMU1
260 A1C=(6+2*SS)/LAMU1
```

```
270 A0C=-6*SS/LAMU1
280 REM SOLVE CUBIC
290 P=-(A2C^2)/3+A1C
300 Q=2*(A2C/3)^3-A2C*A1C/3+A0C
310 BIGQ=(P/3)^3+(Q/2)^2
320 IF BIGQ>0 GOTO 520
330 ARG=P/3
340 IF ARG>0 GOTO 910
350 COSA=-Q/2/SQR(-(ARG*ARG*ARG))
360 TANA=SQR(1-COSA*COSA)/COSA
370 ALPHA=ATN(TANA)
380 IF COSA<0 THEN ALPHA=ALPHA+3.141592654#
390 ARG1=2*SQR(-ARG)
400 Y1=ARG1*COS(ALPHA/3)
410 Y2=-ARG1*COS(ALPHA/3+1.047198)
420 Y3=-ARG1*COS(ALPHA/3-1.047198)
430 X1=Y1-A20/3
440 X2=Y2-A20/3
450 X3=Y3-A20/3
460 PRINT "ROOTS; "X1,X2,X3
470 INPUT "WHICH ONE (1,2 OR 3)";IR
480 IF IR=1 THEN A1=X1
490 IF IR=2 THEN A1=X2
500 IF IR=3 THEN A1=X3
510 GOTO 660
520 POW=1/3
530 AA=-Q/2-BQR(BIGQ)
540 IF AA<0 GOTO 570
550 AA=AA^POW
560 GOTO 580
570 AA=-(-AA)^POW
580 BB=-Q/2-SQR(BIGQ)
590 IF BB<0 GOTO 620
600 BB=BB^POW
610 GOTO 630
```

```
620 BB=-(-BB)^POW
630 A1=AA-BB
640 A1=A1-A20/3
650 PRINT "SOLUTION FOR BIG Q>=0: ";A1
660 ZERO=A1^3+A2C*A1^2+A1C*A1+A0C
670 PRINT "ZERO = ";ZERO
680 LAMBDA=(1-A1/3)/(1/LAMU1-A1/3)
690 U1=LAMU1/LAMBDA
700 A1R1=SQR(A1)
710 A1MM=A1R1*RB
720 GAM=K*A1*RB^2
730 WA1=GAM/A1MM
740 WR1=GAM/RB
750 U1P=U1*R1RB
760 WA1P=WA1*R1RB
770 WR1P=WR1*R1RB
780 LPRINT USING "  \  \";E$
790 LPRINT USING " ##.###  ";LAMBDA;
800 LPRINT USING " ###   ";A1;
810 LPRINT USING " ##.### ";GAM;
820 LPRINT USING " ##.##  ";A1MM;
830 LPRINT USING " ##.### ";U1;
840 LPRINT USING " ##.### ";WA1;
850 LPRINT USING "   ##.###";U1F;
860 LPRINT USING " ##.###";WA1P;
870 LPRINT USING " ##.###";WR1P;
880 GOTO 920
890 OMEGN=K*RB*A1*(1+A1*(LAMBDA/10-0.6))/(1-A1/3*(1-LAMBDA))
900 PRINT OMEGN
910 PRINT "NEGATIVE ARGUMENT OF CUBIC"
920 OMEGN=K*RB*A1*(1+A1*(LAMBDA/10-0.6))/(1-A1/3*(1-LAMBDA))
930 PRINT OMEGN
940 INPUT "ANOTHER PROFILE ";Y$
950 IF Y$="Y" GOTO 160
960 END
```